THERMO-MECHANICAL AND MICRO-STRUCTURAL CHARACTERIZATION OF SHAPE MEMORY POLYMER FOAMS

A Dissertation
Presented to
The Academic Faculty

By

Matthew Allen Di Prima

In Partial Fulfillment
Of the Requirements for the Degree
Doctor of Philosophy in Materials Science and Engineering

Georgia Institute of Technology

May, 2009

Thermo-mechanical and Micro-structural Characterization of Shape Memory Polymer

Approved by:

Dr. Kenneth Gall, Advisor
School of Materials Science and Engineering
Woodruff School of Mechanical Engineering
Georgia Institute of Technology

Dr. David McDowell, Co-Advisor
School of Materials Science and Engineering
Woodruff School of Mechanical Engineering
Georgia Institute of Technology

Dr. Meisha Shofner
School of Polymer, Textile & Fiber Engineering
School of Materials Science and Engineering
Georgia Institute of Technology

Dr. Rina Tannenbaum
School of Materials Science and Engineering
Georgia Institute of Technology

Dr. Robert Guldberg
Woodruff School of Mechanical Engineering
Georgia Institute of Technology

Dr. Terry Sanderson
School of Aerospace and Mechanical Engineering
University of Arizona
Raytheon Missile Systems

Date Approved: March 13, 2009

ACKNOWLEDGEMENTS

I would like to thank Dr. Ken Gall, Dr. Terry Sanderson, and Dr. David McDowell for there support and commitment to this project. Their guidance and input proved to be invaluable. Without the support of the Advanced Materials Lab; and my undergraduate assistants Martha Lesniewski, Erica Hockings, Anthony Formica, Jeremy Kinnaird, and Dusting Simons this project would have taken much longer. Raytheon Missile Systems' support through Dr. Sanderson and the Advanced Materials Development team started and kept the project going. Further support was provided by the Air Force Office of Scientific Research Phase I/II STTR, contract number FA9550-07-C-0115. Dr. Steven Arzbeger and Douglass Campbell at Composite Technology Development for the various epoxy foams and material support. Angela Lin at the Georgia Institute of Technology Orthopaedic Bioengineering Laboratory for her immeasurable assistance in performing the micro-CT scanning.

TABLE OF CONTENTS

ACKNOWLEDGEMENTS iii

LIST OF TABLES vii

LIST OF FIGURES viii

LIST OF SYMBOLS AND ABBREVIATIONS xii

SUMMARY xiv

CHAPTER 1: INTRODUCTION 1

1.1 Shape Memory Polymer Behavior and Systems 2
1.2 Recovery Mechanism of Thermally Activated Cross-Linked Polymers 4
1.3 Shape Memory Polymer Research 5
1.4 Shape Memory Polymer Foam 6
1.5 Introduction to Micro-CT Scanning 9
1.6 Modeling of Foam 11
1.7 Introduction to Epxoy Shape Memory Polymer Foam 13
1.8 Introduction to Thermomechanical Testing 14

CHAPTER 2: THERMO-MECHANICAL BEHAVIOR OF EPOXY SHAPE MEMORY POLYMER FOAMS 17

2.1 Introduction 17
2.2 Experimental Method 18
2.2.1 Materials and Specimen 18
2.2.2 Experimental Apparatus 19
2.2.3 Experiments 19
2.3 Results 23
2.4 Discussion 35
2.5 Conclusion 40

CHAPTER 3: DEFORMATION OF EPOXY SHAPE MEMORY FOAMS: EXPERIMENTS AND CONSTITUTIVE MODELING 42

3.1 Introduction 42
3.2 Background 43
3.3 Experimental 44
3.4 Results 48
3.5 Discussion 60
3.6 Conclusions 64
CHAPTER 4: DEFORMATION OF EPOXY SHAPE MEMORY FOAMS: MESOSCALE MODELING AND DEFORMATION 66
4.1 Introduction 66
4.2 Experiments 67
4.3 Simulation 69
4.4 Results 73
4.5 Discussion 85
4.6 Conclusions 88
CHAPTER 5: CYCLIC COMPRESSIVE BEHAVIOR OF EPOXY SHAPE MEMORY POLYMERS 89
5.1 Introduction 89
5.2 Background 90
5.3 Experimental 90
5.4 Results 93
5.5 Discussion 108
5.6 Conclusions 113
CHAPTER 6: CONCLUSIONS 115
6.1 Introduction 115
6.2 Fundamental Advances 116
6.3 Practical Applications 118
6.4 Future Directions 119
6.5 Conclusion 121
APPENDIX A: Determing T_g 122
APPENDIX B: Reinforced Foam 127

APPENDIX C: Mechanical Efficiency 132

APPENDIX D: Micro-CT Scans 135

REFERENCES 144

LIST OF TABLES

Table 3.1: Fitting Parameters 53

Table 3.2: Adjusted Fitting Parameters 57

Table 4.1: Hyperelastic Material Fit Parameters 72

Table 4.2: DMA results for sample and batch repeatability 75

Table 4.2: Lognormal Cumulative PDF Fit Parameters 85

Table 5.1: Cycles to Failure as a function of Hold Time. 100

LIST OF FIGURES

Figure 1.1 Shape Memory Cycle 5

Figure 1.2 Compressive response of SMP foam. 8

Figure1.3: Examples of CTD's Epoxy SMP foam. 14

Figure 2.1 :DMA results of TEMBO 3XE Foam and Resin. 24

Figure 2.2: Compression response as a function of temperature. 25

Figure 2.3: Analysis of block compression testing. 26

Figure 2.4: Tensile Response of TEMBO 3XE as a function of temperature. 27

Figure 2.5: Effect of cycling on the maximum stress at a set strain for TEMBO 3XE. ... 28

Figure 2.6: Temperature dependence of permanent strain during cyclic loading for TEMBO 3XE. 30

Figure 2.7: Recovery response at differing packaging temperatures for TEMBO 3XE... 32

Figure 2.8: 6μm resolution x-ray micro-CT image of TEMBO 3XE. 33

Figure 2.9: Microstructure response of TEMBO 3XE to deformation at 125°C. 34

Figure 3.1: Distribution of 2a) pore spacing and 2b) strut thickness as determined through micro-CT scanningof DP5.1. 49

Figure 3.2: Representative micro-CT images of the three different foam relative densities of DP5.1. 50

Figure 3.3: The storage modulus and tan delta of the base polymer and the three relative densities as a function of temperature as determined by DMA. 51

Figure 3.4: : Comparison of the experimental storage moduli of the three relative densities and the moduli predicted by Equation 3.1. 52

Figure 3.5: Comparison of tensile strain to failure of DP5.1 foam and resin. 52

Figure 3.6: Compressive response of the three different relative densities at three different temperatures. 54

Figure 3.7: Fitting of the compressive response using Equations 3.4 and 3.6. 55

Figure 3.8: Constrained cooling response during shape packaging of the three different densities..... 58

Figure 3.9: Shape recovery response for the three different relative densities..... 59

Figure 4.1: FE meshes generated via CT scanning for ABAQUS simulation..... 70

Figure 4.2: DMA results of DP5.1 sample and batch consistency. 74

Figure 4.3: Response of the DP5.1 base polymer in compression and tension at T_g + 17°C, or 102°C..... 77

Figure 4.4: Stress/strain response from ABAQUS simulations of the three relative densities..... 78

Figure 4.5: Representative local deformation behavior from macroscopic compression. 78

Figure 4.6: Schematic of the macroscopic compression resulting in local non-compressive strains. 80

Figure 4.7: Cumulative local tensile strain distributions from the ABAQUS simulations. 81

Figure 4.8: Cumulative local tensile strain distributions from the ABAQUS simulations. 83

Figure 5.1: Shape recovery properties of 14% RD as the packaging temperature is varied. 93

Figure 5.2: Schematic of the cyclic compression test..... 94

Figure 5.3: Cyclic behavior of 20% RD foam for 100 cycles at varied maximum strains. 96

Figure 5.4: Cyclic behavior of 30% RD foam for 100 cycles at varied maximum strains. 97

Figure 5.5: Cyclic behavior of 40% RD foam for 100 cycles at varied maximum strains. 98

Figure 5.6: Cyclic behavior of 20% RD foam for 100 cycles with varying hold times. 101

Figure 5.7: Cyclic behavior of 30% RD foam for 100 cycles with varying hold times. 102

Figure 5.8: Cyclic behavior of 40% RD foam for 100 cycles with varying hold times. 103

Figure 5.9: Representative micro-CT of DP5.1 foam..... 104

Figure 5.10: Quantitative structural response to cyclic deformation of 17% RD foam over 100 cycles..... 105

Figure 5.11: Examples of microfracturing of struts pre-macroscopic failure..... 108

Figure 5.12: Stress relaxation of base polymer at 76°C and 110°C. 110

Figure A.1: DSC of TEMBO 3XE foam. 122

Figure A.2: DSC of DP5.1 resin. 122

Figure A.3: DSC comparison of 1st and 2nd passes for unreinforced, nickel, and nanomagnetite reinforced DP5.1. 123

Figure A.4: DSC of 2nd pass of unreinforced, nickel, and nanomagnetite reinforced DP5.1. 123

Figure A.5: DSC of DP5.1 reinforced with 0.5, 1.0, 2.0, 5.0, and 10.0 wt% multi-walled carbon nanotubes (CNT). 124

Figure A.6: Effect of Nanomagnetite reinforcement in DP5.1 foams on T_g and modulus. 124

Figure A.7: Effect of time on the T_g of DP5.1 foam..... 125

Figure A.8: Effect of time on the T_g of DP5.1 resin. 125

Figure A.9: Effect of humidity on the T_g of DP5.1 foam. 126

Figure B.1: Comparison of 4wt% and 0wt% VGCF reinforced foam at 25°C..... 127

Figure B.2: Comparison of 4wt% and 0wt% VGCF reinforced foam at T_g - 10°C. 127

Figure B.3: Comparison of 4wt% and 0wt% VGCF reinforced foam at T_g. 128

Figure B.4: Comparison of 4wt% and 0wt% VGCF reinforced foam at T_g + 25°C. 128

Figure B.5: Comparison of tensile response at 25°C for VGCF reinforced DP5.1 foam. 129

Figure B.6: Comparison of tensile response at T_g + 25°C for VGCF reinforced DP5.1 foam. 129

Figure B.7: Comparison of 11% RD VGCF reinforced DP5.1 foam DP5.1 at 25°C..... 130

Figure B.8 Comparison of 11% RD VGCF reinforced DP5.1 foam DP5.1 at T_g - 10°C. 130

Figure B.9: Comparison of 11% RD VGCF reinforced DP5.1 foam DP5.1 at T_g. 131

Figure B.10: Comparison of 11% RD VGCF reinforced DP5.1 foam DP5.1 at T_g + 25°C. 131

Figure C.1: Schematic of Mechanical efficiency. 132

Figure C.2: Packaging response for DP5.1 20% RD foam at 1.1*T_g. 132

Figure C.3: Schematic of observing output of mechanical energy. 133

Figure C.4: Energy recovered response for DP5.1 20% RD foam. 133

Figure C.5: Mechanical energy efficiency as a function of packaging strain. 134

Figure D.1: As received TEMBO 3XE. 135

Figure D.2: 15% compressed TEMBO 3XE at 25°C 135

Figure D.3: 30% compressed TEMBO 3XE at 25°C 136

Figure D.4: 45% compressed TEMBO 3XE at 25°C 136

Figure D.5: 60% compressed TEMBO 3XE at 25°C 137

Figure D.6: 15% compressed TEMBO 3XE at 125°C 137

Figure D.7: 30% compressed TEMBO 3XE at 125°C 138

Figure D.8: 45% compressed TEMBO 3XE at 125°C 138

Figure D.9: 45% compressed TEMBO 3XE at 125°C 139

Figure D.10: DP5.1foam reinforced with 5wt% MagSilica 139

Figure D.11: DP5.1 reinforced with 1wt% nanomagnetite. 140

Figure D.12: DP5.1 reinforced with 2.5wt% nanomagnetite. 140

Figure D.13: DP5.1 reinforced with 5wt% nanomagnetite. 141

Figure D.14: DP5.1 reinforced with 10wt% nanomagnetite. 141

Figure D.15: DP5.1 foam, ~8% RD. 142

Figure D.16: DP5.1 foam reinforced 0.5wt% VGCF, ~9% RD 142

Figure D.17: DP5.1 foam reinforced 1w% VGCF, ~8% RD 143

Figure D.18: DP5.1 foam reinforced 4w% VGCF, ~24% RD 143

LIST OF SYMBOLS AND ABBREVIATIONS

SMP	Shape memory polymer
T_g	Glass transition temperature
CTD	Composite Technology Developement
VGCF	Vapor grown carbon fiber
CT	Computed tomography
DMA	Dynamic mechanical analysis
DSC	Differential Scanning Calorimetry
TA	Thermal Analysis
ASTM	American Society for Testing and Materials
MTS	Materials Testing Systems
$e_{Recover}$	Recovered strain
$e_{Permanment}$	Non-recovered strain
e_{Max}	Maximum strain
e_{Unload}	Elastically recovered strain
s_{Max}	Maximum stress
E^*	Modulus of foam
E_s	Modulus of base polymer
ρ^*	Density of foam
ρ_s	Density of base polymer
E_D	Densification strain
σ^*	Stress of foam

σ_{el}^{*}	Elastic stress limit of foam
ϵ_{el}^{*}	Elastic strain limit of foam
m	Fitting parameter
D	Fitting parameter
RD	Relative density
T_{Test}	Test temperature
ANOVA	Analysis of variables
I_1	First deviatoric strain invariant
I_2	Second deviatoric strain invariant
C_{ij}	Temperature dependent material parameter
D_i	Temperature dependent material parameter
J^{el}	Elastic volume ratio
ε_{app}	Applied strain
ε_x	Comparison strain
t_{hold}	Hold time
$e_{residual}$	Residual strain
CNT	Carbon nanotube

SUMMARY

The need for a set of design criteria, models, and limits for the use of shape memory polymer foams was proposed. The effect of temperature and strain on the mechanical behavior; compression, tensile, cyclic compression, constrained recovery, and free strain recovery of the material was used to determine the operational limits of the material. Next, the damage mechanism and viscoelastic effects in compressive cycling were determined through further mechanical testing and with the incorporation of three dimensional structure mapping via micro-CT scanning. The influence of microstructure was determined by testing the basic thermomechanical, viscoelactic, and shape recovery behavior of foams with relative densities of 20, 30, and 40 percent. A similar suite of tests were then performed with the base epoxy material to generate the material properties for computational modeling. This data was then combined with three dimensional microstructures generated from micro-CT scans to develop material models for shape memory foams. These models were then validated by comparing model results to the experimental results under similar conditions.

CHAPTER 1: INTRODUCTION

Shape memory polymer (SMP) foams exhibit a unique blend of low density, high compressibility, and shape memory behavior that gives them a wide range of potential applications. The majority of proposed applications are in the aerospace field (Sokolowski W M, 1999; Tey, et al., 2001; Tobushi, et al., 2004; Tobushi, et al., 2001) where the low density of the foam offsets relatively lower mechanical properties compared to solid shape memory polymers. The application motivating this project is highly compact, storable wing structures with morphing ability to be used in tube launched air vehicles. The constraint of tube stowage has reduced the efficiency of these air vehicles compared to non-tube launched vehicles, and SMP foams can be used to bridge the performance gap (Sanderson and Gall, 2007). Other applications include space deployable support structures, shelters for space habitation, and rover components; a more exhaustive list can be found in W.M. Sokolowski et al (Sokolowski W M, 1999). The increased surface area and compressibility of the foams also has promise in biomedical implants (Maitland, et al., 2007; Metcalfe, et al., 2003; Small, et al., 2007) as embolic sponges. Before the potential of shape memory polymer foams can be reached, work must be performed to characterize their thermo-mechanical response under complex loading histories representative of applications and to develop a link between foam structure and thermo-mechanical properties. Once this understanding is reached, models need to be made so industry can efficiently incorporate SMP foams into new and existing products.

Although prior efforts have considered shape memory polymer foams, they have not considered a comprehensive set of thermo-mechanical deformation paths. In addition, most prior work focuses on thermoplastic foams whose physical cross links can have finite life and shape memorization capacity. Furthermore, prior studies on shape memory polymer foams provide minimal characterization of initial foam structure and little or no assessment of foam structure during storage and recovery paths. The purpose of this project is to provide a more thorough understanding of the thermo-mechanical storage and recovery behavior in thermoset shape memory foams under relevant deformation conditions, enhanced understanding of cyclic damage mechanisms, and the effect of microstructure. Moreover, the combination of macroscopic thermo-mechanical tests and x-ray micro computed tomography are used to help understand the fundamental linkages between pore structure in different deformation regimes and associated recoverable strain limits. Micro-CT characterization allows direct tracking of the foam structure during storage and recovery tests.

1.1 Shape Memory Polymer Behavior and Systems

SMPs are materials that have the ability to recover their original shape after being deformed. The original shape is set when the material is formed/cast through solidification from a melt (thermoplastic) or chemical cross-linking (thermoset), a process that also sets the glass transition temperature (T_g) of the SMP. In thermal systems, the material can be deformed into a second shape above T_g. This deformed shape is retained when the temperature drops below T_g. When the material is subsequently heated above the T_g, the material returns to the original shape. In

thermoplastic SMPs, this occurs due to the dual phases that are present; the soft amorphous portion and a hard crystalline portion. The crystal phase retains the original shape, while the amorphous phase allows deformation that does not influence the stability of the crystalline region (Lendlein and Kelch, 2002; Ohki, et al., 2004). Chemically cross-linked thermoset shape memory polymer systems retain a temporary shape via molecular interactions between chains formed during thermomechancial shape storage, the permanent shape is fixed by the chemical cross link points formed during initial polymerization. Related thermal systems do not need external ambient heat to recover their initial shape; electric current or magnetic fields can lead to heating of the polymer and subsequent shape recovery (Yang, et al., 2005). The electric current-activated SMP requires that the polymer be conductive or that it have a conductive reinforcement and the magnetic activated SMP requires appropriate magnetic filler (Annette, 2006; Buckley, 2006; Vialle, et al., Submitted).

The aforementioned SMPs depend on heat to return to the original shape; other systems use light to instigate shape retention (Lendlein, et al., 2005). The light activated SMP is initially processed into the original shape; when it has been deformed into the second shape it is exposed to a specific wavelength of radiation that creates new cross links which locks in the deformed shape. These cross-links can then be cleaved when it is exposed to another wavelength of radiation; returning the material to the original shape (Lendlein, et al., 2005). Other light activated systems use dyes to increase energy absorption of the same wavelength of the light source (laser) to provide the thermal energy needed for transformation (Maitland, et al., 2007).

Heat activated SMPs are commonly synthesized from polyurethanes (thermosets or thermoplastics), epoxies (thermosets), or acrylates (thermosets). These base materials can be made into a composite to tailor mechanical and thermal properties for a specific application. The Diaplex Company has synthesized some polyurethanes used in literature (Mitsubishi Heavy Industry Ltd. has made most of the SMP polyurethane foam), epoxy has been synthesized by Composite Technology Development (CTD) Incorporated (Liu, et al., 2004; Ohki, et al., 2004). Photo-polymerizable cross-linked acrylates have been studied for medical applications by university researchers (C. M. Yakacki, 2008; Christopher M. Yakacki, 2008; Ken Gall, 2005; Yakacki, et al., 2007). The light activated SMP is based off of cinnamic acid, which is photo responsive and forms the reversible cross-links. The cinnamic acid is combined with a polymeric backbone to form the SMP, and the exact polymer chemistry can be found in Lendlein et al., 2005 (Lendlein, et al., 2005).

1.2 Recovery Mechanism of Thermally Activated Cross-Linked Polymers

In thermally activated cross linked polymers, the shape memory effect is entropic in nature. When heated near the glass transition temperature (T_g) the polymer chains between network points can undergo rotational conformational changes, allowing the polymer chains to be uniaxially strained. As the material is strained, the alignment of the chains increases, which increases the stored energy in the material as the configurational entropy of the chain decreases. This energy is subsequently locked into the polymer chains when the material is cooled below T_g and the chains are restricted from freely rotating via interactions with their neighbors. When the polymer is reheated above T_g

without constraint, an increase of entropy serves as a driving force for the material to recover its initial shape (Lendlein and Kelch, 2002). The thermo-mechanical shape storage and recovery process is illustrated in Figure 1.1.

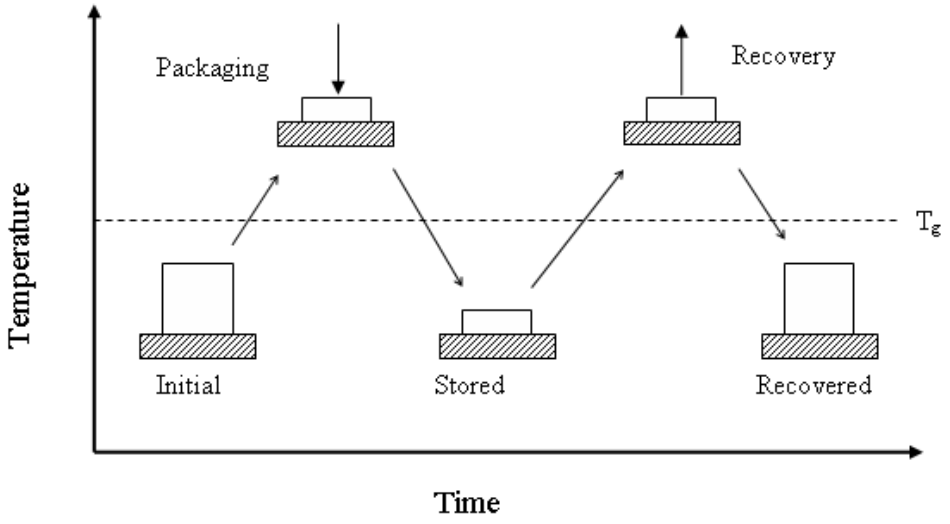

Figure 1.1 Shape Memory Cycle
The recovery step can also be used to package the material into another shape.

1.3 Shape Memory Polymer Research

As the shape memory mechanism is relatively well understood, other aspects of the material have also been studied. These works have considered 'pure' SMPs (Hayashi, et al., 1995; Hayashi, et al., 2004; Jeong, et al., 2000; Liu, et al., 2006; Tobushi, et al., 1996; Tobushi, et al., 2001) and SMP composites (Abrahamson, et al., 2003; Gall, et al., 2002; Gall, et al., 2000; Liu, et al., 2004; Ohki, et al., 2004). Work on 'pure' SMPs is widespread. It was found for shape memory polymer thin films that altering T_g shifted the mechanical properties in relationship to the new T_g (Tobushi, et al., 1996). Research to

develop constitutive models of the thermo-mechanical behavior has led to both 2D (Tobushi, et al., 2001) and 3D models (Liu, et al., 2006). Thermal characterization and studies of processing effects on material behavior have been performed (Hayashi, et al., 1995; Hayashi, et al., 2004; Jeong, et al., 2000) and potential applications for SMPs have been explored. Thermo-mechanical investigations similar to those performed in this work have been investigated for the 'pure' SMPs (Liu, et al., 2006; Tobushi, et al., 1996; Tobushi, et al., 2001).

To increase the stiffness and recoverable force levels in shape memory polymers, various researchers have developed SMP based composites (Abrahamson, et al., 2003; Gall, et al., 2000); including fiber-reinforced materials (Abrahamson, et al., 2003; Gall, et al., 2000; Ohki, et al., 2004) and nano-particulate reinforced materials (Gall, et al., 2002; Liu, et al., 2004). As the percentage of reinforcement increases, the modulus and recoverable force increase while the ductility and recoverable strain decrease (Ohki, et al., 2004). This tradeoff in properties facilitates tailoring of a shape memory polymer for specific application requirements.

1.4 Shape Memory Polymer Foam

Foaming the SMP is another means to tailor material properties for application requirements. Foams generally have reduced mechanical stiffness and strength but enhanced compressibility and unique relationship between axial and transverse strains (Poisson effect). The free volume inherent in the foam structure leads to cell collapse/buckling with increasing axial strain which does not lead to an increase in

transverse strain. The transverse strain becomes significant once the foam reaches the densification stage. In general, foams can be classified into three different types: (1) open celled for which the cells are interconnected by walls but the structure is permeable, (2) closed cell for which the cells are each enclosed by faces, resulting in an impermeable structure; and (3) a combination of open and close cells (2005). This distinction allows for a greater understanding of mechanical properties and more accurate modeling of foam materials. A variant of closed celled foam is created by infiltrating polymer around hollow spheres, called syntactic foam (Adrien, et al., 2007), while open cell foams with negative Poisson ratios are called auxetic foams (Scarpa, et al., 2004). Foams with open cells have been widely considered, and their internal structure and deformation mechanisms have been well characterized (Gong and Kyriakides, 2005; Gong, et al., 2005; Wang, et al., 2000; Zhou and Soboyejo, 2005). Other work has explored the effects of cell size distribution in modeling open cell foams (Roberts and Garboczi, 2001; Roberts and Garboczi, 2002; Schraad and Harlow, 2006). Work on closed cell foams has also focused on determining and modeling the collapse behavior of these foams (Du Bois, et al., 2006; Ehlers and Markert, 2003; Lim, et al., 2002; Lopatnikov, et al., 2007; Onck, 2001). Under compression, nearly all foams exhibit similar regimes of the stress-strain curve, as presented in Figure 1.2. In the initial elastic regime and during early yield, cell wall ‘struts’ deform uniaxially or bend. Subsequently, the struts buckle with increasing deformation and the material experiences plastic flow.

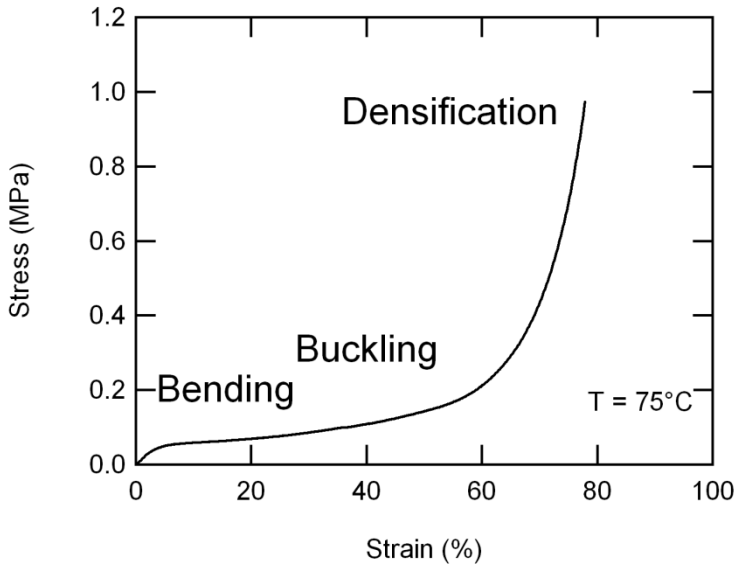

Figure 1.2 Compressive response of SMP foam.
In the elastic region the cell walls bend, from the yield point to the upswing ~60% strain, the cell walls buckle, and beyond buckling the cells wall make contact and densification begins. This testing temperature is below the T_g of the foam.

Eventually, upon exhaustion of this so-called plateau stage, cells collapse and compact as the strain is further increased and the stress-strain curve turns up toward higher stress at large strain (Ehlers and Markert, 2003; Schraad and Harlow, 2006).

Work to date on metallic and traditional polymer (elastomer) foams is much more extensive than that on SMP foams. The bulk of literature on SMP foams has covered open celled polyurethane systems produced by Mitsubishi Heavy Industries (Metcalfe, et al., 2003; Sokolowski W M, 1999; Tey, et al., 2001; Tobushi, et al., 2004; Tobushi, et al., 2001). The majority of this work concentrated on the long-term stability of foams that are 'frozen' in the deformed state; it was observed that even after six months the deformed foam could fully recover the imposed deformation (Sokolowski W M, 1999; Tey, et al.,

2001; Tobushi, et al., 2004). Other tests considered constrained stress and free strain recovery, cyclic properties, and strain rate dependence. These results demonstrated that full unconstrained recovery is possible from large compressive prestrains and that any external stress constraint inhibited full recovery but allowed for the foam to perform mechanical work (Tey, et al., 2001; Tobushi, et al., 2004; Tobushi, et al., 2001). Furthermore, there was no residual strain after cyclic compression when heated above T_g (Tobushi, et al., 2004) and the effect of strain rate on mechanical properties increases when the foam is heated above the T_g (Tobushi, et al., 2001).

1.5 Introduction to Micro-CT Scanning

Micro-CT scans refer to high powered/high resolution CT scans than have resolutions in the micron to tens of micron range. The scan works by directing x-rays at a spot on the sample and measuring the change in beam intensity as the sample is rotated through the machine (Keyak and Falkinstein, 2003; Ryan and Milner, 2006; Tuan and Hutmacher, 2005). The changes in intensity can then be used to create a 2D density map. This 2D density map is then turned into a binary image where the software defines which pixels are voids and which pixels represent material (Montminy, et al., 2004). This process of material definition is based on the user-defined threshold, which creates some error; a high threshold eliminates material, while a low threshold introduces too much noise (Tuan and Hutmacher, 2005). A series of these 2D maps is then compiled to produce the 3D image of the sample. A key advantage of this testing method is that it is non-destructive and it requires very little sample preparation (Tuan and Hutmacher, 2005). Another advantage of using CT scans is that it allows the computer model to accurately

represent the foam instead of using models and foam theory to develop a microstructure map (Montminy, et al., 2004).

Most work to date using CT scans has been done in the biomedical field (Keyak and Falkinstein, 2003; Ryan and Milner, 2006; Tuan and Hutmacher, 2005), but recently this technology has expanded to foam materials (Montminy, et al., 2004; Youssef, et al., 2005). Along with the high resolution and non-destructive nature, another key advantage to using the micro-CT instrument is that the data processing method (Montminy, et al., 2004) makes the transfer to FEM trivial (Keyak and Falkinstein, 2003; Montminy, et al., 2004; Youssef, et al., 2005). This allows for greater precision in creating models and inherently reduces error in comparing models to actual tests. The CT software also allows for quantitative analysis of relative density and pore size distribution. These foam characteristics can be used to determine how the microstructure evolves with applied strain. Micro-CT scanning can be used to non-destructively image complex 3D architectures and the output can be used as an FE mesh (A. Brydon, 2005; Adrien, et al., 2007; Lin, et al., 2003; Montminy, et al., 2004; Nagaraja, et al., 2005; Tuan and Hutmacher, 2005; Youssef, et al., 2005). This technique has been used successfully to fully characterize the microstructure of polymer foams(Montminy, et al., 2004) and to tie the microstructure to mechanical properties in porous polymers(Lin, et al., 2003). The next step has also been taken to analyze deformation response (M. A. Di Prima, et al., 2007) and to quantify material (Adrien, et al., 2007). Moving beyond scanning and observing deformation behavior, work has been performed using meshes of actual foam and performing FEA to simulate deformation of the material (A. Brydon, 2005; Youssef,

et al., 2005). This has been tied together by using a combination of scanning and modeling to perform damage prediction and analysis in porous bone (Nagaraja, et al., 2005).

1.6 Modeling of Foam

Although modeling of cellular solids has considered effects of mesostructure (cell shape, size, fraction of struts to joints, relative density, etc.), it has not been applied to shape memory polymers. The existing literature has covered the heterogeneous nature of the foam mesostructure (Roberts and Garboczi, 2001; Roberts and Garboczi, 2002; Schraad, 2007; Schraad and Harlow, 2006; Silva and Gibson, 1997) as well as cell size and specimen effects (Andrews, et al., 2001; Onck, et al., 2001). Work has also focused on the compressive behavior of open cell foams exhibiting elastic (Demiray, et al., 2007; Gong and Kyriakides, 2005; Gong, et al., 2005) and hyperelastic behavior (Danielsson, et al., 2004; Demiray, et al., 2006; Hohe and Becker, 2003). Limited research has specifically addressed damage evolution (P. Hard af Segerstad, 2007) and numerical simulations of mesoscopic damage effect on macroscopic behavior (James Ren and Silberschmidt, 2008). The literature also contains information on the constitutive modeling of nanocomposite foams (C. Jo, 2007) which may be applicable to SMP foams when they are reinforced with nanoparticles.

Using open cell foams models developed by Gibson and Ashby (Gibson and Ashby, 1997), the effect of relative density on the elastic stiffness was well approximated. The models were able to fit to the compression test data and were temperature independent above the T_g. The constrained stress relaxation behavior was shown to exhibit combined

viscous and thermal stress relaxation components. However, despite the capacity of macroscale models to fit specimen-level stress-strain response of the foams, they are incapable of accurately predicting local stress and strain distributions in the heterogeneous structure that are key to understanding progressive damage and failure processes. In particular, macroscale approaches have difficulty predicting peak local stresses that can drive local tensile failure and accumulation and coalescence of damage under cyclic loading. As such, Chapter 3 of this work will investigate how the three different mesostructures differ in terms of local mesoscale response to compression of test specimens.

To properly model SMP foam, a constitutive model of an SMP could be applied to the foam frame work. One constitutive modeling approach for SMP focuses on a two phase system (Barot, et al., 2008; Chen and Lagoudas, ; Chen and Lagoudas, ; Qi, et al., 2008; Y. Liu, 2006), with the material composed of "hard" and "soft" phases; the ratio of phases is determined by the temperature relative to T_g. The "soft" phases gain strain energy when the material is deformed above T_g; upon cooling the strain energy is stored in the "hard" phase until the material is heated again. While this simplification works to predict first order thermo-mechanical responses it is focused on specimen level behavior and does not account for local material behavior.

Lognormal cumulative probability distribution of cell level information (geometry and responses) is pursued in this work to model local structure response to compressive strains. It has been utilized for a number of purposes. Such distributions have been used

to fit the accumulation of dislocations on a plane versus the shear on that same plane (Beyerlein and Tomé, 2007) or recrystallization of austenite as a function of time under isothermal conditions (Quispe, et al., 2007). This approach to fitting also was used to model fatigue crack growth rate as a function of cycles and frequency (Chryssanthopoulos and Righiniotis, 2006) and to determine the 2D size distribution of particles from images (Sivakumar, et al., 2001). Each of these approaches employed slightly different forms and fitting parameters as appropriate to the specific application. Lognormal cumulative probability distributions have been used to correlate particle size distribution from impact testing (Cooper and Spielman, 1976), accumulation of calcium ions during fusion of proteins (Coorssen, et al., 2003), and substrate utilization sensitivity distributions (Boivin, et al., 2005).

1.7 Introduction to Epxoy Shape Memory Polymer Foam

The material systems for this work were provided by Composite Technology Development (CTD) Inc and were all epoxy based SMP. The chemistry and processing of the foams is proprietary to the company, so no chemical analysis of the materials was ever performed. Two different epoxy chemistries were provided in both resin and foam form, TEMBO 3XE and DP5.1. Foam composites were all based on the DP5.1 system and encompassed both magnetic nanofillers and vapor grown carbon fiber (VGCF). Differing relative densities of DP5.1 foam were also provided to determine effect of foam structure on properties. These materials are unique as the bulk of SMP foam literature has focused on polyurethane foams at low relative densities, 5 – 10%, (Metcalfe, et al., 2003; Sokolowski W M, 1999; Tey, et al., 2001; Tobushi, et al., 2004; Tobushi, et al., 2001).

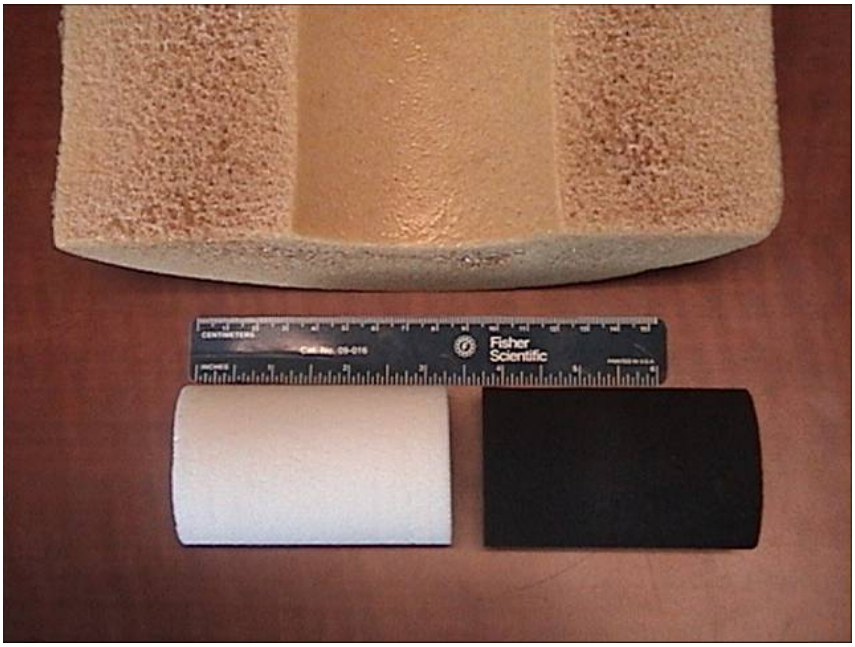

Figure1.3: Examples of CTD's Epoxy SMP foam.
The three primary supplied foam types are shown; TEMBO 3XE (upper center), DP5.1 (lower left), and reinforced DP5.1, in this instance with VGCF, (lower right).

1.8 Introduction to Thermomechanical Testing

Thermally activated shape memory polymers mechanical properties are highly dependent on temperature with respect to the glass transition. Since most applications envisioned for SMPs and SMP foams require the material to operate within this range, gaining understanding of how mechanical properties vary as a function of temperature is critical. Recent literature has shown that the testing temperature must be performed in relationship to the glass transition temperature for it to have any real significance (Safranski and Gall). As such the glass transition temperature must be properly measured for each material, and confirmed between batches, to insure that results can properly be compared.

The primary tool used to accomplish this was a Dynamic Mechanical Analyzer (DMA). The DMA oscillates a sample, for this material a tensile fixture was used, at a specified preload and strain while the temperature is increased at a constant rate. As the material undergoes the viscoelastic transition the deformation response comes out of phase from the applied stress and the modulus can be broken into a real component called the storage modulus (in phase) and an imaginary component called the loss modulus (out of phase). The ratio of the two is called the tan delta, delta being the phase angle between applied stress and strain amplitude (Rubinstein and Colby, 2003). We consider the glass transition temperature to be at the peak of the tan delta as this is where the ratio of the modulii are maximized and it is an easily defined point. A TA Instruments Q800 DMA was used in strain controlled mode operating at a frequency of 1 Hz. Exact testing procedure will be discussed in the appropriate section in each chapter.

The Differential Scanning Calorimeter (DSC) is another tool that was used to determine the glass transition temperature as well as other important thermal properties. The DSC consists of two very sensitive thermocouples inside a small furnace. An empty pan is placed on one of the thermocouples, to remove the effect of the pan, and the material sample is placed in a pan on the other sample. As the temperature inside the furnace changes, the thermocouples measure the temperature difference to calculate heat flow through the pans and the difference between the two heat flows can be plotted against temperature to illustrate when the sample material undergoes phase changes. For this project, the DSC provides the specific heat of different SMP foam samples as a function of temperature to allow for the energy to increase temperature to be properly calculated

via ASTM E1269 (2005). Using a TA Instruments Q100 DSC, samples were massed into aluminum pans (5 to 20 mg) and then run using a heat/cool/heat cycle from 0°C to 150°C at a rate of 2.5°C/min and a N_2 purge of 10 ml/min. Running a heat/cool/heat test removes the thermal memory of the sample when only the second heat cycle is analyzed.

Once the glass transition temperature was fully established, the bulk of the mechanical properties were determined with a uniaxial mechanical load frame produced by MTS, referred to by its product name Insight. The Insight is an electromechanical load frame, not hydraulic, and is displacement controlled. Displacement control means the crosshead, the part that moves to deform the specimen, moves at a rate specified by the user. To deform a sample under load control, a Proportional-Integral-Derivative (PID) controller must be programmed to insure the crosshead will move at a variable rate to provide the appropriate load control. As a result, all tests were run under displacement control with the displacement rate calculated based on sample geometry to maintain the specified engineering strain rate. A third party thermal chamber was used in conjunction with the Insight and had a temperature range of -50°C to 150°C. For precise strain measurements and free strain recovery a MTS LX300 Laser extensometer which has 1μm resolution was used. This set up allows for stress and strain to be plotted against each other or by either temperature or time. The largest load cell available for the Insight was 2 kN. For tests exceeding that load an Instron 5580 with attached thermal chamber was used. The Instron 5580 operates under the same principles as the Insight.

CHAPTER 2: THERMO-MECHANICAL BEHAVIOR OF EPOXY SHAPE MEMORY POLYMER FOAMS

2.1 Introduction

Shape memory polymer foams have significant potential in biomedical and aerospace applications, but their thermo-mechanical behavior under relevant deformation conditions is not well understood. In this chapter we examine the thermo-mechanical behavior of epoxy shape memory polymer foams with an average relative density of about 20%. These foams are deformed under conditions of varying stress, strain, and temperature. The glass transition temperature of the foam was measured to be approximately 90°C and compression and tensile tests were performed at temperatures ranging from 25°C to 125°C. Various shape recovery tests were used to measure recovery properties under different thermo-mechanical conditions. Tensile strain to failure was measured as a function of temperature to probe the maximum recovery limits of the foam in both temperature and strain space. Compression tests were performed to examine compressibility of the material as a function of temperature; these foams can be compacted as much as 80% and still experience full strain recovery over multiple cycles. Furthermore, both tensile strain to failure tests and cyclic compression recovery tests revealed that deforming at a temperature of 80°C maximizes macroscopic strain recovery. Deformation temperatures above or below this optimal value lead to lower failure strains in tension and the accumulation of non-recoverable strains in cyclic compression. Micro-computed tomography scans of the foam at various compressed states were used to understand foam deformation mechanisms. The micro-CT studies revealed the bending,

buckling, and collapse of cells with increasing compression, consistent with results from published numerical simulations.

2.2 Experimental Method

2.2.1 Materials and Specimen

The material used in this work was an epoxy foam with the trade name TEMBO® 3XE provided by Composite Technology Development (CTD). Chemical and processing details of the material are proprietary, but the material can be considered essentially as a two-part thermoset epoxy network. The foam's initial mean cell diameter is 0.472 mm, determined by MicroCT scans, and a density of 0.2 g/cc, resulting in a relative density of 17%. Samples for the Dynamic Mechanical Analysis (DMA) were rough cut and sanded to rectangular prisms with dimensions 10 by 6 by 2 mm. The compression test samples were each rough cut to rectangular prisms 17 by 17 by 20 mm and then punched into cylinders with a diameter of 13.5 mm and height of 20 mm. The cylindrical specimens were then thermally cycled above the T_g to remove any strain imposed during sample preparation. Tensile specimens, 0.5 scaled ASTM D 638-03 Type IV dog bone specimens, were laser cut from sheets of foam 2 to 3 mm thick. The ends of the dog bones were wrapped in aluminum foil to prevent slippage and failure in the grip region. Since the tensile specimens were too small to unambiguously constitute a representative volume element (RVE), given average pore diameter, multiple duplicate tests were conducted in tension to explore repeatability of results.

2.2.2 Experimental Apparatus

To determine the T_g, a Thermal Analysis DMA Q800 was used with film tension clamps. The remainder of the tests were performed using a MTS Insight 2 uniaxial mechanical test frame with an attached thermal chamber. A thermocouple was located inside the thermal chamber and was placed adjacent to the sample. Negligible differences were observed between displacement measurements taken using the machine cross head and those taken with laser extensometer in compression; accordingly, the former were used for convenience. MTS high load capacity compression platens (643.10A-03) were used to compress the foam cylinders. MTS Advantage Screw Action tensile grips and a MTS LX300 laser extensometer were used for the tensile testing.

2.2.3 Experiments

Six types of tests were performed to measure bulk properties/responses: DMA, compression, block compression, tensile, cyclic loading, and shape memory. The shape memory tests were further composed of free strain and constrained shape recovery tests.

DMA. The foam specimens were wrapped with aluminum foil at the ends to avoid the occurrence of fracture in the grips. With the use of a torque wrench, the upper clamp was tightened to 0.11 Newton meter of torque and the lower clamp was tightened to 0.22 Newton meter of torque, to insure uniform stress on the sample. The sample was equilibrated at 25°C for two minutes and then heated to 150°C at a rate of 5°C/min. The test was run under engineering strain control; with a strain of 0.1%, a preload of 0.01 N, a force track rating of 150%, and a frequency of 1 Hz. The strain value of 0.1% keeps the material in the linear viscoelastic region

Compression tests. The tests were conducted at five different temperatures: 25°C, 50°C, 75°C, 100°C, and 125°C. To ensure uniform heating, the thermal chamber and each specimen were held at temperature for ten minutes at each temperature. To achieve full contact of the platen on the sample, a preload of 0.2N was used. The cross head speed was set at a rate of 3mm/min for a strain rate of 0.0025 s^{-1}. The sample was compressed to a load of 1950 N, nearly the maximum load for the test frame, and unloaded at the same strain rate until the minimum preload was again reached. Three specimens were run at each temperature to investigate repeatability of trends.

Block compression experiments. In this test, the specimen was loaded to the first strain point, unloaded until the desired preload was reached, reloaded to the second strain point, until the load limit was reached. This sequence was run at five different temperatures: 25°C, 50°C, 75°C, 100°C, and 125°C. The strain end points for each temperature were determined by taking the maximum strain from the compression test and dividing it into eight equal segments. To ensure uniform temperature for each specimen, the thermal chamber was held at each temperature for ten minutes. To maximize resolution and test range, a 2kN load cell was used for the 25°C, 50°C, and 75°C tests and a 100 N load cell was used for the 100°C and 125°C tests. The load limit for the 2k N load cell was set to 1950 N and the 100 N load cell was set to 95 N to prevent damage to the load cells. To ensure full contact of the platen on the sample, a preload of 0.2 N (2 kN load cell) or 0.075 N (100 N load cell) was used. The cross head moved at a rate of 3 mm/min for an

engineering strain rate of 0.0025 s^{-1}. Three specimens were run at each history to investigate the repeatability of trends.

Tensile experiments. Tensile specimens were loaded using MTS Advantage Screw Action tensile grips with an engineering strain rate of 0.0025 s^{-1} until failure. After wrapping the ends in aluminum foil and measuring the width and thickness of the gauge length, a piece of laser tape was placed on both ends of the nominal gage section of the dog bone. The nominal gage length, used for calculations of strain, was measured prior to and during testing with the laser extensometer. The use of laser tape did not appear to adversely affect the results, as the specimens failed in the center of the gage region as often as they failed near the laser tape. The specimen was placed in the tensile grips so that the laser tape was facing the thermal chamber door, and the thermal chamber heated to the appropriate temperature. Specimens were tested at temperatures of 25°C, 50°C, 65°C, 70°C, 75°C, 80°C, 85°C, 90°C, 95°C, 100°C, 125°C, and 150°C. To ensure uniform temperature, specimens were held at each temperature for ten minutes prior to testing. Three specimens were run at each temperature to investigate the repeatability of trends.

Cyclic loading experiment.. In this test, each specimen was cyclically compressed in the load frame to a set strain endpoint for one hundred cycles. The cylindrical specimens were compressed with an engineering strain rate of 0.0025 s^{-1}. The temperatures of interest for this test were 80°C, 100°C, and 125°C. Engineering strain end points were 40%, 60%, and 80%. Specimens were held at temperature for 10 minutes prior to starting each test. For the tests at 80°C, the sample was subsequently heated to 100°C to promote

recovery and then cooled back to 80°C, since at this testing temperature instantaneous (rubbery) recovery was not observed. With this extra step, the tests at 80°C were only cycled twenty times in light of excessive testing time. For the best resolution, a 100 N load cell was used with a load limit of 95 N (the load limit was set but not used). To promote full contact of the platen on the specimen, a preload of 0.075N was used.

Shape storage. Shape storage is the first step for both constrained recovery and free strain recovery. The specimen was heated to the packaging temperature and compressed to a strain of 80%. This compression was maintained as the specimen was cooled to 25°C and the platen was raised when there was no longer a stress registering on the load cell. Packaging temperatures of 100°C and 125°C were used.

Constrained recovery. The packaged specimens were placed into the MTS Insight 2 mechanical test frame, with a 100N load cell and attached thermal chamber, and compressed at room temperature to a preload of 0.5N. The compression platen was then raised 0.3 mm to take into account thermal expansion. The platen was then held at that position as the temperature was increased from 25°C to 145°C at a rate of 2°C/min. The stress exerted by the specimen on the platen was then recorded versus time, which was correlated to the temperature.

Free strain recovery. A square glass slide, with laser tape along the edge facing the extensometer, was set on top of the packaged specimen. The specimen was then placed on a single compression platen, also with laser tape on the edge (facing the extensometer

and parallel to the glass slide), in the MTS Insight 2 with attached thermal chamber. Three aluminum blocks surrounded the specimen to prevent it from falling over during the recovery process. The specimen was then heated from 25°C to 145°C at a rate of 2°C/min, while the MTS LX300 laser extensometer recorded the displacement of the two pieces of laser tape. This displacement was used to determine the percent strain recovered and plotted against the temperature (again correlated with time).

X-ray micro-CT scanning. Various samples of interest were scanned using a Scanco Medical vivaCT 40 x-ray micro-CT scanner at the Georgia Institute of Technology Orthopedic Bioengineering Laboratory. The nondestructive nature of micro-CT imaging allows for iterative scanning. A single specimen was scanned and then compressed to 10% strain; the specimen was then rescanned and compressed to another 10% strain of the original height. This process continued until the sample was compressed to a strain of 80% of the original height. Isolation of the same foam region across the scans was performed manually using ImageJ software for comparison and image alignment. MRIcro software was used for fine tuning the area selection and the generation of the 3D images. Bulk foam properties were determined using the ScanCo analysis software.

2.3 Results

A selected pair of storage modulus and tan delta curves from the DMA test are shown in Figure 2.1; the differences between the resin and foam versions of the base material are readily visible. The T_g of the foam is seen to be 92°C +/- 3°C, using the peak of the tan

delta, with the onset near 75°C and the completion near 110°C. Figure 2.2 contains the results of testing a) simple compression and b) block compression samples.

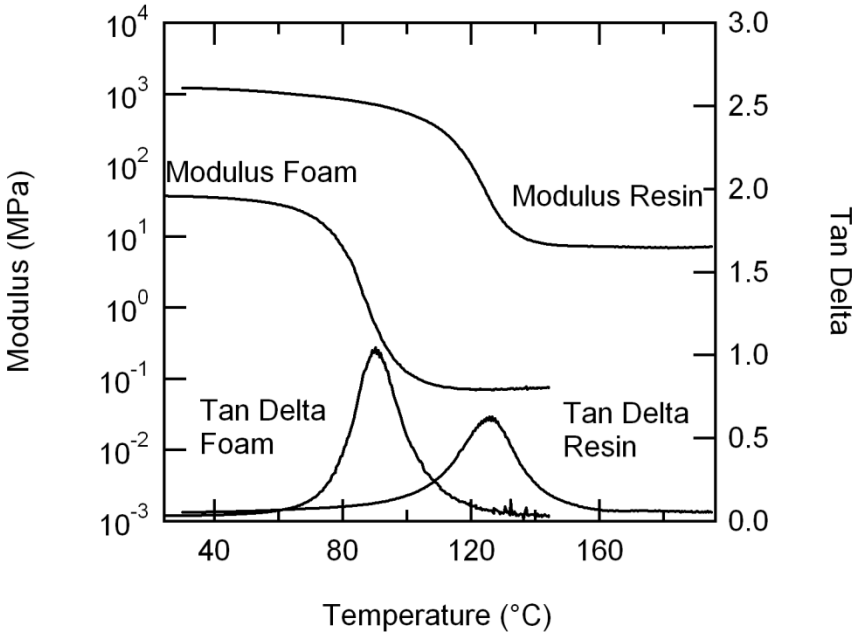

Figure 2.1 :DMA results of TEMBO 3XE Foam and Resin

From Figure 2.2(a), it is seen that as the temperature increases so does the strain needed to fully compress the material. The overlay of the curves from Figures 2.2(a) and 2.2(b) indicates that the block compression testing does not alter the mechanical properties in relation to the simple compression test. Figure 2.2(c) compares the low strain regions of the five temperatures and the log scale reveals the magnitude in the shift of the mechanical properties at small strains between the temperatures.

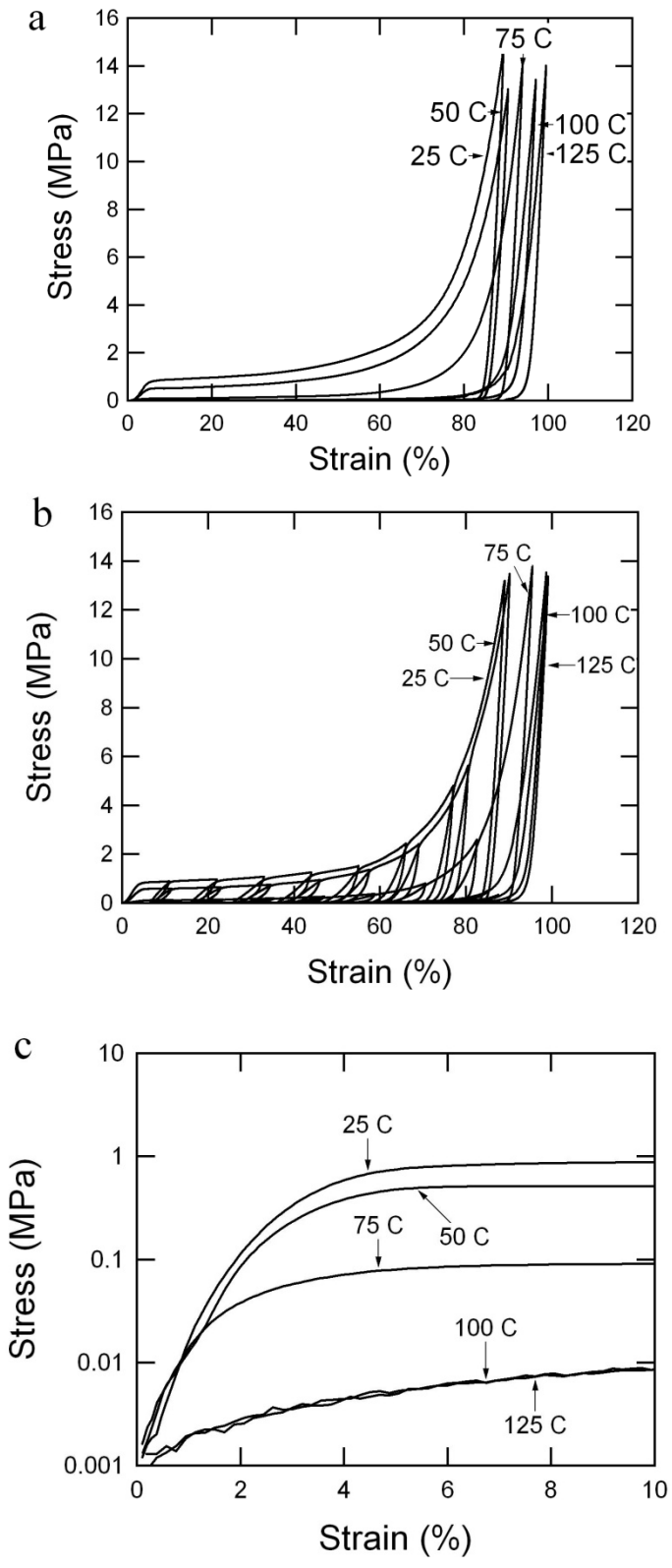

Figure 2.2: Compression response as a function of temperature.
(a) simple compression and (b) block compression (c) log scale of low strain region.

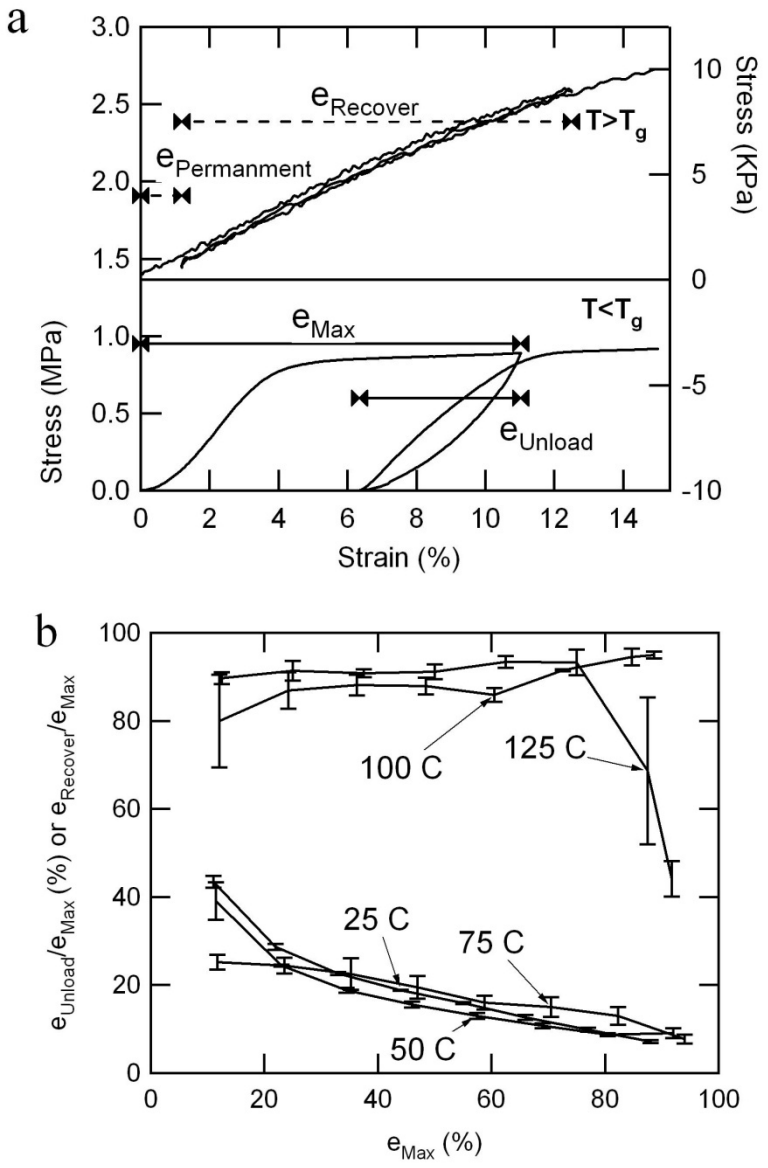

Figure 2.3: Analysis of block compression testing.
(a) defining maximum strain, unloaded strain, permanent strain, and recovered strain. Recovered strain and permanent strain arise when the specimen is heated above the T_g. (b) A plot of recovered strain in terms of maximum strain by maximum strain and temperature effect.

Figure 2.3(a) illustrates the loading path for the block compression test and the definition of the maximum strain (e_M) and recovered strain (e_R). Figure 2.3(b) shows the effect of the maximum strain and the testing temperature on the materials' ability to recover strain.

At temperatures below T_g the only strain recovered is elastic strain (roughly constant), so the ratio of e_M to e_R decreases as the maximum strain increases. The influence of T_g on spontaneous shape recovery (rubbery behavior) is indicated by the difference of strain recovery in the samples run at 100°C versus the samples run at 75°C.

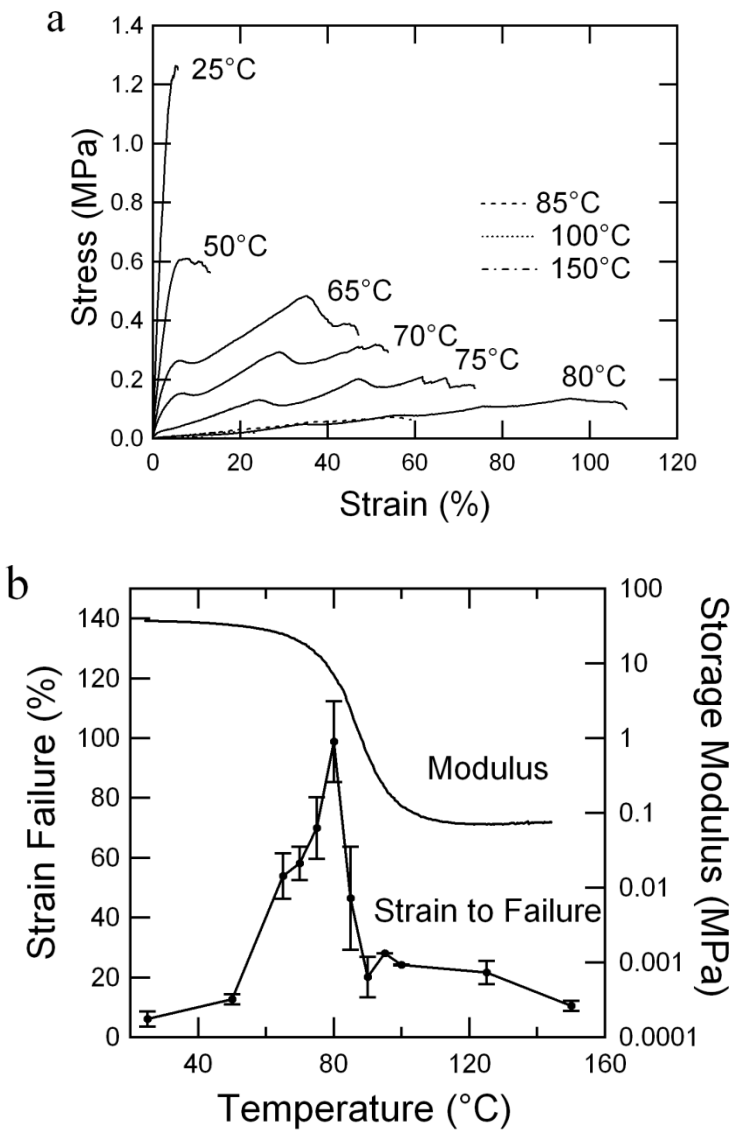

Figure 2.4: Tensile Response of TEMBO 3XE as a function of temperature.
(a) select tensile curves at each temperature to show failure peak, (b) average strain to failure versus various temperatures overlaid with storage modulus versus temperature.

The results of the tensile testing at various temperatures are presented in Figure 2.4. Figure 2.4(a) plots the tensile strain to failure versus temperature and compares it to the storage modulus. The error bars mark one standard deviation from the mean strain to failure for n = 3. Figure 2.4(b) is an overlay of selected tensile curves for each temperature which forms the failure peak (Gall, et al., 2007; Smith, 1963). These plots show that the optimum temperature to maximize tensile strain is at approximately 80°C, which is below T_g but at the peak of the loss modulus, as measured by DMA.

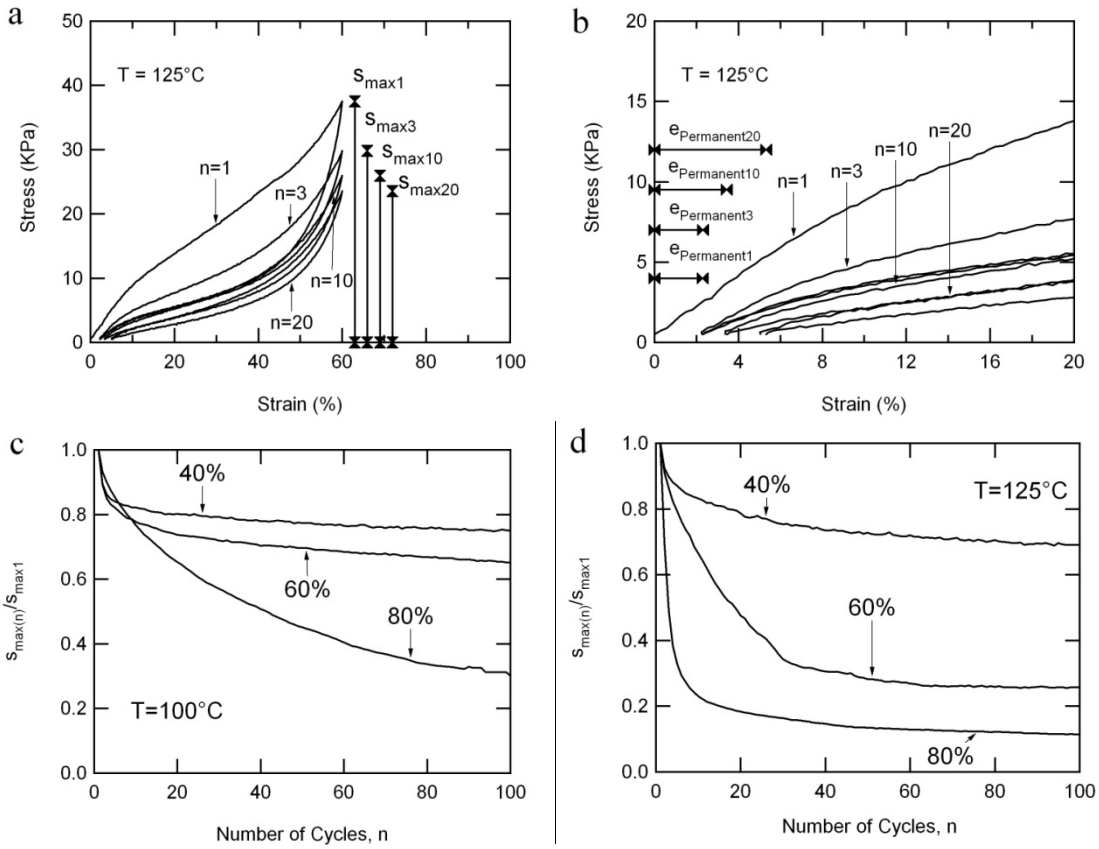

Figure 2.5: Effect of cycling on the maximum stress at a set strain for TEMBO 3XE. (a) Shows selected cycle curves and defines the maximum stress, (b) shows same selected cycle curves at a smaller strain region and defines permanent strain. (c) Effect at 100°C and d) 125°C. The curves are labeled with the strain end point.

The results from the cyclic loading series (brought to 100 cycles) are presented in Figure 2.5. Figure 2.5(a) has selected cycle curves and defines the stress nomenclature at the strain end point while Figure 2.5(b) defines the permanent strain from each cycle. Figures 2.5(c) and 2.5(d) show the maximum stress achieved at the strain end point versus cycle number. The stress is normalized to the stress at the strain end point for the first cycle to allow comparison across temperature and strain end points. The trend is a sharp drop in the first few cycles, followed by a plateau of the normalized stress. Figure 2.6 compares the unrecovered strain from the cycling for the first 20 cycles to allow comparisons of the cyclic series at 80°C (which was only subjected to 20 cycles due to excessive testing time incurred during intermittent reheating to 100°C). Figure 2.6(a) compares the samples compressed to 40%, Figure 2.6(b) compares the samples compressed to 60%, and Figure 2.6(c) compares the samples compressed to 80%. The temperature and maximum strain level has a significant effect on reversibility (accumulation of permanent strain) in the temperature range near T_g and close to the maximum strain capacity of the material. It is important to notice the difference in the scales of Figures 2.6(a)-2.6(c) as temperature effects on reversibility only become significant at higher applied strain.

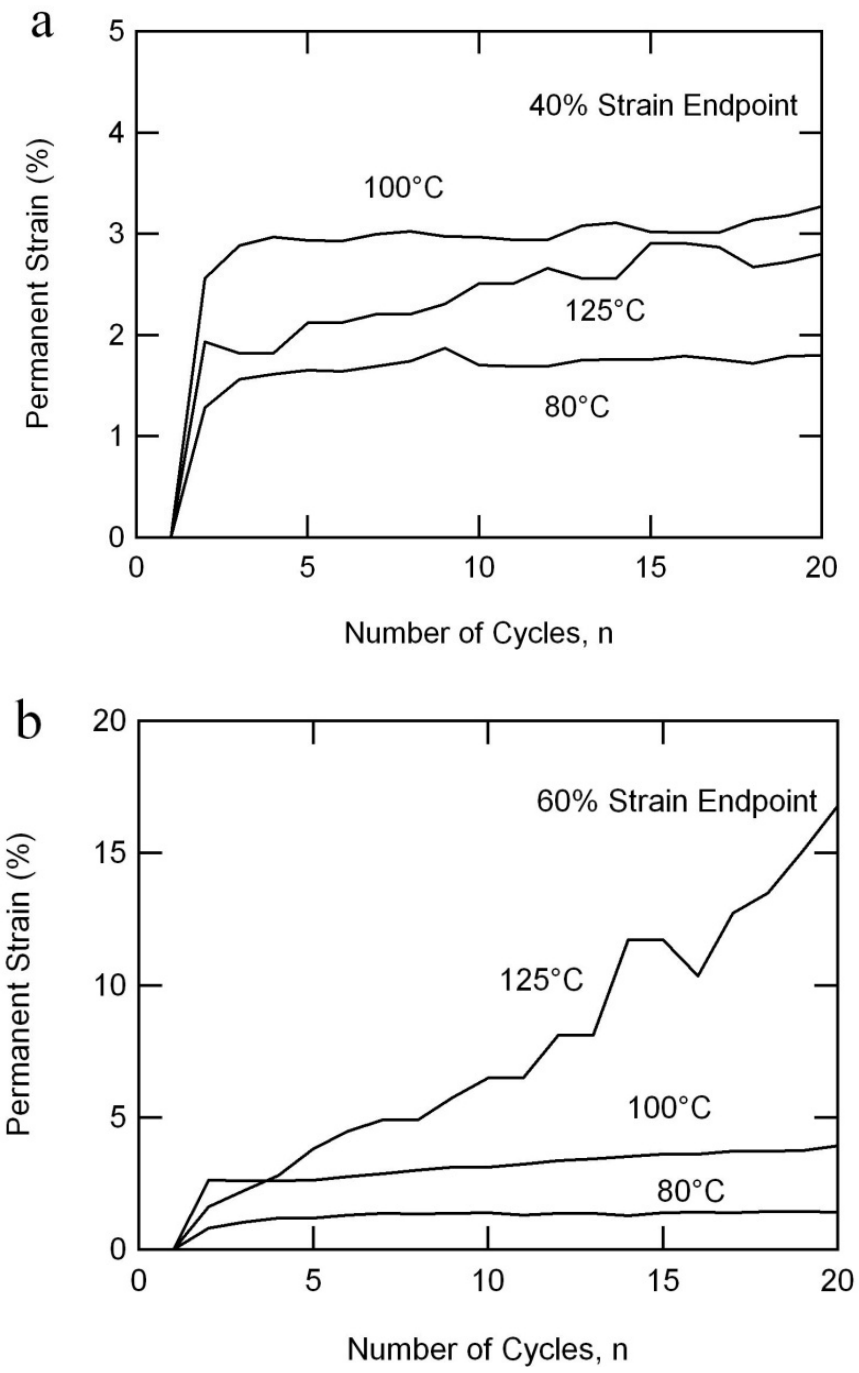

Figure 2.6: Temperature dependence of permanent strain during cyclic loading for TEMBO 3XE. Strain endpoints of (a) 40% compressed, (b) 60% compressed, and (c) 80% compressed. At 40% compressed the testing temperature has no significant effect on the permanent strain.

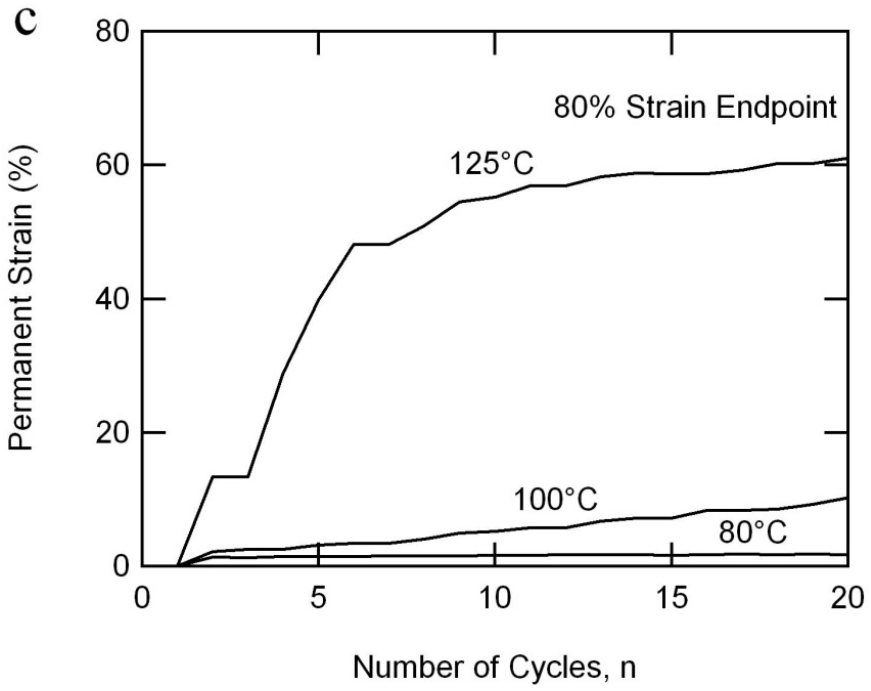

Figure 2.6 Continued

The constrained recovery tests show that the specimen packaged at 100°C begins exerting stress at a slightly lower temperature than when the specimen is packaged at 125°C, as shown in Figure 2.7(a). Furthermore, the foam packaged at 100°C exerts a greater force than when the foam is packaged at 125°C. The results from the free strain recovery test, Figure 2.7(b), demonstrate that the packaging temperature does not affect the overall recovery strain level, only the onset temperature of strain recovery.

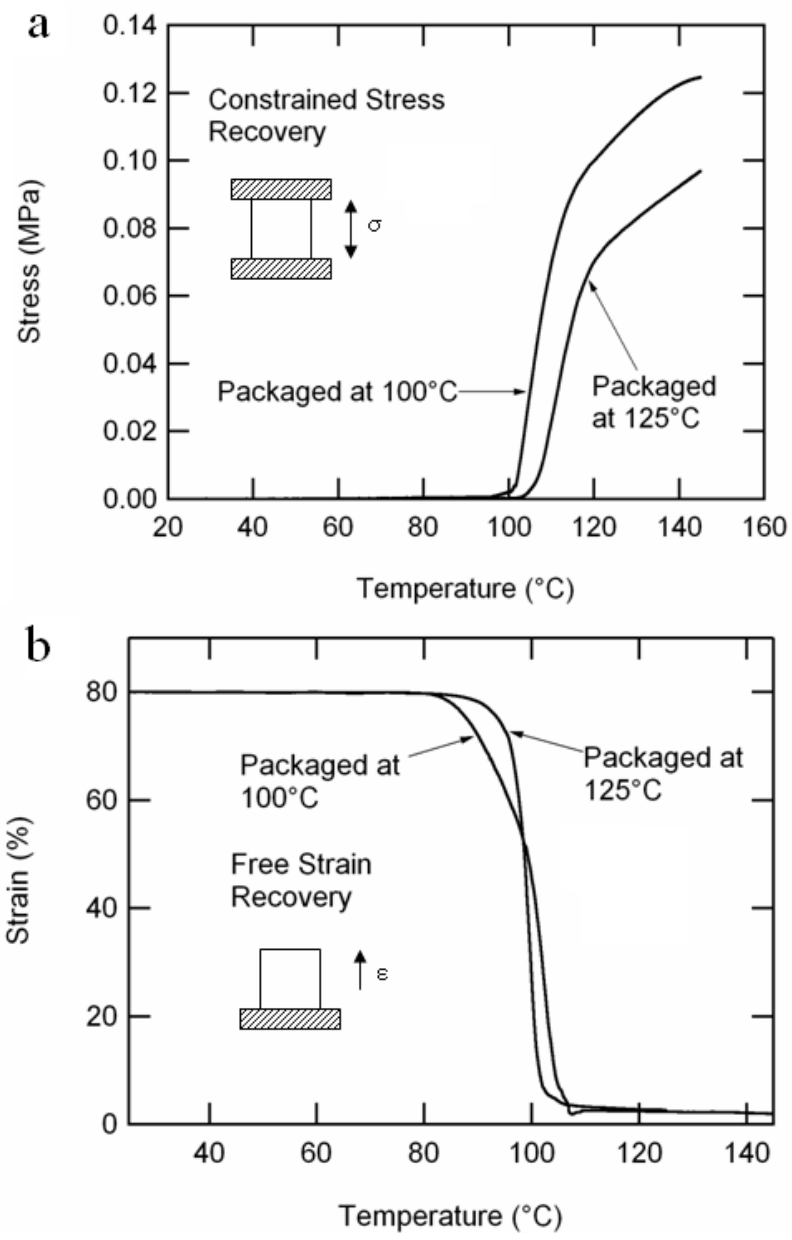

Figure 2.7: Recovery response at differing packaging temperatures for TEMBO 3XE. Packaging temperatures of 100 and 125°C were used for a) constrained stress recovery and (b) free strain recovery.

In a high resolution CT scan, the cells in the undeformed foam are highly spherical (Figure 2.8). Furthermore, the wall thickness is nonuniform across the cell to cell interface.

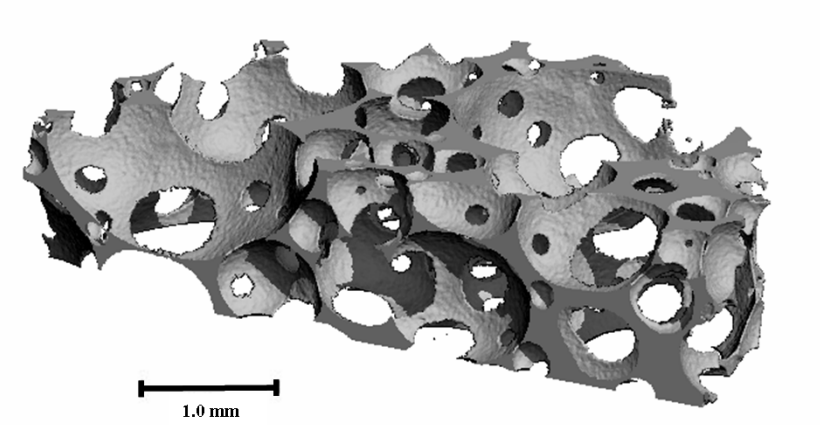

Figure 2.8: 6μm resolution x-ray micro-CT image of TEMBO 3XE.

While the high resolution (6 μm) scan captures more of the cell wall than the 20 μm scan in Figure 2.9(b), the overall structure is the same. The response of the cell to deformation is tracked in Figure 2.9; cell response to strain (with the stress-strain curve for superimposed comparison) is plotted in Figure 2.9(a), while (b) shows micro-structural snapshots at increasing strains. The average cell size drops less than 10 percent in the first 10 percent of strain but then rapidly decreases until ~45 percent strain. After this point the decrease in the average cell size begins to slow. The snapshot of the foam structure shows that buckling of the main cells did not occur, on average, until the sample was compressed to 20 percent strain and that densification started near 40 percent strain. Each of the snapshots shown correspond to a volume of 2mm by 2 mm by 0.8 mm. Figure 2.9c shows histograms of cell size (cell wall spacing) for selected strain levels, showing that the distribution of cells sizes changes along with the average cell size.

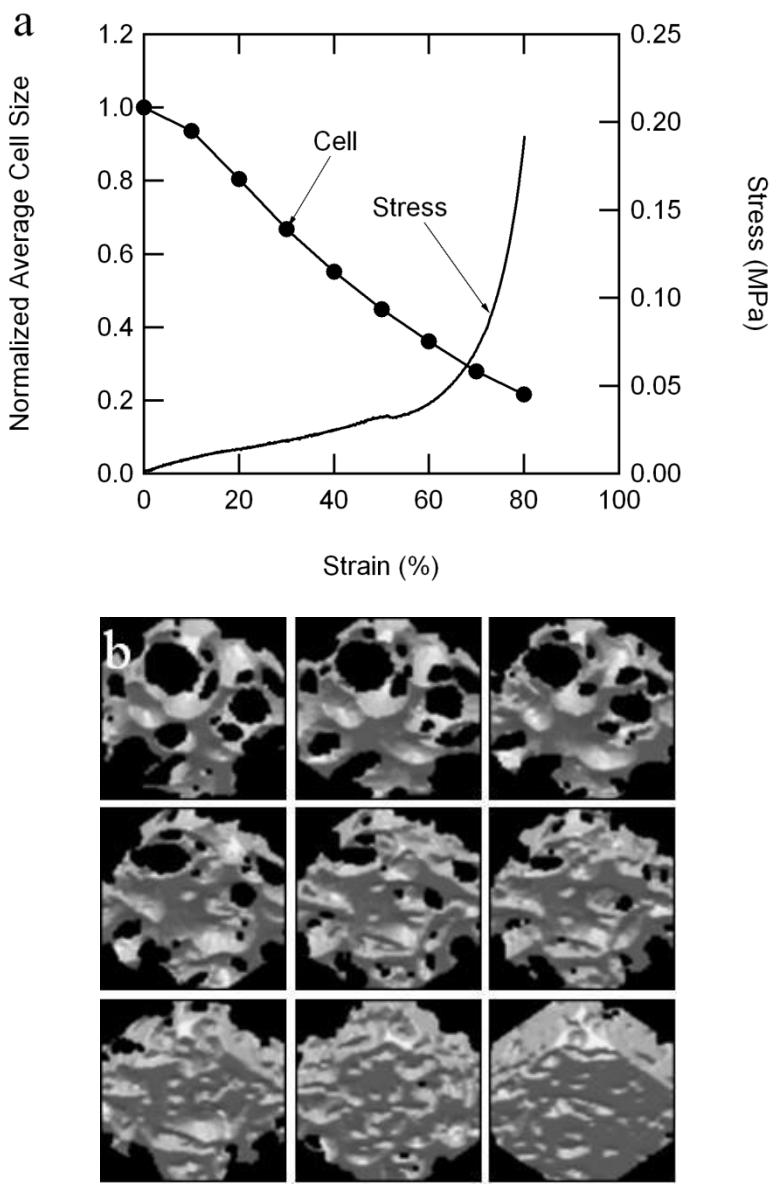

Figure 2.9: Microstructure response of TEMBO 3XE to deformation at 125°C.
(a) Plot of average cell size versus strain, stress-strain plot is included for comparison. (b) Snap shot of the same 2x2x0.8 mm foam region during deformation at 10% strain intervals. Reads left to right, top to bottom starting at un-deformed and ending at 80% compressed. (c) Selected histograms of cell wall spacing vs. count number of the foam as its being deformed.

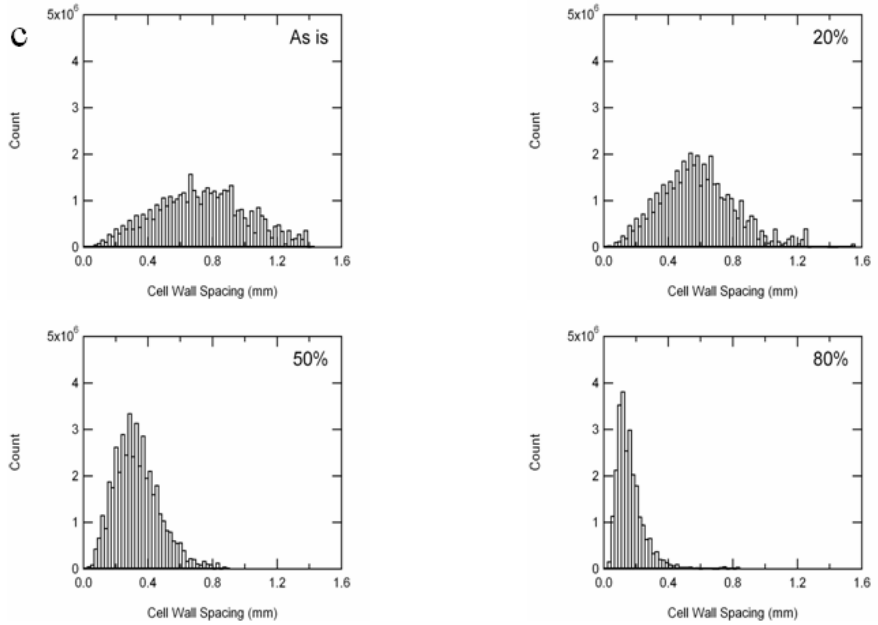

Figure 2.9 continued

2.4 Discussion

The results obtained here provide a foundation to better understand the thermo-mechanical behavior of shape memory polymer foams for emerging applications. The epoxy-based foams considered here are most applicable in the aerospace field, but some of the overarching results can be extended to other foam systems, especially thermoset networks. The compressive monotonic stress-strain results provide key information on the stiffness and compressibility of the foams as a function of strain level and temperature. The compressive stress-strain response, as a function of temperature, also provides a substantial input into constitutive modeling of the shape memory polymer foams. The tensile monotonic results provide key information on the ductility of the foams and the optimal temperature for deforming the foams without damage (under tension or compression). The cyclic results extend durability concepts to multiple loading

cycles and provide increased sensitivity to local damage through changes in the stress-strain response (maximum stress, elastic modulus) with cycling. Fundamentally, the cyclic results reveal local damage evolution trends that may not be evident under monotonic loading. From an application perspective, the cyclic results provide more conservative temperature and strain limits for the polymers to avoid failure as failure occurs at a lower threshold than monotonic testing. The free strain recovery test provides insight into the effect of deformation temperature on required actuation temperature while the constrained stress recovery test quantifies actuation work output. Finally, the micro-CT scanning provides some insight into the deformation mechanisms operating during foam compaction, although further work is surely needed to understand local deformation mechanisms operating during monotonic and particularly cyclic deformation.

The results from Figure 2.1 were used to determine the relative test temperatures for the thermo-mechanical testing. From this plot, the five temperatures of interest for the thermo-mechanical testing were chosen to be 25°C, 50°C, 75°C, 100°C, and 125°C, corresponding respectively to room temperature, the glassy phase, the transition onset, the transition completion, and the rubbery phase. This provides a map of the mechanical properties over the full range of possible temperatures that the material could see in a shape memory cycle. Compression tests at these various temperatures are critical for future constitutive modeling efforts.

Post recovery analysis with calipers has shown full to nearly full recovery in samples that are heated above T_g to induce recovery. While Figures 2.3(b) and 2.7(b) show that a great deal of strain is recovered, they do not show the full recovery that is observed after the test. In the case of Figure 2.3(b), the slight minimum preload from the compression platen (0.075N) is preventing complete recovery in the course of the test. This effect was observed when the 100 N load cell was used instead of the 2 kN load cell as the strain recovered increased when the minimum load was dropped from 0.5 N to 0.075 N. These minimum loads were required to maintain contact between the compression platens and the specimen. Using a microscope slide as a marker for the free strain recovery tests (Figure 2.7(b)) should have eliminated the effect of a load on the shape recovery and in fact the test shows greater strain recovery than Figure 2.3(b). However, the test still does not show the full strain recovery that is observed when the specimen is removed from the thermal chamber and measured by hand. This is due to the measurement error introduced by measuring specimen height before the specimen thermally expands in the thermal chamber.

Figure 2.3(b), which leads to Figure 2.5(c), confirms the significance of the temperature for strain recovery in this foam system. The clearest indication is the change in trends for temperatures above and below T_g. An unexpected result was that at the highest temperature, 125°C, the strain recoverability repeatedly dropped after being compressed to 80% strain (Figure 2.3(b)). This suggests that this temperature and strain are beyond the ‘optimal’ conditions for this material to recover strain. This is reinforced by the results of Figure 2.5; where the cyclic response of the material being compressed to 80%

strain at 100°C strongly deviates from the other curves. There is, however, little difference between the curves for 40% and 60% strain, indicating that the temperature increase alone (both above T_g) is not enough to degrade the material's performance. The general trend of these curves, except for the aforementioned 80% strain at 125°C, is supported by the literature on the cyclic properties of SMP foams (Tobushi, et al., 2004; Tobushi, et al., 2001), although the polyurethane foams exhibited a lower drop in normalized stress. However, the permanent strain trend from cyclic deformation is very similar to that reported for cyclically deforming polyurethanes (G. Baer, 2007). Polyurethanes typically need to be pre-conditioned; a process which removes any chain irregularities and relaxes dangling chains, which accounts for the behavior in the first few cycles of the SMP polyurethanes. The epoxy material being a thermoset, should be less susceptible to this phenomena but the experimental results suggests that some cyclic degradation mechanisms are acting. Future work will investigate the structural response to cyclic loading of SMP foams to determine which mechanism is responsible for this cyclic trend in thermo-sets.

The peak in the tensile strain to failure versus temperature in Figure 2.4(a) was a surprising result. This peak is theorized for elastomeric materials (Smith, 1963) and has been recently confirmed in other SMP networks (Gall, et al., 2007); it is not unique to this material system. We speculate that this peak signifies that the effects of material and/or structural defects are minimized at the peak, 80°C, where the material has enough viscoelasticity to suppress local damage in the polymer and the loss modulus is maximized. This prompted a return to cyclic testing to investigate whether compressive

packaging at this temperature led to an increase in performance. Figure 2.6 shows that cyclic loading at 80°C exhibits less permanent strain (which we speculate corresponds to less damage) than the other testing temperatures at all three strain levels. As such, the peak in the tensile strain to failure does predict the optimum packaging temperature of the material to minimize damage during cyclic loading and unloading. It is interesting that this toughening mechanism may be used effectively in shape memory polymers, but not traditional elastomers since the latter materials are required to exhibit spontaneous strain recovery rather than strain recovery upon reheating.

The shape recovery tests, especially constrained stress recovery, show a dependence on the packaging temperature. In Figure 2.7(a) there is a noticeable difference in the stress-temperature curve between specimens packaged at 100°C and 125°C. At 100°C, the material is still in the glass transition region, as seen from the DMA data in Figure 2.1, which can account for the increase in constrained stress. The packaging temperature, as previously mentioned, affects the strain recovery onset and offset in the free strain recovery test. From Figure 2.2b, the specimen packaged at 100°C has an early onset and later offset of shape recovery than the specimen packaged at 125°C. Like the differences in the constrained stress recovery, this difference is most likely due to the viscous behavior of the specimen packaged at 100°C.

As previously discussed, foam materials have three stages of deformation; bending, buckling, and densification (Ehlers and Markert, 2003; Schraad and Harlow, 2006). The results from Figure 2.9 show that the epoxy SMP foam deforms in a manner consistent

with these three stages. The initial small drop in cell size in Figure 2.9a can be explained as the cells walls bend in response to the stress. The next stage of buckling describes the rapid drop in the average cell size over the strain range of 10 to ~45 percent strain. Once the cell walls have all buckled, densification occurs which has a slower rate of cell size change and is seen at the end of Figure 2.9(a). This is supported by the images in Figure 2.9b, in which the main cells buckle at scans within the range of 20 and 30 percent engineering strain. The cells become difficult to distinguish when the densification started around the 50 percent strain scan.

2.5 Conclusion

1. Epoxy shape memory foams are capable of recovery from compressive strains of up to 90% depending of the prescribed thermo-mechanical cycles.
2. There is both temperature and strain dependence of the strain recovery under monotonic loading. The threshold observed in this work was at 125°C and for strains beyond 80%, after which there is a sharp decrease in strain recoverability under monotonic loading.
3. Compressive cyclic strain can damage the foam under certain temperatures and applied strains. The damage under compression can be greatly minimized by lowering the maximum strain or changing deformation temperature to a temperature where tensile ductility is maximized.
4. The optimum temperature at which to package the material to minimize structural damage is approximately 80°C, below the glass transition temperature measured by the peak of the tan delta curve from thermo-mechanical analysis.

5. The packaging temperature strongly affects the unconstrained shape recovery profile.
6. The micro-CT scans show that the cell structure does deform as predicted in numerical models of foam deformation.

CHAPTER 3: DEFORMATION OF EPOXY SHAPE MEMORY FOAMS: EXPERIMENTS AND CONSTITUTIVE MODELING

3.1 Introduction

Having explored the basic thermomechanics of epoxy SMP foam in Chapter 2, this chapter focuses on how the relative density of the foam affects macroscale response to deformation. Epoxy shape memory foams with relative densities of 20, 30, and 40% and a glass transition temperature (Tg) near 85°C as measured by dynamic mechanical analysis were tested in compression. Micro-CT scans were used to characterize the micro-architecture for each relative density. Tensile test data showed a temperature dependence on the effect of relative density on tensile strain to failure. Compression tests demonstrated similar effects of relative density at different temperatures. Unconstrained shape recovery tests showed no effect of relative density on free strain recovery, while constrained stress recovery showed a strong effect of relative density. Relative density did have a slight effect on constrained cooling, which was demonstrated to be controlled by viscous relaxation followed by thermal stress relaxation. A model from Gibson and Ashby on cellular solids was used to simulate the effect of relative density on the macroscale stress-strain properties. The prediction of the effect of relative density on modulus correlated well with the DMA data, and the compressive response was fit to each compression curve. However, it was necessary to modify the prediction for the densification strain and allowing it to depend on temperature for the fits to correlate with

experimental data at higher strains. The fitting parameters were fairly temperature independent once the material was above Tg.

3.2 Background

The framework used here was proposed by Gibson and Ashby and is based on experimental data as well as modeling of idealized open cell foam elements(Gibson and Ashby, 1997). Equation (3.1) relates the modulus of the foam based on the relative density and the modulus of the fully dense base material; E^* is the modulus of the foam, E_s is the modulus of the base material, ρ^* is the density of the foam, and ρ_s is the density of the base material. The ratio $\rho^*/\ \rho_s$ is the relative density of the foam. Equation (3.2) relates the densification strain of the foam, at which the stress-strain response stiffens due to cell wall contact, to the relative density; Gibson and Ashby introduced the factor of 1.4 as the compressibility modifier (Gibson and Ashby, 1997). The compressibility modifier relates the densification strain to the RD. Nominal stresses and strains are employed in these relations.

$$\frac{E^*}{E_s} \approx \left(\frac{\rho^*}{\rho_s}\right)^2 \tag{3.1}$$

$$\epsilon_D = 1 - 1.4\left(\frac{\rho^*}{\rho_s}\right) \tag{3.2}$$

For elastomeric foams, the compressive behavior is decomposed into linear and non-linear regions. The linear region is defined as according to Equation (3.3); where σ^* is the stress of the foam, ϵ is the strain, and ϵ_{el}^* is the elastic strain limit of the foam (set to 0.05), and D is a fitting parameter. The term σ_{el}^* is the elastic limit of the foam and in

defined in Equation (3.4). The non-linear region is defined via Equation (3.5), where m and D are fitting parameters.

$$\frac{\sigma^*}{\sigma^*_{el}} = 1 \text{ for } \epsilon \leq \epsilon_D \left(1 - \frac{1}{D}\right) + \epsilon^*_{el} \tag{3.3}$$

$$\frac{\sigma^*_{el}}{E_s} \approx \epsilon^*_{el} \left(\frac{\rho^*}{\rho_s}\right)^2 \tag{3.4}$$

$$\frac{\sigma^*}{\sigma^*_{el}} = \frac{1}{D}\left(\frac{\epsilon_D}{\epsilon_D - \epsilon}\right)^m \text{ for } \epsilon > \epsilon_D \left(1 - \frac{1}{D}\right) + \epsilon^*_{el} \tag{3.5}$$

3.3 Experimental

This study focused on an epoxy foam with the trade name TEMBO® DP5.1, provided by Composite Technology Development (CTD). Chemical and processing details of the material are proprietary, but the material can be considered to be a two-part thermoset epoxy network. Three relative densities (20, 30, and 40%) were supplied along with neat resin.

To determine the T_g, a Thermal Analysis Instruments DMA Q800 was used with film tension clamps. The remainder of the tests were performed using an MTS Insight 2 uniaxial mechanical test frame with an attached thermal chamber. A thermocouple was located inside the thermal chamber and was placed adjacent to the sample. A laser extensometer, MTS LX300, was used to measure strain for tensile tests while the crosshead displacement was used for this purpose in compression tests. MTS high load capacity compression platens (643.10A-03) were used to compress the cylindrical foam specimens.

Three types of experiments were performed to measure bulk properties and responses: DMA, tensile, and shape recovery. Two types of shape memory experiments were conducted, namely free strain and constrained stress recovery.

X-ray micro-CT scanning. Two samples of the three relative densities of interest were scanned using a Scanco Medical μCT 40 desktop micro-CT scanner with microfocus X-ray source located within the Georgia Institute of Technology Orthopaedic Bioengineering Laboratory. The cylindrical samples were 15mm in height and 6mm in diameter and were scanned at 12μm voxel resolution. Mesostructure characterization (i.e., cell shape, sizes, and distributions) of the foams was performed using the ScanCo analysis software based on direct distance transformation methods that are independent of model-based assumptions (Hildebrand, et al., 1999).

DMA. Rectangular specimens were cut to dimensions of 5x25x1 mm and inserted in the tensile film clamps. The sample was equilibrated at 25°C for two minutes and then heated to 145°C at a rate of 5°C/min. The test was run under engineering strain control, with a strain of 0.1%, a preload of 0.01 N, a force track (ratio of static load to dynamic load) rating of 150%, and a frequency of 1 Hz. The strain value of 0.1% keeps the material in the linear viscoelastic region

Tensile Tests. Specimens were cut to a half-size ASTM D638 Type IV dogbone with a thickness of 1 mm. The specimens were mechanically loaded using MTS Advantage

Screw Action tensile grips at an engineering strain rate of 0.0025 s^{-1} until failure. After measuring the width and thickness of the gauge length, a piece of laser tape was placed on both ends of the nominal gage section of the dog bone specimen. The nominal gage length, used for calculations of strain, was measured prior to and during testing with the laser extensometer. The use of laser tape did not appear to adversely affect the results, as the specimens failed in the center of the gage region as often as they failed near the laser tape. The specimen was placed in the tensile grips so that the laser tape was facing the thermal chamber door, and the thermal chamber heated to the appropriate temperature. Fully dense polymer specimens were tested at temperatures of 25°C, 40°C, 45°C, 50°C, 55°C, 60°C, 65°C, 70°C, 75°C, 100°C, and 125°C. Foam specimens were tested at temperature of 25°C, 45°C, 50°C, 52°C, 55°C, 57°C, 60°C, 65°C, 70°C, 75°C, 80°C, 85°C, 95°C, 105°C and 125°C. The temperature differences were due to differences in test temperature refinement to find the strain to failure peak. To ensure uniform temperature, specimens were held at each temperature for ten minutes prior to testing. Three specimens were run at each temperature to investigate repeatability.

Compression tests. The tests were conducted at three different temperatures: 25°C, T_g, and Tg + 20 where Tg was determined for each of the foam relative densities. To ensure uniform heating, the thermal chamber and each specimen were held at the experimental temperature for ten minutes prior to commencement of testing. To achieve full contact of the platen on the sample, a preload of 0.2N (25°C) or 0.05N (Tg and Tg + 20) was used. The cross head speed was set at a rate of 3mm/min, corresponding to an engineering

strain rate of 0.0025 s^{-1}. The sample was compressed to a load of 1950 N (25°C) or 95N (Tg and Tg + 20), nearly the maximum load for the respective load cells.

Shape storage. Shape storage is the first step for both constrained stress recovery and free strain recovery. The specimen was heated to 55°C and compressed to a strain of 75%. This compression was maintained as the specimen was cooled in the thermal chamber at 2°C/min to 25°C and the platen was raised after there was no longer a stress registering on the load cell. The deformation temperature of 55°C was used as it corresponds to the temperature with the highest tensile strain-to-failure for DP5.1.

Constrained stress recovery. This experiment measured the stress generated as a function of temperature as the packaged material attempts to recover while constrained. A schematic for this can be found in Figure 3.9(b). The packaged specimens were placed into the MTS Insight 2 mechanical test frame, with a 100N load cell and attached thermal chamber, and compressed at room temperature to a preload of 0.5N. The compression platen was then raised 0.3 mm to take into account thermal expansion. The platen was then held at that position as the temperature was increased from 25°C to 125°C at a rate of 2°C/min. The stress exerted by the specimen on the platen was then recorded versus time, which was correlated to the temperature.

Free strain recovery. This experiment measures strain recovery as a function of temperature as the packaged material recovers in an unconstrained state. A schematic can be found in Figure 3.9(a). A square glass slide, with laser tape along the edge facing the

extensometer, was set on top of the packaged specimen. The specimen was then placed on a single compression platen, also with laser tape on the edge (facing the extensometer and parallel to the glass slide), in the MTS Insight 2 with attached thermal chamber. The specimen was attached to both the platen and the glass slide with a single piece of double-sided tape. The specimen was then heated from 25°C to 125°C at a rate of 2°C/min, while the MTS LX300 laser extensometer recorded the displacement of the two pieces of laser tape. This displacement was used to determine the percent strain recovered and plotted against the temperature (again correlated with time).

3.4 Results

Micro-CT scanning determined the volume fraction to be 19.8%, 30.6%, and 40.2% for the 20%, 30%, and 40% RD foams. The distribution of cell size (pore spacing) and strut thickness in mm of the foams is shown in Figure 3.1.

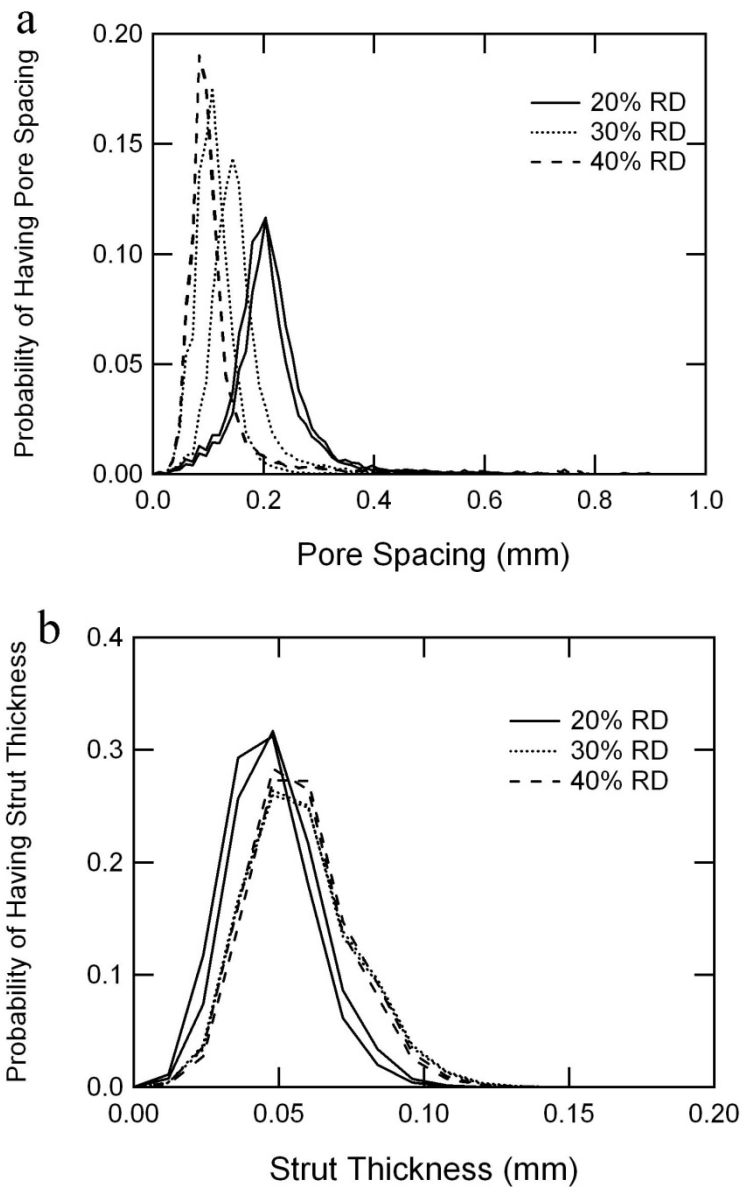

Figure 3.1: Distribution of a) pore spacing and b) strut thickness as determined through micro-CT scanningof DP5.1.
The average pore spacing was 0.21, 0.13, and 0.12 mm for 20% RD, 30% RD, and 40% RD foams respectively. The average strut thickness was 0.047, 0.057, and 0.057 mm for the 20% RD, 30% RD, and 40% RD foams respectively.

The distributions correlate well for the two sets of scans except for the 30% RD pore spacing. The connectivity was measured to be 292, 470, and 800 for the 20%, 30%, and 40% RD foams. Connectivity is a volume normalized measure of redundant connections

among struts based on Euler characteristics and has units of mm^{-3} (Odgaard and Gundersen, 1993) and can be thought of as number of struts normalized to volume. Measurement of strut anisotropy showed that there is no significant directional preference for strut length. This can be visually observed in the representative images from the micro-CT scans, shown in Figure 3.2.

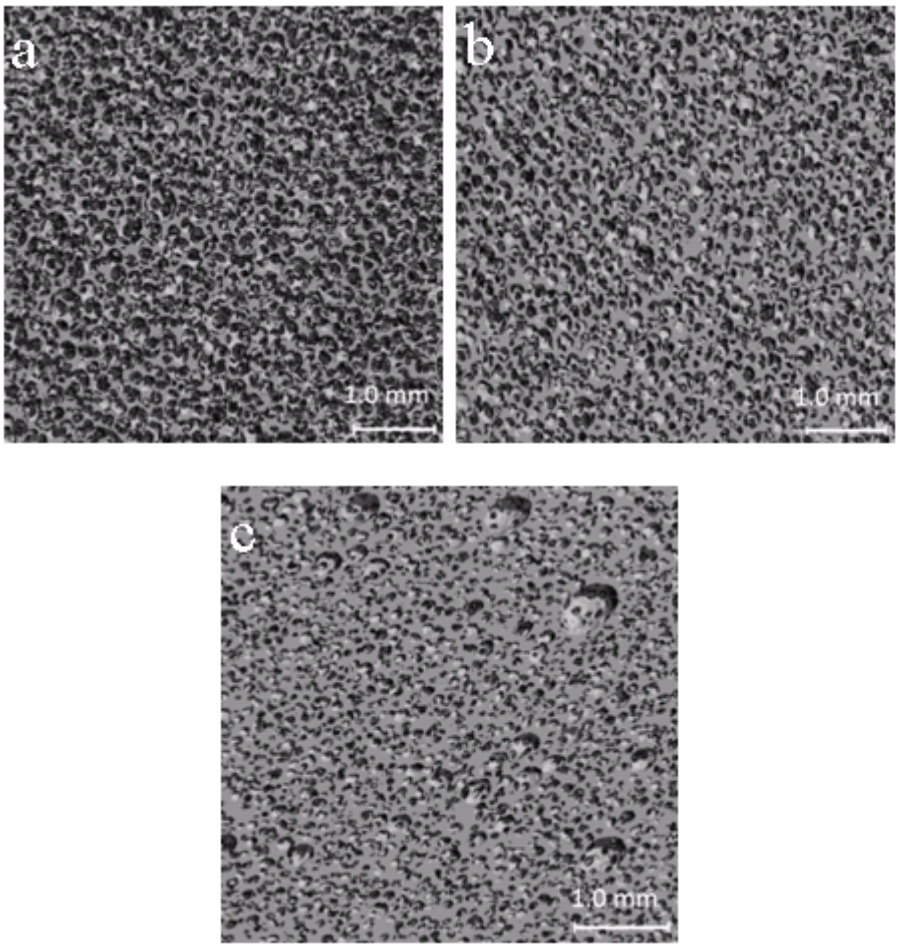

Figure 3.2: Representative micro-CT images of the three different foam relative densities of DP5.1. The scans were taken at a resolution of 12µm to a pixel and 2a) is of the 20% RD sample, 2b) is of the 30% RD sample, and 2c) is of the 40% RD sample.

DMA tests for the resin and the three relative densities (RD) are shown in Figure 3.3 with error bars representing a single standard deviation. The peaks of the tan delta for the resin, 20%, 30%, and 40% RD foams respectively occurred at 84.7 ± 0.6°C, 84.2 ± 0.2°C, 87.9 ± 2.6°C, and 82.7 ± 0.3°C showing negligible effect of RD on T_g. Predictions of Equation (3.1) based on the modulus of the resin from Figure 2 for the foams with relative densities of interest are shown in Figure 3.4.

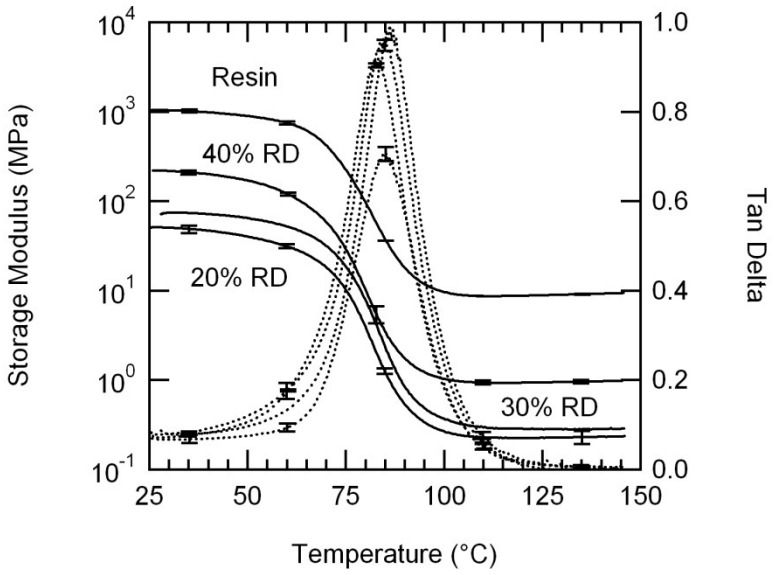

Figure 3.3: The storage modulus and tan delta of the base polymer and the three relative densities as a function of temperature as determined by DMA.
The Tg is defined as the peak in the tan delta and the error bars represent one standard deviation from mean value.

The failure strain for the tensile tests as a function of temperature is shown in Figure 3.5. The maximum tensile failure strain for the resin was 93 ± 2.8% at 55°C and the maximum strain-to-failure for the foam was also 93 ± 2.8% at 55°C. Below this temperature the tensile strain-at-failure of the resin is significantly greater than that of the

foam, while at temperatures above 55°C the difference in tensile failure strain between foam and resin is negligible. This does not correspond to the peak of the loss modulus of the base polymer or the foam (~70°C). However, on the more recent DMA test the loss modulus for the foam peaks at 55°C, see A.7 and A.8 for more on DMA differences.

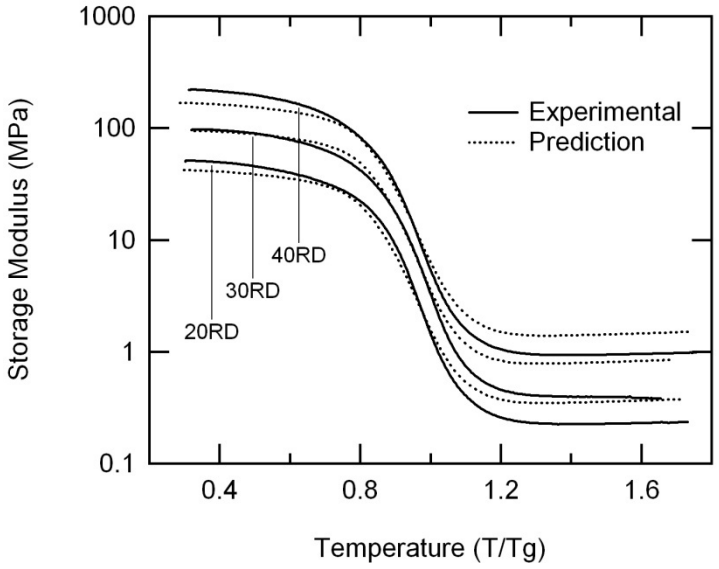

Figure 3.4: : **Comparison of the experimental storage moduli of the three relative densities and the moduli predicted by Equation 3.1.**

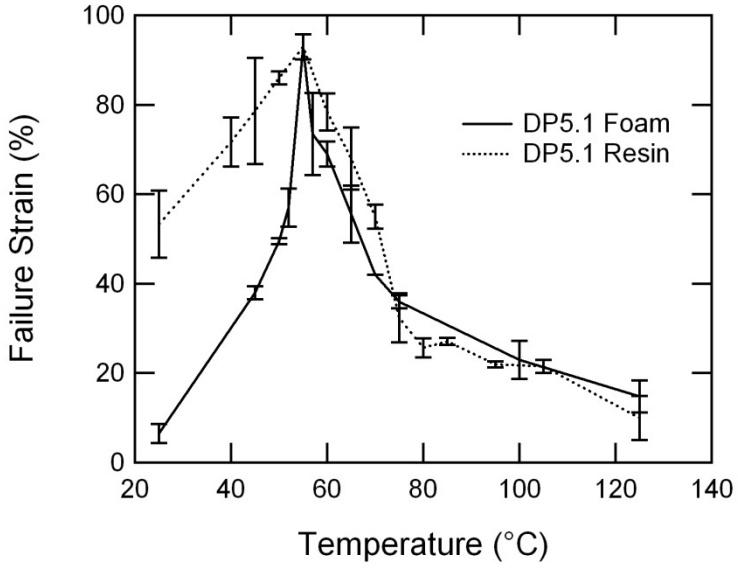

Figure 3.5: Comparison of tensile strain to failure of DP5.1 foam and resin.

The effect of relative density and temperature on compressive behavior is shown in Figure 3.6, with 7(a) at 25°C, 7(b) at Tg, and 7(c) at Tg + 20. These plots show that the compressive response depends both on the temperature and the relative density and the impact of relative density is consistent across the temperatures. Equations (3.3) and (3.5) are overlaid for each curve with the fit parameters found in Table 3.1. Fit parameters were computationally determined to minimize deviance from experimental data using MatLab (1984-2009).

Table 3.1: Fitting Parameters

Relative Density (%)	Temperature	m	D
20	25°C	.45	1
20	Tg	1.6	1.05
20	Tg + 20°C	1	1.05

Relative Density (%)	Temperature	m	D
30	25°C	.26	1
30	Tg	1	1.05
30	Tg + 20°C	1.1	1.09

Relative Density (%)	Temperature	m	D
40	25°C	.31	1
40	Tg	.7	1.3
40	Tg + 20°C	2	1.055

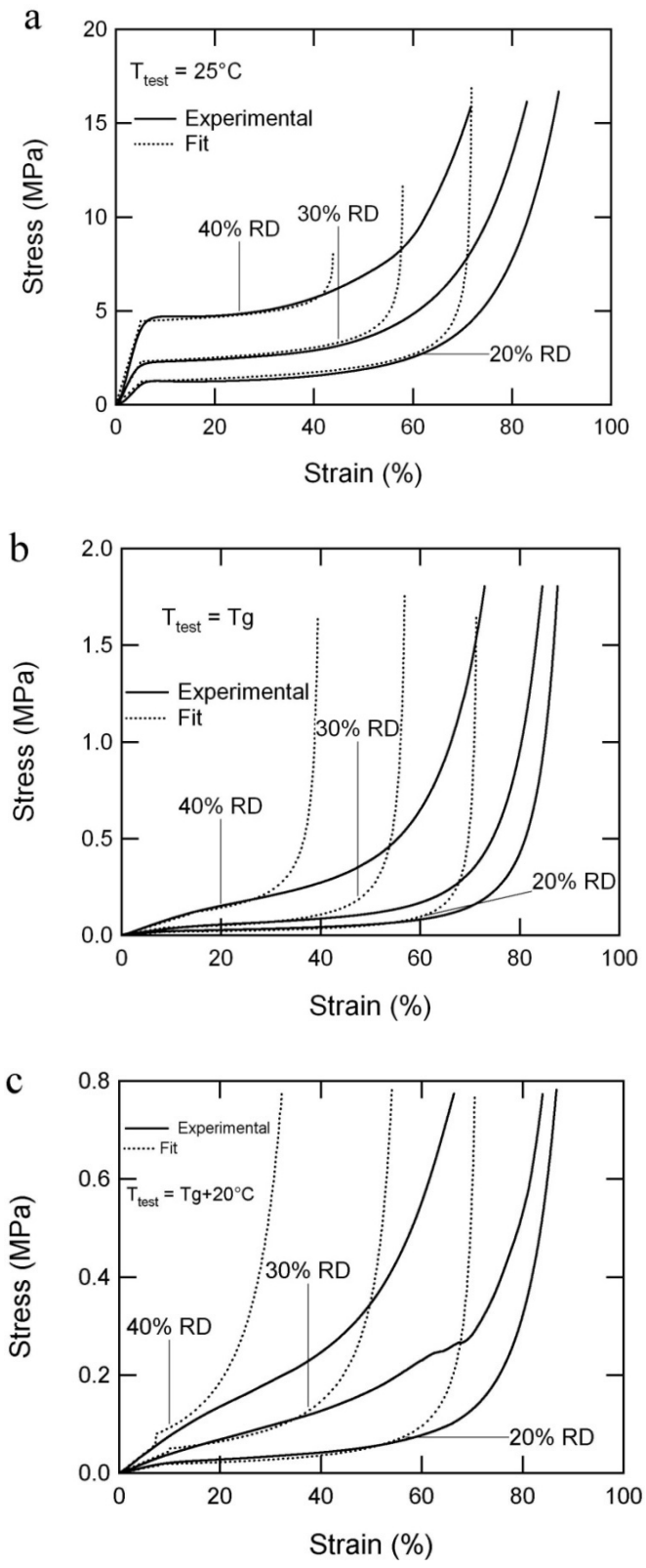

Figure 3.6: Compressive response of the three different relative densities at three different temperatures.
6a) is at 25°C, 6b) is at Tg, and 6c) is at Tg+20°C.

Figure 3.7 shows the Gibson-Ashby fit for the foam, (Equations (3.3) and (3.5), see Table 3.2 for fitting parameters) with a temperature dependent compression modifier. From Equation 3.2, the densification strain is solely dependent on relative density, but Figure 3.7(a) shows strong temperature dependence of the densification strain of these materials; so 0.66, 0.25, and 0.14 for the appropriate temperature were used instead of 1.4 for the compressibility modifier. Each point represents the densification strain of 3 samples at the indicated temperature and the error bar represents the range of the values. Figures 3.7(b)-(d) shows the fit with the parameters in Table 3.2, and the compressibility modifier from Figure 3.6(a) reasonably predicts the compressive response.

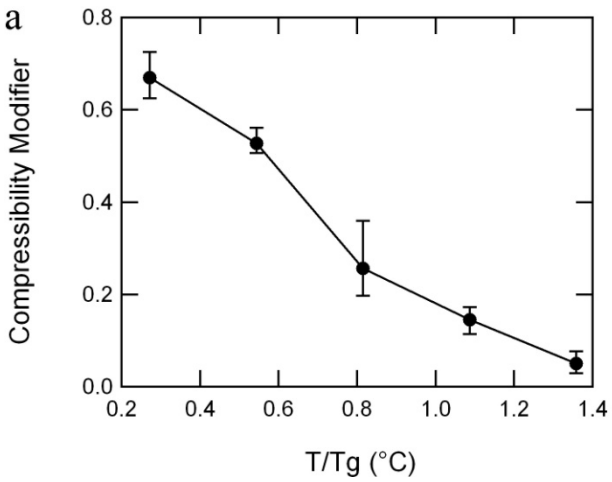

Figure 3.7: Fitting of the compressive response using Equations 3.4 and 3.6. 3.7a) illustrates the effect of temperature on the compressibility of the foam, 3.7b) has the fit overlaid with the experimental response at 25°C, 3.7c) has the fit overlaid with the experimental response at Tg, and 3.7d) has the fit overlaid with the experimental response at Tg+20°C.

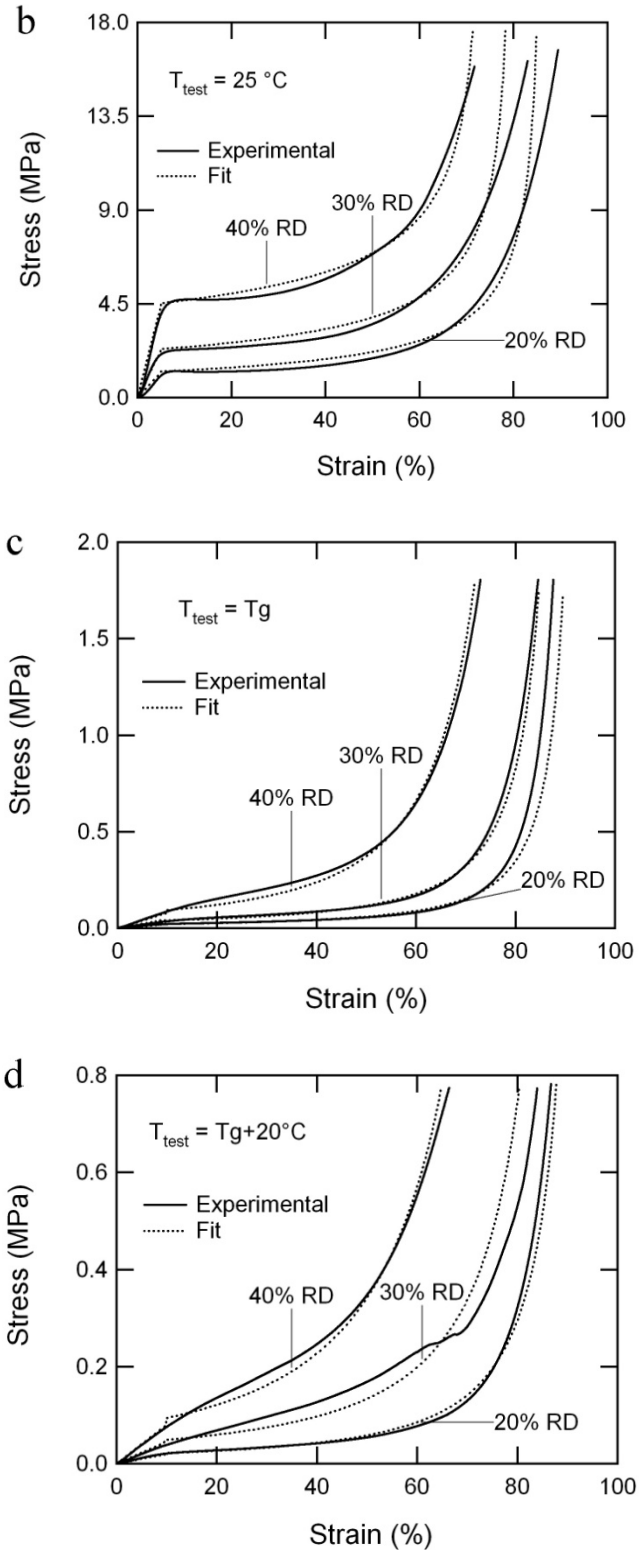

Figure 3.7 continued

Table 3.2: Adjusted Fitting Parameters

Relative Density (%)	Temperature	m	D	Compressibility Modifier
20	25°C	0.7	1	0.66
20	Tg	1.6	1.05	0.25
20	Tg + 20°C	1.6	1.05	0.14

Relative Density (%)	Temperature	m	D	Compressibility Modifier
30	25°C	0.55	1	0.66
30	Tg	1.6	1.03	0.25
30	Tg + 20°C	1.6	1.05	0.14

Relative Density (%)	Temperature	m	D	Compressibility Modifier
40	25°C	0.4	1	0.66
40	Tg	2	1.055	0.25
40	Tg + 20°C	2	1.055	0.14

The average constrained cooling response of the foams is presented in Figure 3.8, with error bars representing a single standard deviation from the mean. Figure 3.8(a) includes an overlay of the experimental isothermal relaxation response for foams with each of the three relative densities at the deformation temperature. Figure 3.8(b) includes an overlay of the calculated linear thermal stress relaxation, $\sigma_t = E\alpha\Delta T$, where E was determined by the modulus results in Figure 3.3 and α was fit to the linear region of Figure 3.8(a) (strain as a function of temperature). This linear model was chosen for simplicity and is used as a comparative tool for the constrained cooling mechanism. The placement of the line was determined by where it intersected the cooling curve while being parallel.

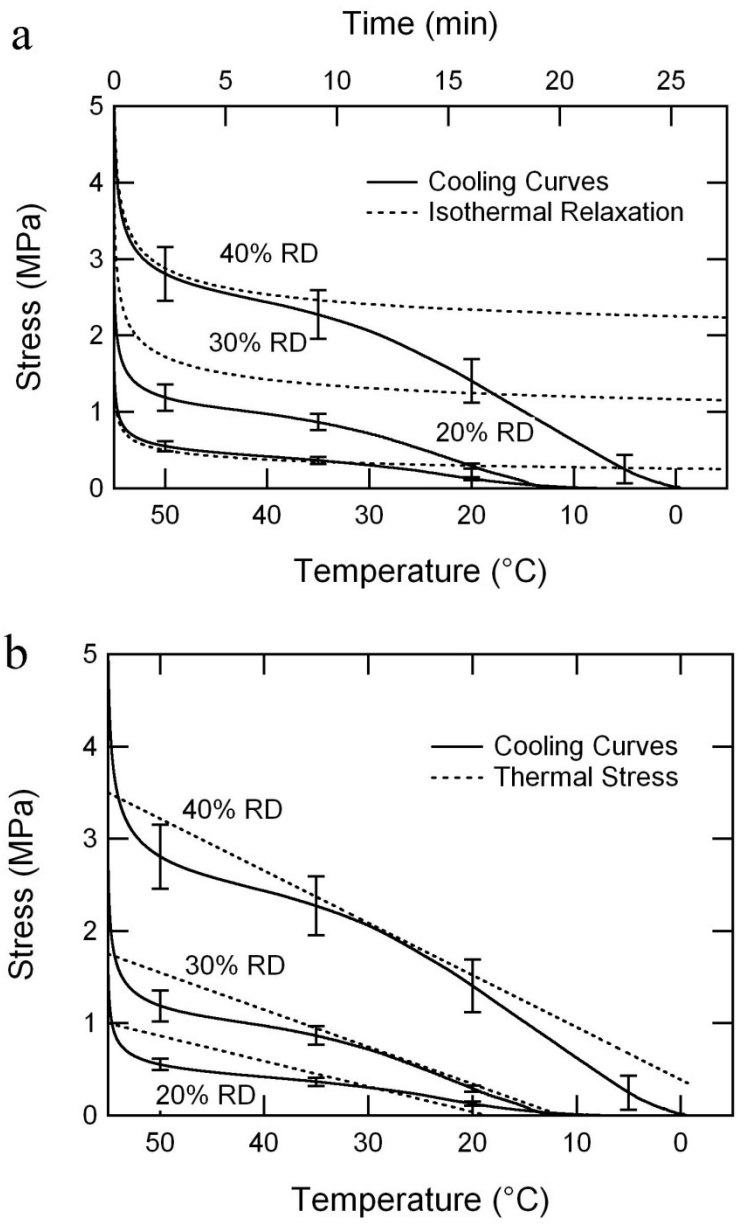

Figure 3.8: Constrained cooling response during shape packaging of the three different densities. 3.8a) has the isothermal relaxation behavior at the packaging temperature overlaid for the different relative densities and 3.8b) has the calculated thermal stress relaxation overlaid for the different relative densities. This shows the behavior mechanisms of the constrained cooling (packaging) step for these materials.

The effect of relative density on shape recoverability is shown in Figure 3.9; including both 3.9(a) free strain recovery and 9(b) constrained stress recovery. Figure 3.9(a) shows

no significant effect of relative density on free strain recovery. Figure 3.9(b) shows a significant effect of relative density on constrained recovery; at the higher densities failure occurred at high temperatures during constrained stress recovery.

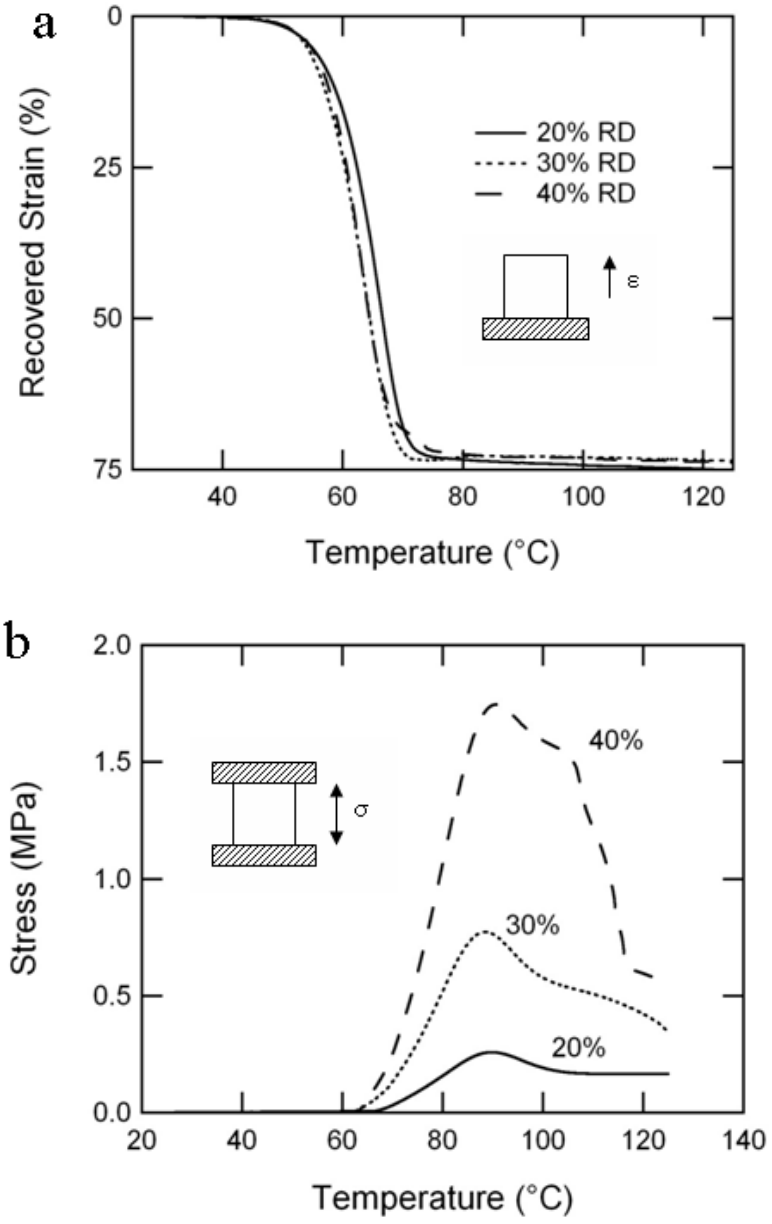

Figure 3.9: Shape recovery response for the three different relative densities
10a) is the free strain recovery response, the recovered strain as a function of temperature, of the three foams and 10b) is the constrained stress recovery, constrained stress as a function of temperature, for the three materials.

3.5 Discussion

While foaming SMP gives it the high compressibility and low density attractive for so many applications, it also reduces other thermomechanical properties. This trade-off is critical to understand the fundamental behavior of SMP foams as well as for optimization for specific applications. Micro-CT scanning revealed that the structural parameters of the investigated foams did not scale with relative density. The elastic modulus of the investigated foams scaled in a predictive manner with an acceptable variance with relative density. The fitting of the stress-strain behavior used the relative density dependence on elastic modulus as well as a relative density term in the densification strain. Constrained cooling behavior, depending on elastic modulus, trended with relative density. Free strain recovery behavior was uniformly independent of structure across the investigated relative densities, while constrained stress recovery had a strong dependence on relative density. Material responses with elastic modulus dependence (elastic modulus, compression response, cooling curves, and constrained stress recovery) scaled with increasing relative density while the material responses that were independent of elastic modulus (T_g, free strain recovery) were independent of relative density. This advances the understanding of SMP foam behavior and allows for better optimization for specific applications.

The measured volume fraction for the foams is close to predicted relative density, however as the micro-CT scan had a 12μm resolution the measured volume fraction will inherently be low as features less than 12 μm will not be counted. There is a significant change in average strut thickness and pore spacing between the 20% and 30% RD

samples and less of a difference in these parameters between 30% and 40% RD. The difference in the strut thickness is apparent in the probability distribution, Figure 3.1b, as the 30 and 40% RD distributions are nearly identical while the 20% RD is shifted slightly towards smaller struts and has a narrower peak. The connectivity scales reasonably well with the RD, which can be visually observed in Figure 3.2 as there appears to be more struts and smaller pores as relative density increases. This is significant, as the use of only porosity (relative density) as a single state variable to reflect microstructure fails to capture the full complexity of the material, as seen in both Figures 3.1 and 3.2 . This result also emphasizes the need for direct simulation of these different mesostructures to understand how the changes in strut thickness and pore spacing affect the local deformation mechanics that may significantly affect foam densification and degradation, for example.

Since T_g in cross-linked polymers is a function of polymer chemistry and network organization, it is expected that the relative density would not have a significant effect on the T_g, as shown in Figure 3.3. The result in Figure 3.3 confirms this and allows for the T_g to be tailored independent of the microstructure. In prior work (M. A. Di Prima, et al., 2007) we showed a change in T_g with foaming, but this prior processing route resulted in some residuals that either plasticized the foam or altered the foam chemistry in a manner to lower cross-link density and/or T_g. While the elastic stiffness of the foams depends on the relative density, as shown in Figure 3.3, the dependence closely follows the prediction of the open cell model of Gibson and Ashby in Equation (3.2), shown in Figure 3.4, based on the modulus-temperature data from the solid polymer material. This allows the

relative density to be tailored to a desired elastic stiffness of the foam at a given temperature once the base polymer has been characterized.

The tensile results from Figure 3.5 reveal two important behaviors. The first is that the maximum strain attainable by these systems is not dependent on initial relative density for the range considered (20 to 100% RD). Not only does this allow for simplified material characterization but also it allows for the relative density to be tailored to other properties without sacrificing tensile failure strain within the limits of the materials structures. The second key behavior is that microstructure/relative density dominates the tensile failure properties in the glassy region and is then negligible in the viscoelastic and rubbery regions. Clearly, in the glassy state, the material is more flaw sensitive and the local stress concentrations drive failure at lower applied strain levels.

The results of Figure 3.6 follow the expected trend of both relative density and temperature and show that the compressibility modifier of 1.4 is too large for the investigated foams. Figure 3.7(a) is of interest because it shows that the densification strain is a function of temperature, something not addressed by Gibson and Ashby modeling. Furthermore, these foams have better compressibility than predicted by the model of Gibson and Ashby in Equation 3.2, as they determined a compressibility modifier of 3.4, which is significantly larger than the 0.66 for the SMP foam at room temperature. With this correction, the Gibson-Ashby fit, Equations 3.3 and 3.5, correlate well with the experimental data over the full strain range. The fitting parameters from Table 3.2 show a strong parameter dependence (m) on the relative density at low

temperatures, but little dependence at elevated temperatures. Significantly, the parameters change little between Tg and Tg + 20°C within a specific relative density, which means that the compressive behavior at elevated temperature is predominately controlled by the changing modulus of the base polymer.

During the cooling after compression, the stress in the foam material decreases non-monotonically with decreasing temperatures and ultimately reaches zero. The constrained cooling plots, Figure 3.8, show that a stress build up in the "packaging process" (shape storage) is reduced due to viscous relaxation. This is most likely due to thermal lag in the polymer material due to the low conductivity of the polymer, the spatial lag in the thermal chamber temperature and the slow cooling rate, which maintains each individual temperature longer. The cooling rate was selected to be the same as the heating rate in the shape recovery tests and was minimized to manage spatial thermal gradients in the oven and material. Nevertheless, there will always be some lag in the packaging process and it is important to know that the material will undergo significant relaxation. The calculated thermal stress relaxation curves indicate that most of the non-viscous relaxation can be attributed to thermal stress relaxation driven by thermal contraction of the compressed material (this same effect drives an increase in tensile stress in samples held after tensile stretch (Y. Liu, 2006)). The deviation of the calculated thermal stress relaxation from the experimental data, shown in Figure 3.8(b), can be ascribed to the complexity of determining the coefficient of thermal expansion of stored SMP foam, as it needs to be separated from general temperature induced recovery strain and is dependent on densification (applied strain). Further deviation could be the result of non-uniform

cooling rate of the sample, a variable modulus, or non-linear thermal stress behavior. The initial temperature is low enough, ~Tg -30°C (55°C) , that the effect of constrained stress recovery forces should be negligible, as shown in Figure 3.9(b). Even with the deviation, the constrained stress cooling response of the foams at this temperature is dominated by viscous stress relaxation and the decay of thermal stress.

The lack of dependence of free strain recovery on relative density further increases the tailorability of the material since relative density can be tuned within the limits considered here without diminishing overall free strain recoverability. However, this trend is not continued in constrained stress recovery (Figure 3.9(b)) where elastic properties also control response during in recovery responses. Furthermore, the recovery induced failure of the 30% and 40% RD materials indicates that there is a limit of force that these materials can generate. The failure was most likely due to local (mesostructural) strains exceeding the strain to failure of the material as the material attempts to recover. This can occur even with the recovery stress plateauing as the strain to failure drops as temperature increases. The recovery failure envelope is likely to depend on both packaging strain and temperature, but future work will need to address this aspect.

3.6 Conclusions

1. Relative density has little influence on the Tg in the present foams.
2. Relative density has the predicted effect on modulus as a function of temperature as predicted by Gibson and Ashby for open cell foams.

3. Relative density has the predicted effect on stress/strain response as developed by Gibson and Ashby for open cell foams with a modification for densification strain as a function of temperature.
4. Stresses during compressive packaging decreases through a combination of viscoelastic relaxation and thermal stress (contraction) relaxation.
5. Within the ranges considered here, relative density has minimal effect on the free strain recovery, but has a large effect on constrained stress recovery.

CHAPTER 4: DEFORMATION OF EPOXY SHAPE MEMORY FOAMS: MESOSCALE MODELING AND DEFORMATION

4.1 Introduction

The previous chapter discussed the importance of relative density on the macro-scale response to deformation and the shape storage process. To better understand how this occurs, this chapter focuses on how the relative density of epoxy shape memory polymer foam affects mesostructural response to deformation. The modeled foams had relative densities of 20, 30, and 40%, with a glass transition temperature (T_g) near 85°C as measured by dynamic mechanical analysis. Statistical analysis of the dynamic mechanical analyisis data (3 tests per sample, 4 samples per RD) showed that stiffness did not significantly vary across foam samples of the same relative density. The stress-strain response of the base polymer was obtained through tensile and compressive tests at T_g + 17°C and fit to a hyperelastic material model using the ABAQUS material evaluation function. Meshes for the three relative densities were obtained through micro-CT scanning of actual foams, to accurately represent the mesostructure. Overall compression responses predicted by ABAQUS correlated well with experimental stress-strain results. The simulations qualitatively showed a shift in mesostructure response to deformation between the 20% relative dense material and the materials with higher relative densities. Quantitatively, both the local maximum shear strain and tensile strain cumulative probability distributions within the material were analyzed and a lognormal function was fit to these distributions. The function had three parameters fit to the distribution; two other parameters, the applied macroscale strain and the reference strain

value, were considered in scaling the distributions. These lognormal distributions were then used to predict local strain distributions at applied compressive strain values larger than those simulated in the finite element modeling. The results are discussed in the light of the potential local damage mechanisms in shape memory polymer foams.

4.2 Experiments

The epoxy foam in this work has the trade name TEMBO® DP5.1 Foam and the fully dense base polymer were provided by Composite Technology Development (CTD). Chemical and processing details of the material are proprietary, but the material is a two-part thermoset epoxy network. Three relative densities (20, 30, and 40%) were supplied along with the base polymer.

To determine T_g, a Thermal Analysis Instruments DMA Q800 was used with film tension clamps. The tensile tests were performed using a MTS Insight 2 uniaxial mechanical test frame with an attached thermal chamber. A thermocouple was located inside the thermal chamber and was placed adjacent to the sample. A laser extensometer, MTS LX300, was used to measure strain for tensile tests while the crosshead displacement was used for this purpose in compression tests. The compression tests on the base polymer were performed using an Instron 5580 with attached thermal chamber similar to the one used for tensile testing, while compression tests on the foam were performed with the Insight 2.

Three types of experiments were performed to measure bulk properties and responses to support and evaluate the modeling: DMA, tensile tests, and compression tests.

Simulations were performed with ABAQUS 6.7-1 on the Georgia Tech Titan Cluster**.** In all cases, foam specimen level strains are reported in the form of engineering or nominal strain.

DMA. Rectangular specimens were cut to dimensions of 5x25x1 mm, inserted in the tensile film clamps, and torque was applied to secure them. The sample was equilibrated at 20°C for two minutes and then heated to 150°C at a rate of 5°C/min. The test was run under engineering strain control, with a strain of 0.2%, a preload of 0.01 N, a force track rating (ratio of static to dynamic load) of 150%, and a frequency of 1 Hz. To evaluate the difference in response between samples of similar relative density, four samples at each relative density were randomly selected and three specimens were cut from each sample. Statistical analysis of DMA data was performed using Igor Pro 5.04A (2005) built-in one-way ANOVA analysis tool with the Tukey HSD option for pair wise comparison. For pair wise analysis, a p-value below 0.05 was deemed a significant difference between samples.

Tensile Tests. Specimens were cut to a half scaled ASTM D638 Type IV dogbone with a thickness of 1 mm. The specimens were mechanically loaded using MTS Advantage Screw Action tensile grips with an engineering strain rate of 0.0025 s^{-1} until failure. After measuring the width and thickness of the gauge length, a piece of laser tape was placed on both ends of the nominal gage section of the dog bone. The nominal gage length, for strain, was measured prior to and during testing with the laser extensometer. The use of laser tape did not appear to adversely affect the results, as the specimens failed in the

center of the gage region as often as they failed near the laser tape. The specimen was placed in the tensile grips so that the laser tape was facing the thermal chamber door, and the thermal chamber heated to the appropriate temperature. Base polymer specimens were tested at temperatures of T_g + 17 °C or 102°C. To ensure uniform temperature, specimens were held at each temperature for ten minutes prior to testing. Three specimens were run at each temperature to investigate the repeatability.

Compression tests. Base polymer specimens were machined to cylinders with a diameter of 15 mm and a height of 20 mm. The tests were conducted at T_g + 17 °C or 102°C. To ensure uniform temperature, the thermal chamber and each specimen were held at temperature for ten minutes prior to testing. To achieve full contact of the platen on the sample, a preload of 1 N was used. The cross head speed was set at a rate of 3mm/min to achieve an engineering strain rate of 0.0025 s^{-1}. The sample was then compressed until it exhibited macroscopic failure. Foam specimens were compressed under nearly identical conditions, except the preload was 0.05 N and the compression endpoint was set to 95N, nearly the maximum load for the 100 N load cell.

4.3 Simulation

Finite Element Method (FEM). The uniaxial compression simulation consisted of an assembly of; an upper platen, the foam, and a lower platen. The mesh for the foam was generated for each of the relative densities using input from micro-CT scan characterization to provide an accurate 3D representation of each the three microstructures. The resolution of 12μm/voxel was selected to balance scan time,

computation time, and accuracy of the mesostructure. However, this resolution was unable to properly represent cell walls due to coarse voxellation in converting a digital image into the mesh. The coarseness of the voxellation could also introduce error in the stresses of the individual struts (Guldberg, et al., 1998). Checking the convergence of the simulation to experimental` results will validate the use of this resolution. The meshes were voxellated cubic elements with 75 nodes per side (0.9 mm), with the total number of nodes varying with relative density (roughly 85,000, 127,000, and 170,000), as seen in Figure 4.1.

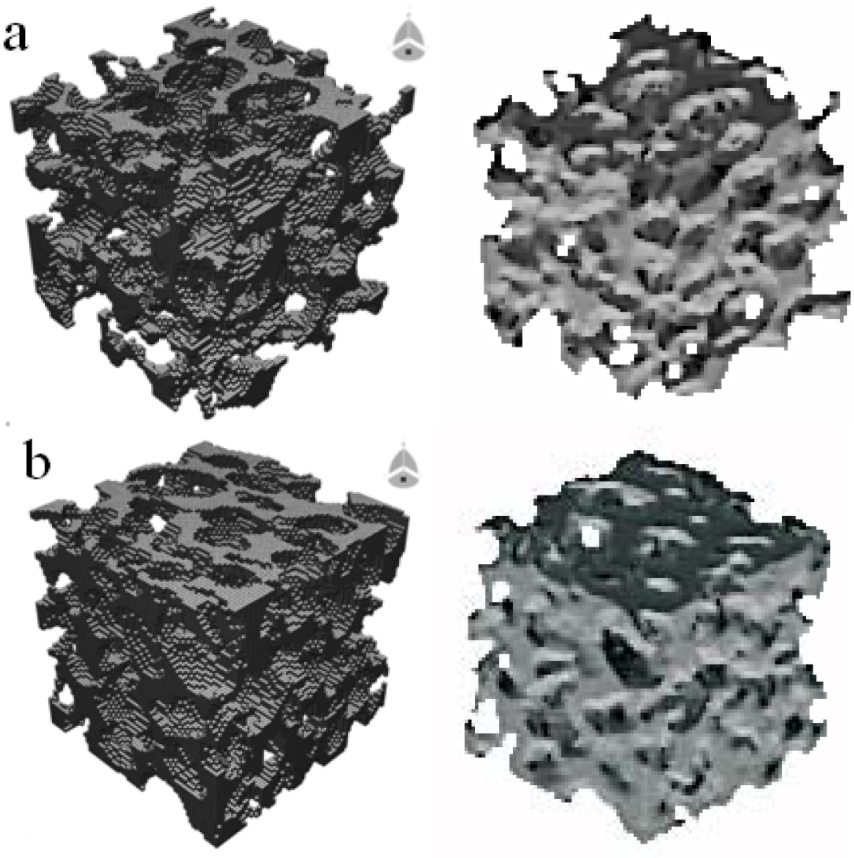

Figure 4.1: FE meshes generated via CT scanning for ABAQUS simulation.

1a) is the mesh for the 20% RD material, 1b) is the mesh for the 30% RD material, and 1c) is the mesh for the 40% RD material. The actual CT scan for each volume is also shown for comparison purposes.

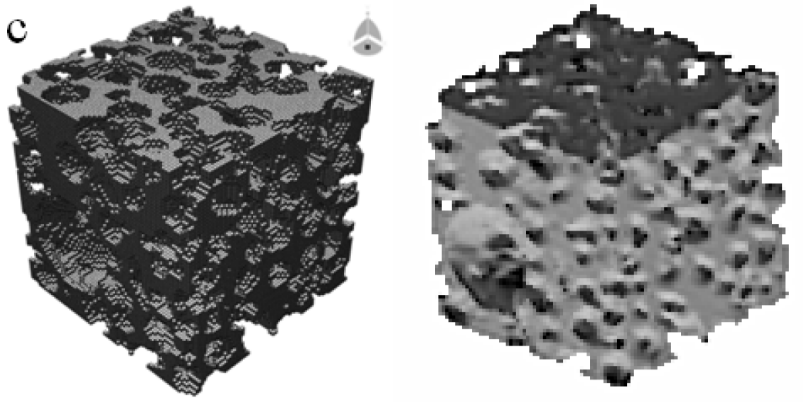

Figure 4.1 continued

The elements connecting the nodes were assigned to be standard type and a linear geometric order. Two meshes were made for each relative density, randomly selected from larger scanned volumes from two different samples, to check convergence of results and to ensure that a RVE was being modeled (in terms of overall foam statistics). Using experimental data from the base polymer and the ABAQUS material evaluation code, a hyperelastic material constitutive law was fit and the appropriate coefficients calculated (Simulia, 2007). The hyperelastic strain energy potential had the form of (2.1) (2007).

$$U = \sum_{i+j=1}^{N} C_{ij}\left(\bar{I}_1 - 3\right)^i \left(\bar{I}_2 - 3\right)^j + \sum_{i=1}^{N} \frac{1}{D_i}\left(J^{el} - 1\right)^{2i} \tag{4.1}$$

Here, U is the strain energy function, I_1 is the first deviatoric strain invariant, I_2 is the second deviatoric strain invariant, C_{ij} and D_i are temperature dependent material parameters, i and j are indices for each parameter, N is the number of indices for each parameter, and J^{el} is the elastic volume ratio defined as the ratio of the total volume to the thermal volume. Using the parameters found in Table 4.1, this material function was assigned to the elements of the foam mesh.

Table 4.1: Hyperelastic Material Fit Parameters

D1	1.30×10^{-7}	C10	1.28×10^{6}
C01	3.70×10^{5}	C11	1.18×10^{7}
C20	-4.97×10^{6}	C02	-5.18×10^{6}

To model the effect of platens (upper and lower platens being identical), a mesh was generated as a rectangular prism that was the same cross-section as the foam mesh and 1/10 the thickness. The platen was composed of 228 nodes connected by standard 3D quadratic brick elements. To make the platens effectively incompressible in comparison to the foam, the platen elements were assigned an elastic modulus of 10 GPa and remained elastic. To connect the foam mesh to the platen mesh, the nodes on the interface were tied to each other, with the platen acting as the master surface and corresponding nodes on contacting foam surfaces as the slave nodes. The lower platen was fully constrained while the upper platen was constrained from movement in the y and z directions. The upper platen was then displaced 0.5 mm toward the foam mesh. The simulation started with an increment step (fraction of total displacement to check for equilibrium) of 0.1 and ran until the step size dropped below 10^{-6}. The actual increment size was optimized by ABAQUS and varied with strain and mesh and averaged 1.2×10^{-2}.

*Lognormal Distribution Fit***:** The strain data were fit using an equation with the form of a lognormal cumulative probability distribution with three fit parameters and two independent variables, i.e.,

$$f(\varepsilon_x, \varepsilon_{app}) = 1 - \left(1 - Ae^{-B \times log\left(\frac{C\varepsilon_x}{\varepsilon_{app}}\right)}\right)^{-1} \quad (4.2)$$

Here A, B, and C are the fitting parameters and $f(\varepsilon_x, \varepsilon_{app})$ is the probability that the local strain is greater than or equal to ε_x, ε_x is a comparison strain, and ε_{app} is the applied (average) strain.

4.4 Results

The dynamic mechanical response as a function of temperature for the various foams are compared in Figure 4.2 and detailed statistical analysis found in Table 4.2; for convenience, only the glassy stiffness (at 20°C), rubbery stiffness (at 150°C), and the T_g are analyzed. For each parameter, the average and standard deviation for each of the four samples is given with the batch average and standard deviation. The p-value for the entire batch, indicating batch uniformity, is also listed. The average for all glassy stiffness's was 150 MPa with a standard deviation of 76 MPa and a p-value $<10^{-3}$. For the rubbery modulus, the overall average was 0.78 MPa with a standard deviation of 0.48 MPa and a p-value $<10^{-3}$. For the T_g, the overall average was 67°C with a standard deviation of 3.73°C and a p-value $<10^{-3}$. The discrepancy between these T_g values and those previously observed (85°C) has been investigated but cannot be adequately explained.

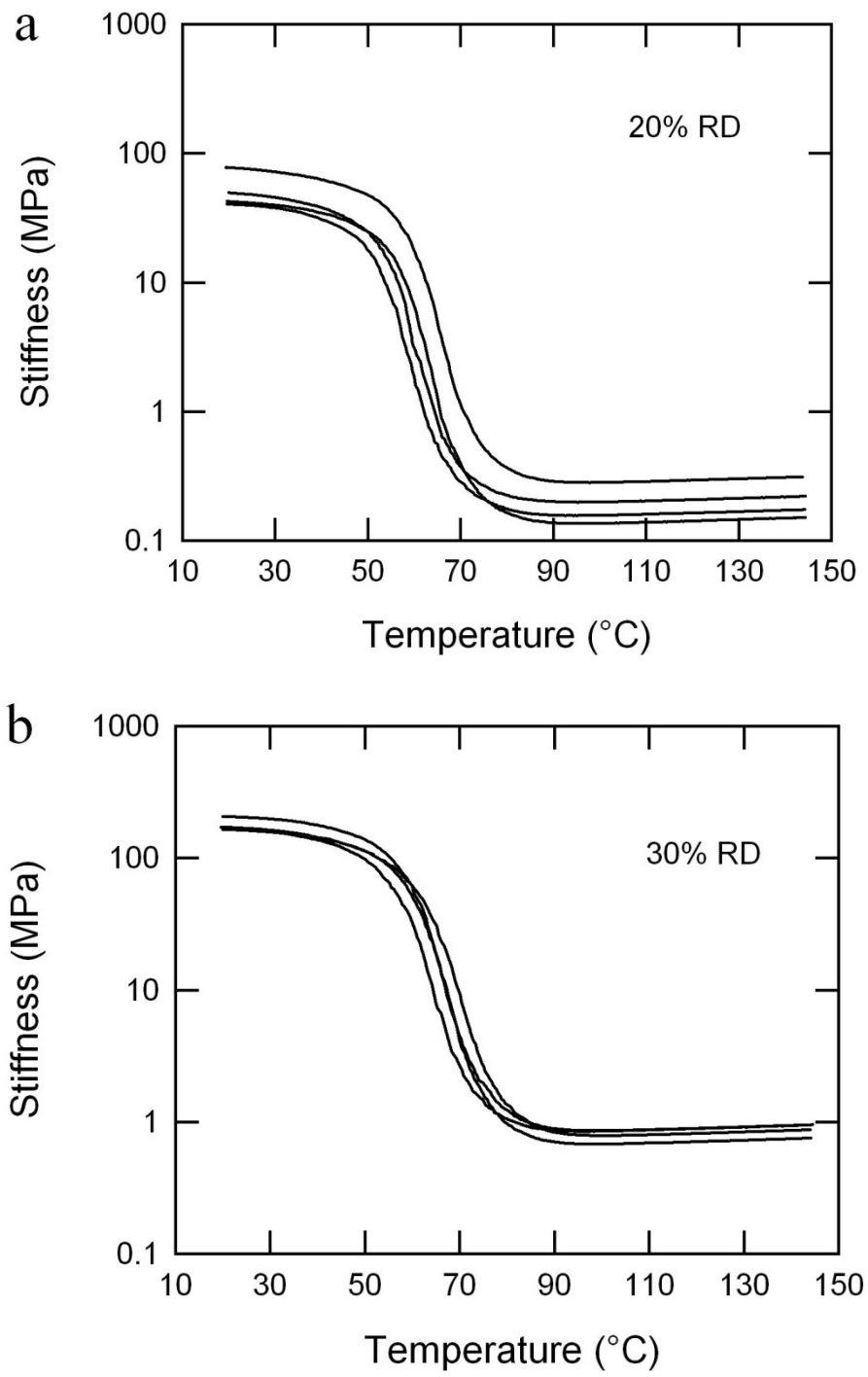

Figure 4.2: DMA results of DP5.1 sample and batch consistency.
Key parameters were: 2a) glassy stiffness, 2b) rubbery stiffness, and 2c) Tg. Three tests were run for four samples from the three relative densities.

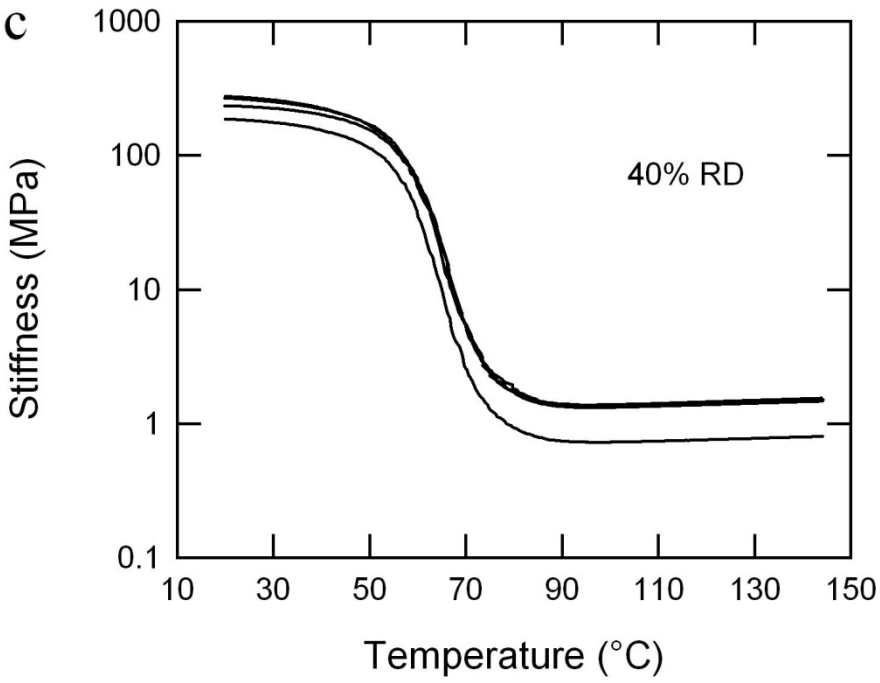

Figure 4.2 continued

Table 4.2: DMA results for sample and batch repeatability

Eg (Mpa)					
20% RD					
	sample 1	sample 2	sample 3	sample 4	batch
average	72.07	57.37	42.23	53.08	56.44
deviation	5.04	16.7	4.02	3.64	11.98
p-value					0.0281
30% RD					
	sample 1	sample 2	sample 3	sample 4	batch
average	172.1	160.5	158.2	177.6	167.1
deviation	26	10.6	15.3	26.9	9.273
p-value					0.646
40% RD					
	sample 1	sample 2	sample 3	sample 4	batch
average	246.2	252.2	242.4	170.1	227.7
deviation	14.9	24.2	28.7	14.5	38.61
p-value					0.005

Er (Mpa)					
20% RD					
	sample 1	sample 2	sample 3	sample 4	batch
average	0.2405	0.2085	0.1783	0.236	0.2158
deviation	0.145	0.06	0.015	0.013	0.0287
p-value					0.772
30% RD					
	sample 1	sample 2	sample 3	sample 4	batch
average	0.972	0.873	0.795	0.8118	0.863
deviation	0.097	0.101	0.041	0.041	0.0799
p-value					0.18
40% RD					
	sample 1	sample 2	sample 3	sample 4	batch
average	1.43	1.46	1.45	0.75	1.273
deviation	0.131	0.073	0.084	0.041	0.348
p-value					<10-3

Tg (C)					
20% RD					
	sample 1	sample 2	sample 3	sample 4	batch
average	65.86	66.08	63.50	61.13	64.14
deviation	1.74	0.37	1.75	1.74	2.47
p-value					0.03
30% RD					
	sample 1	sample 2	sample 3	sample 4	batch
average	75.25	67.15	68.27	67.81	69.62
deviation	6.19	1.54	1.86	1.10	4.46
p-value					0.65
40% RD					
	sample 1	sample 2	sample 3	sample 4	batch
average	66.74	67.43	67.27	65.87	66.83
deviation	1.64	0.92	1.12	1.80	1.36
p-value					0.005

The peak stress for compression (up to 40%) and tension (up to 30%) as a function of engineering strain of the DP5.1 Resin at T_g + 17°C, 102°C, is shown in Figure 4.3. The hyperelastic material fit (coefficients in Table 4.1) is superimposed over the experimental stress-strain response.

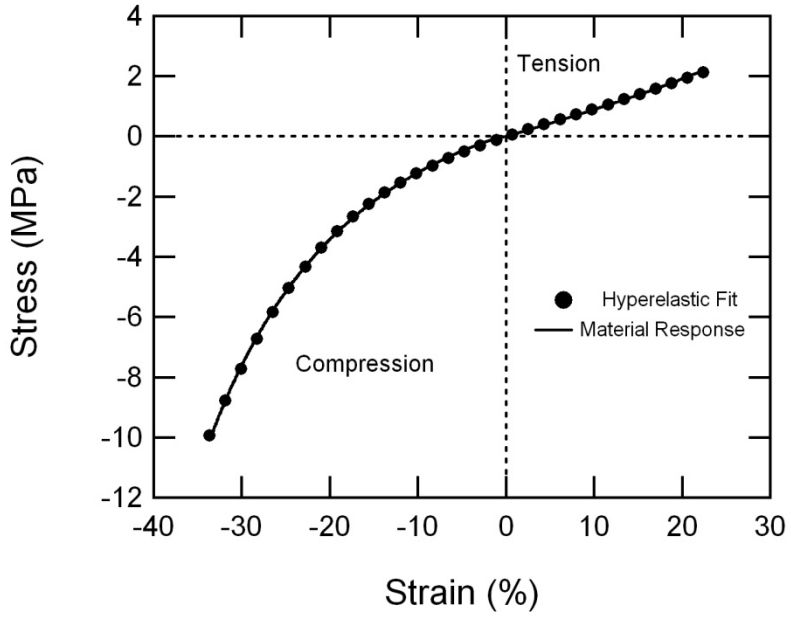

Figure 4.3: Response of the DP5.1 base polymer in compression and tension at T_g + 17°C, or 102°C. The hyperelastic material response fit to the curve via ABAQUS is overlaid for comparison.

The compression predictions from the simulations of the foams using the constitutive model in Figure 4.3 are shown in Figure 4.4, with experimental results from foams of the same relative densities provided for comparison. The two simulation curves for each relative density represent the two different FE mesh instantiations that were generated for each relative density. Representative images highlighting local deformation differences in the foams with different densities are shown in Figure 4.5.

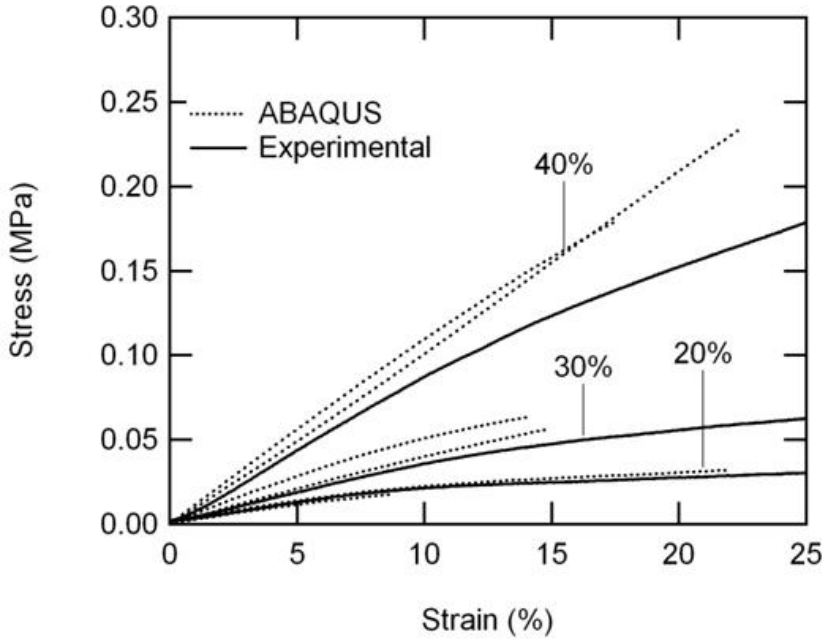

Figure 4.4: Stress/strain response from ABAQUS simulations of the three relative densities. The three relative densities were 20, 30, and 40%. The two curves for the simulations represent the two meshes run for each relative density. The experimentally determined stress/strain response is overlaid to show how the simulation compares to experimental results.

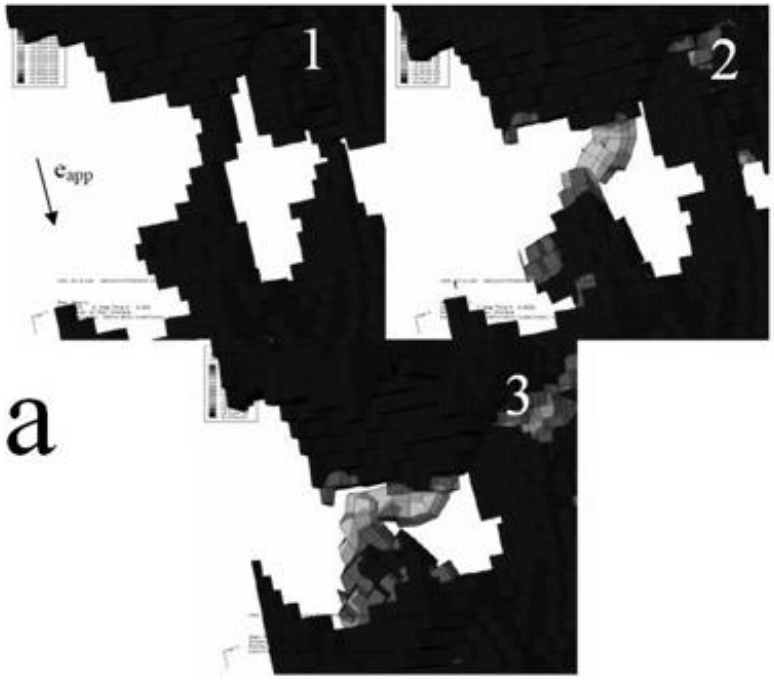

Figure 4.5: Representative local deformation behavior from macroscopic compression. 4a) the 20% RD material deforms primarily in the vertical struts while 4b) and 4C) the 30 and 40% RD materials deform primarily in the joints.

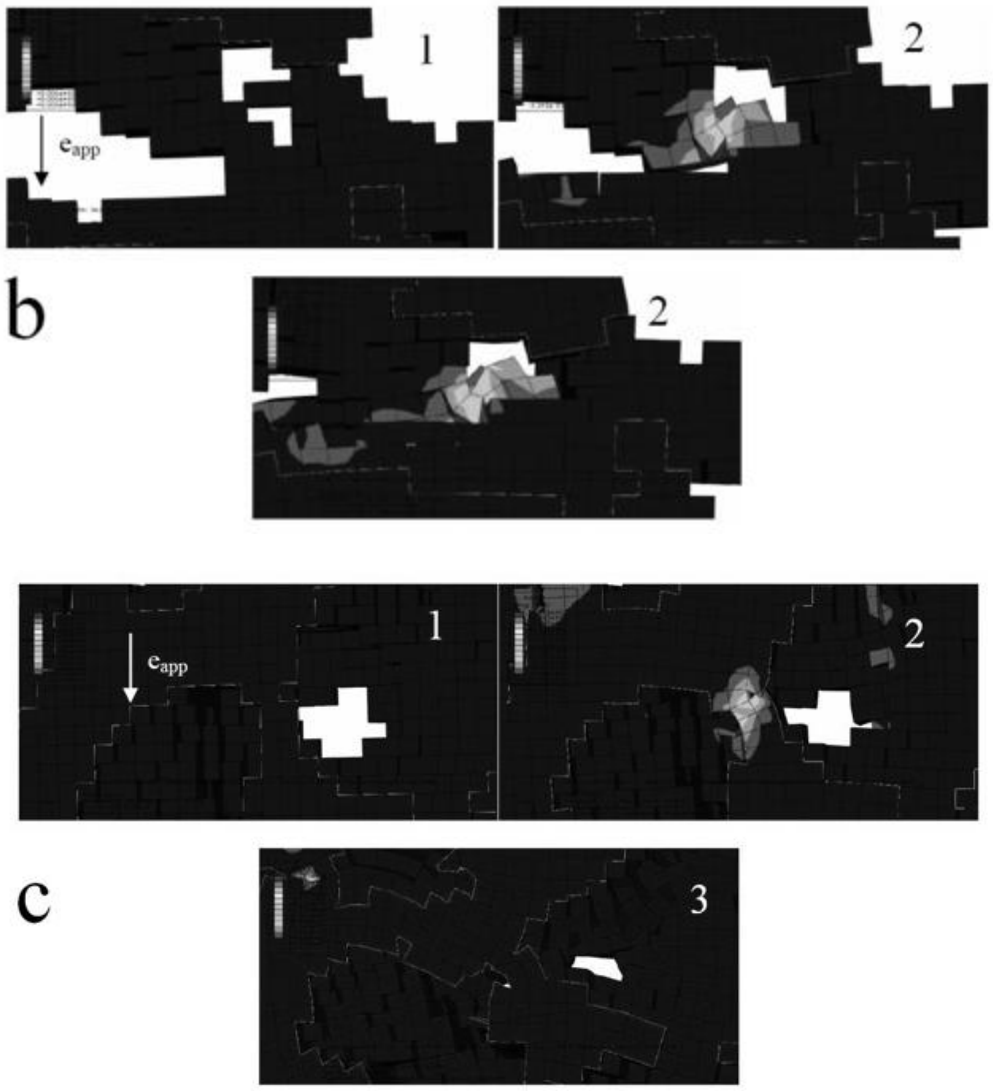

Figure 4.5 continued

The complex mesostructure of foam induces wide variation of local strains with application of a macroscopic strain. Figure 4.6 illustrated the distinction of applied macroscopic engineering strain from the ABAQUS simulations and local engineering strain in cell walls (which may be compressive, tensile, or shear).

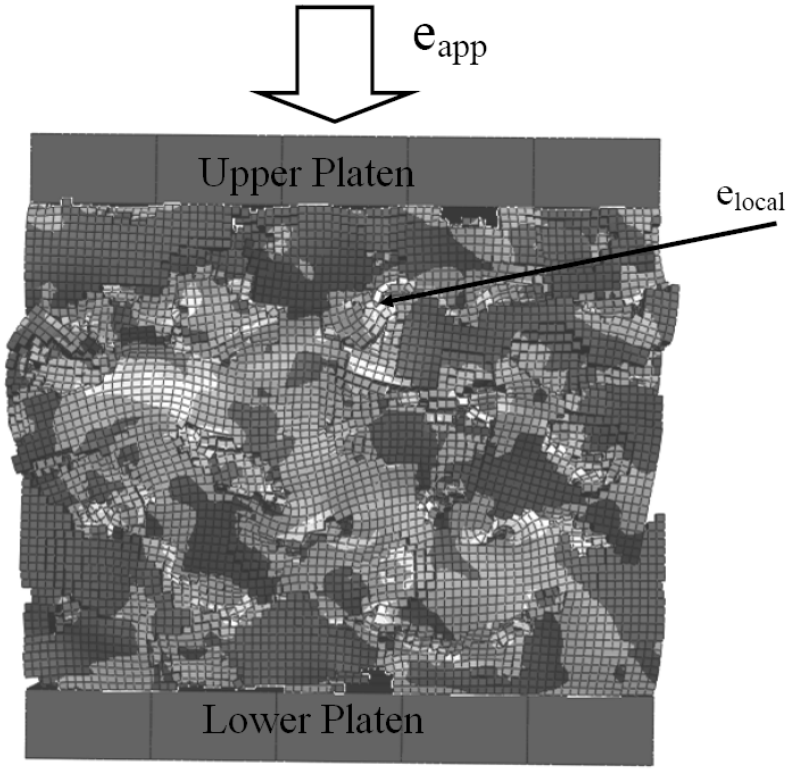

Figure 4.6: Schematic of the macroscopic compression resulting in local non-compressive strains.

The distribution of the maximum principal strain, henceforth referred to as "tensile strain", from the ABAQUS simulations is shown in Figure 4.7. A lognormal cumulative distribution fit was employed, overlaid on the ABAQUS distribution in Figure 4.7. It is noted that these distributions would effectively change very little if true strain in the cell walls were used instead, since most of these data are below 10% strain. However, the extreme value tails corresponding to low probability occurrence would shift to the right for the higher applied strain levels, since strains of 30% and above are realized. The parameters for the tensile strain fits can be found in Table 4.2(a). The data in Figure 4.7 essentially portrays the probability of the local strain, e_{local}, exceeding a given tensile strain, $e_{tensile}$, for applied compressive strain levels, e_{app}. For example, at an applied

compressive strain of e_{app} = 6.9%, the probability of finding a region with local strain, e_{local}, greater than 1% ($e_{tensile}$) is about 40%. This is significant because the data provides an idea that some partition of the material is experiencing a local strain great than the applied compressive strain.

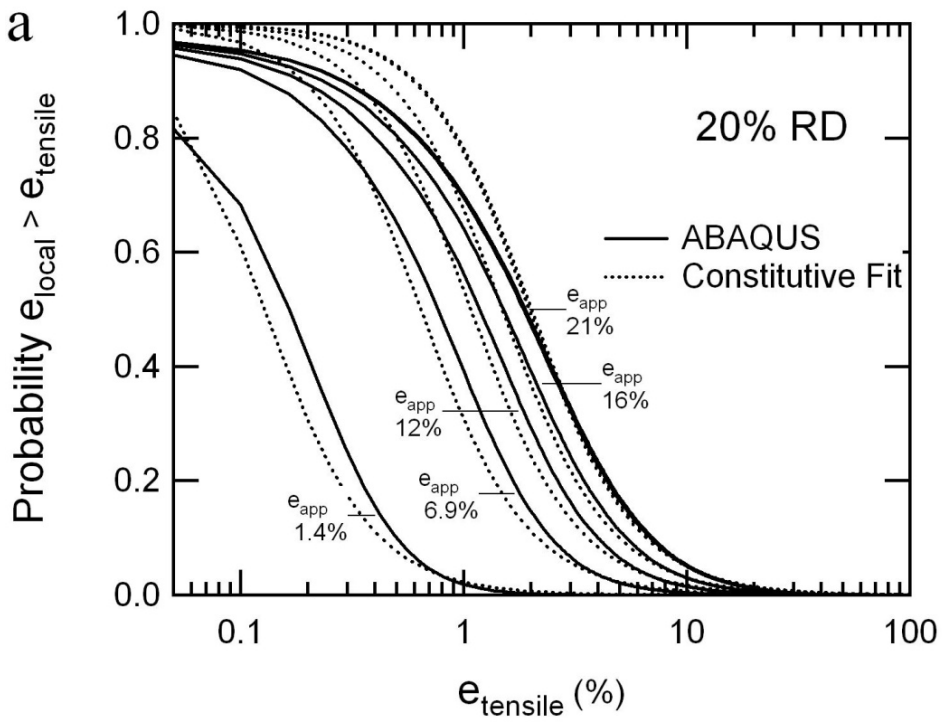

Figure 4.7: Cumulative local tensile strain distributions from the ABAQUS simulations. Three relative densities are showen; a) 20%, b) 30%, and c) 40% and applied average compressive strain. The fit of equation 4.2 with the parameters found in Table 4.2a are overlaid for comparison.

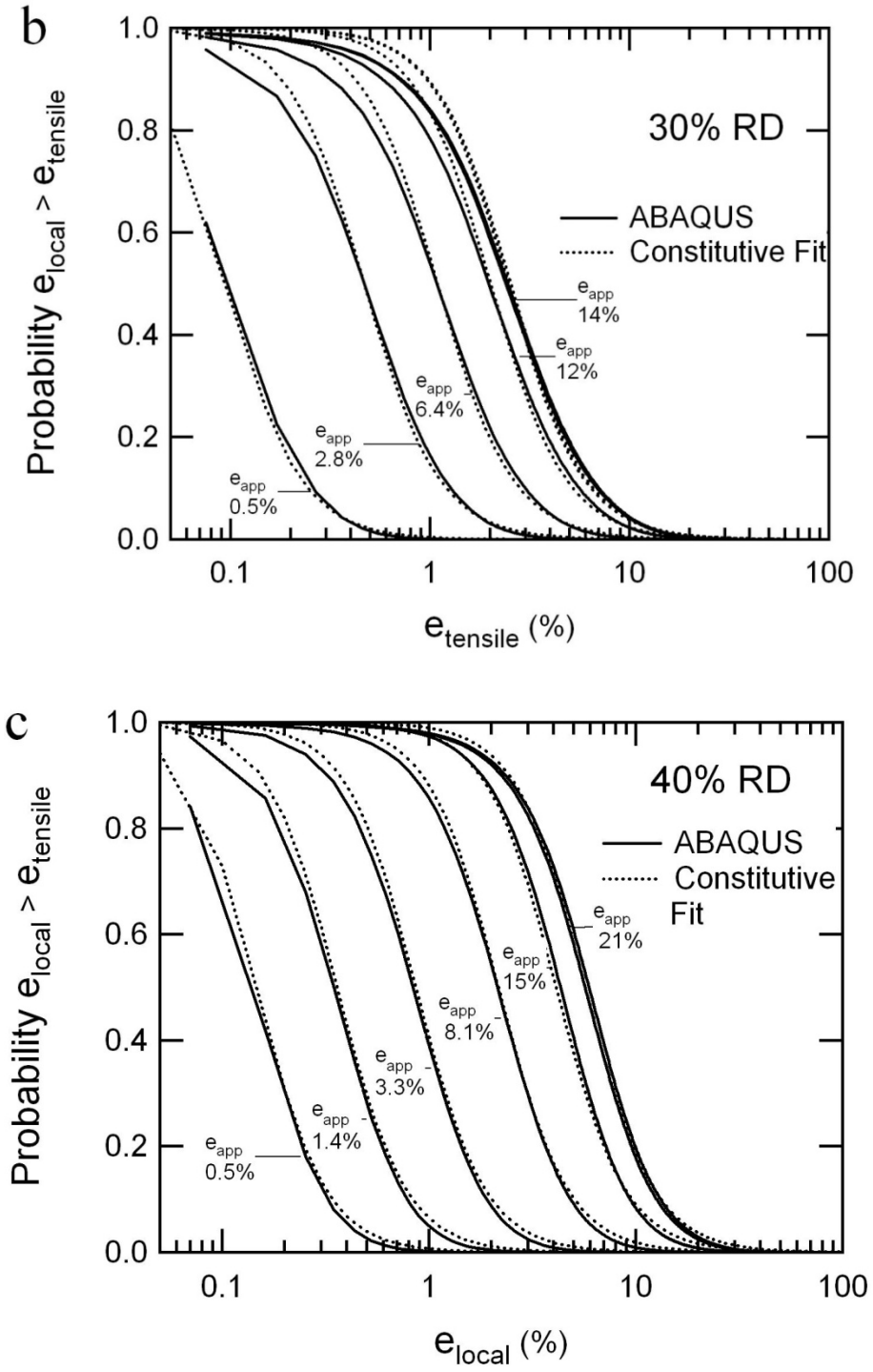

Figure 4.7 continued

The cumulative probability distribution of maximum engineering shear strain magnitude (based on the difference of maximum and minimum principal strains), henceforth

referred to as “shear strain”, is shown in Figure 4.8, again with the simulation results overlaid in the same figure. The parameters for the shear strain fits can be found in Table 4.2b.

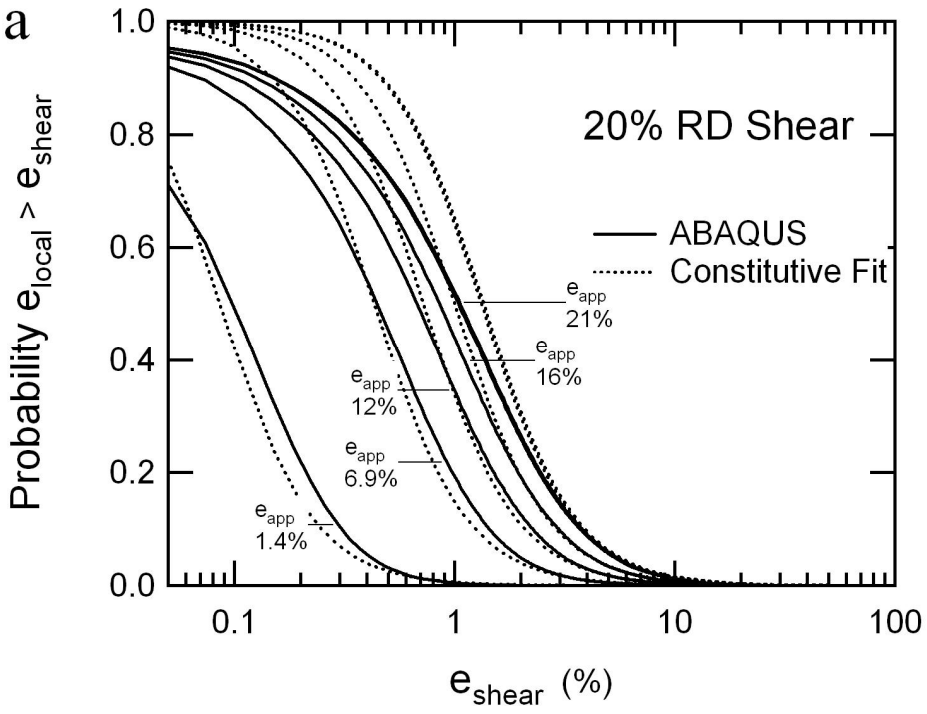

Figure 4.8: Cumulative local tensile strain distributions from the ABAQUS simulations. Three relative densities are showen; a) 20%, b) 30%, and c) 40% and applied average compressive strain. The fit of equation 4.2 with the parameters found in Table 4.2b are overlaid for comparison.

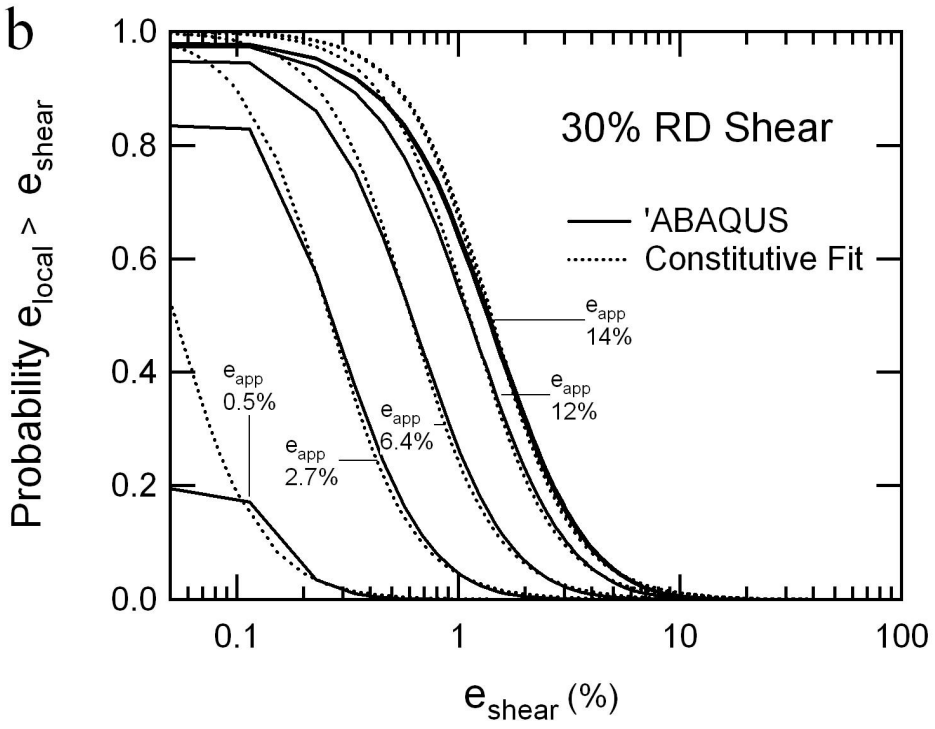

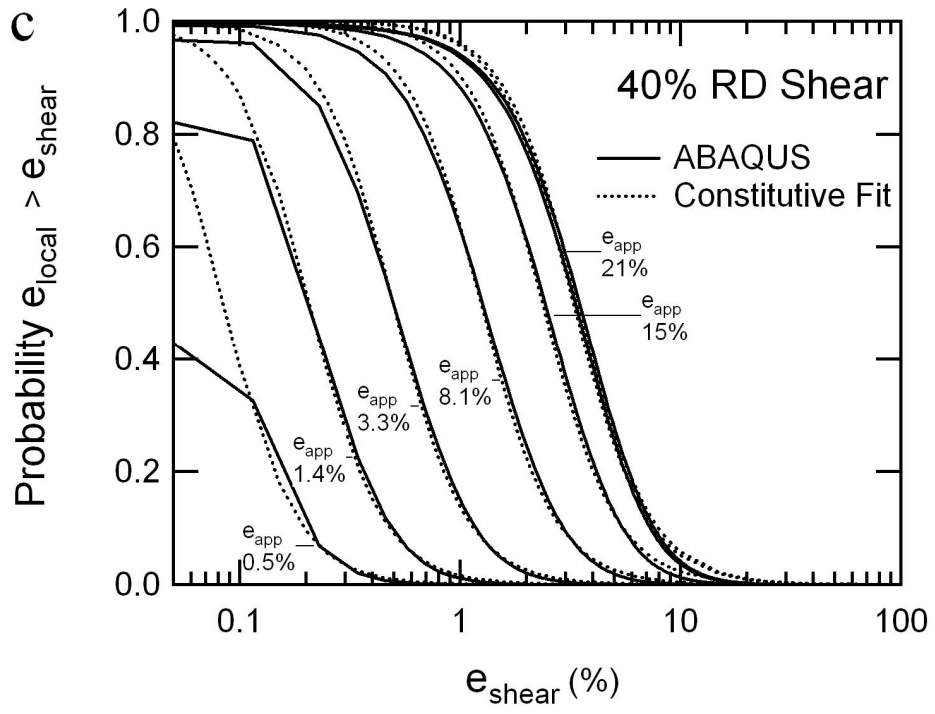

Figure 4.8 continued

Table 4.2: Lognormal Cumulative PDF Fit Parameters

a) Tensile Fit

Relative Density	A	B	C
20	1.2	4.9	11.11
30	2.8	5.325	9.09
40	2.1	5.975	5.00

b) Shear Fit

Relative Density	A	B	C
20	0.35	4.775	9.68
30	0.15	5.225	4.54
40	0.55	6.0	5.18

4.5 Discussion

Figure 4.2 confirms the dependence of the stiffness on relative density of foams and the independence of T_g on relative density, as previously discussed in Chapter 3. The p-values from ANOVA showed that the 20 and 30% RD samples fit a normal distribution of both glassy and rubbery stiffness. This allows the mechanical testing and modeling based on one sample to be projected to other samples of similar relative density. The 40% RD samples failed to show this same correlation, as the fourth sample significantly deviated from the remaining samples. Measurement of relative density showed that the fourth sample was 37.6% RD, while the other three samples average 41% RD. Neglecting this sample from ANOVA gave a p-value of 0.877 for the glassy stiffness and a p-value of 0.936 for the rubbery stiffness. So long as the relative densities of these materials are similar, the mechanical properties do not statistically differ across samples. While the ANOVA for the T_g did show a significant amount of variation across the samples for two of the three relative densities, analysis of all T_g values gave a mean of 66.8°C with a

standard deviation of 3.7°C, which is on par with the standard deviation with the relative densities and supports the hypothesis that T_g is consistent across the samples.

Local stresses and strains in the SMP foam materials are considered as a function of relative density and applied compressive strain. As such, they provide a means to understand potential damage mechanisms in the foams under compressive loading. Although the damage may be microscopic in nature, it can impact foam performance, including progressive fatigue degradation under high strain cyclic loading that the foams are expected to experience in applications involving repeated actuation.

The hyperelastic behavior of the base polymer was a reasonable approximation of deformation response of the material at a single temperature and strain rate. In addition to changing rate or temperature of deformation this approach would require further testing and characterization if the chemistry of the base polymer changed. Even with these limitations, the present results here are expected to have general applicability, especially for epoxy shape memory polymers which have similar structure and are often deformed at or near the temperature considered here.

Figure 4.4 shows that the material parameters and mesh are generally representative of the foam from a global stand point, as the predicted stress-strain behavior of the foam matches fairly well with experimental results. The simulation appears to provide a good fit for the 20% RD foam and performs reasonably well for the 30% RD foam. There is more divergence in the 40% RD foam, but seems suitable as an approximation. The

divergence could be due to insufficient resolution to capture important features at higher relative densities or it could be caused by the approximation that assigned material properties do not change with damage once a local failure criterion is met. Another potential source of error is a difference in the simulated temperature and the experimental temperature. For purposes of analyzing the mesoscopic distribution of cell wall response to imposed global deformation, however, the match between the experimental and simulated results is deemed acceptable.

The trend in Figure 4.5 highlights the effect of relative density on deformation, in that there is a distinct difference between the 20% RD foam and foams with higher relative density. The 20% RD foam predominately deforms by bending of struts aligned parallel to the direction of compression while the other materials (with thicker cell walls) deform predominately via shear at the junction of struts. This finding was representative of the cell structures over the entire volume of the simulation. This difference should have an effect on failure mode and failure sites as a function of relative density, and even perhaps affect how damage ultimately propagates under cyclic deformation.

Figures 4.7 and 4.8 demonstrate that for both local tensile and shear strains, a small fraction of the foam struts experiences extremely high strains. This is significant since some fraction of the material experiences local tensile strains that exceed the tensile failure strain even when modest global compressive strains are applied. The similarity of the shape of the distribution as a function of applied strain and relative density is striking. The fit equation consistently diverges from the simulation results at lower applied strains

and increases with decreasing relative density. This could be an artifact of the log scale for the strain or a problem of applying the chosen distribution function to low strains. However, the fit is accomplished through only three parameters; two to determine the shape of the distribution and one to calibrate the position of the distribution.

4.6 Conclusions

1. Samples received from the material supplier with similar relative densities exhibit statistically similar stiffness in both glassy and rubbery regions as well as statistically similar values of T_gs.
2. Using a hyperelastic material model, finite element meshes constructed from CT-images of actual 3D micostructures can reasonably predict compressive stress-strain response for foams over a range of relative densities.
3. The majority of deformation in the 20% RD foam is localized bending in the vertical struts while in the 30% and 40% RD foams, the deformation is localized shear near the junctions of struts.
4. Shear and tensile strains are highly localized at all relative densities of materials.
5. Both the local tensile and the local shear strain cumulative probability distributions can be fit as lognormal as a function of applied compressive strain. This encourages pursuit of such simulations to support modeling of fatigue degradation under cyclic loading.

CHAPTER 5: CYCLIC COMPRESSIVE BEHAVIOR OF EPOXY SHAPE MEMORY POLYMERS

5.1 Introduction

Shape memory polymer foams have significant potential in aerospace and biomedical applications, but their thermomechanical behavior and damage response under cyclic deformation is not well understood. Chapter 2 briefly touched on the effect of deformation temperature on the cyclic response, while Chapter's 3 and 4 only focused on monotonic response. In this chapter the effect of strain and relaxation time on cyclic behavior of epoxy shape memory polymers with relative densities of 20, 30, and 40% was investigated. For each relative density, foams were cyclically deformed under conditions of strain control with periodic hold times (0 s, 40 s, and 300 s). During the hold time the sample was totally unconstrained; neither stress nor a strain was applied. A 17% relative density foam was periodically imaged at 12μm resolution using microcomputed tomography scans to determine the mesostructural response to cyclic deformation of 40, 60, or 80% engineering strain. These scans provided global quantitative data as well as qualitative regional information on cyclic deformation mechanisms. Individual struts were isolated and tracked across the scans to qualitatively show local response to cyclic conditions. The experimental data are discussed in light of finite element modeling of the foams (Chapter 4) to better understand the cyclic deformation behavior.

5.2 Background

Cyclic and fatigue damage behaviors for SMP foams have not been fully explored. The two SMP foam papers (M. A. Di Prima, et al., 2007; Tobushi, et al., 2004) that touched on the subject noticed an effect of cycling at different peak strain levels, and temperatures. Work on cyclic loading in conventional polymer foams have investigated multiple modes of fatigue in glassy foams (Zenkert and Burman, 2008) and the effect of mesostructure (auxetic, as processed, etc.) on tension-tension fatigue (Bezazi and Scarpa, 2009). The glassy polymer study covered tensile, compressive, and shear fatigue conditions but only investigated small engineering strains, which are not relevant to the large strain regimes in which SMP foams must operate. The auxetic foam study was conducted on a flexible foam that was cycled to large strains, but the relative density was much lower than the SMP foams of interest here, 5-10% RD. Thus, this Chapter seeks to address the gap in knowledge in shape memory polymer foam fatigue behavior under relevant large strain conditions.

5.3 Experimental

Materials and Specimens

The material used in this work was an epoxy foam with the trade name TEMBO® DP5.1 Foam provided by Composite Technology Development (CTD). Chemical and processing details of the material are proprietary, but the material can be considered as a two-part thermoset epoxy network. The relative densities (RD), density of the foam normalized to the density of the resin, of the samples were 14 to 20%, 30%, and 40%.

Experimental Apparatus

To determine the T_g, a Thermal Analysis Instruments DMA Q800 was used with film tension clamps. The value of T_g is near 85°C and was evaluated for each batch of materials. The other thermomechanical tests were performed using a MTS Insight 2 uniaxial mechanical test frame with an attached thermal chamber. A thermocouple was located inside the thermal chamber and was placed adjacent to the sample. The crosshead displacement was used to determine compressive engineering strain. In this paper, sample strain levels are reported in terms of engineering strain in all cases.

Experiments

Three types of tests were performed to measure bulk properties/responses: DMA, shape recovery, and cyclic compression. The shape memory tests were further composed of free strain and constrained shape recovery tests.

DMA. Rectangular specimens were cut to 5x25x1 mm and inserted in the tensile film clamps. The sample was equilibrated at 25°C for two minutes and then heated to 125°C at a rate of 5°C/min. The test was run under engineering strain control; with a strain of 0.1%, a preload of 0.01 N, a force track rating (ratio of static load to dynamic load) of 150%, and a frequency of 1 hz.

Cyclic compression experiments. In these tests, each specimen was cyclically compressed in the load frame to a target strain endpoint for one hundred cycles. The cylindrical specimens were compressed at an engineering strain rate of 0.0025 s^{-1}. The temperature

of this test was 110°C to ensure that the behavior was fully reversible in a mechanical sense. Both the engineering strain endpoint and the time between each cycle (hold time) were varied independently. The engineering strain targets were 40, 60, 80, and 85% while the hold times were 0 s, 40 s, and 300 s. For the best resolution, a 100 N load cell was used with a load limit of 95 N (the load limit was set but not used). To promote full contact of the platen on the specimen, a preload of 0.05N was used. Statistical analysis of the cycle to failure data was performed using Igor Pro 5.04A (2005) built in one-way Analysis of Variables (ANOVA) tool with the Tukey HSD option for pair wise comparison. Failure was defined to occur at the cycle at which the rate of residual strain accumulation increased rapidly relative to steady prior trajectory with accumulated cycles. This represents the point of accumulated progression of irreversible strain localization due to cell wall damage.

X-ray microCT scanning. Samples of interest were scanned using a Scanco Medical vivaCT 40 x-ray micro-CT scanner at the Georgia Institute of Technology Orthopedic Bioengineering Laboratory. The nondestructive nature of micro-CT imaging allows for iterative scanning. A single specimen was scanned, at 12μm resolution, and then cyclically compressed at an engineering strain rate of $0.0025s^{-1}$ to a maximum engineering strain of 40, 60, or 80%. Each specimen was compression 100 times and scanned after cycle number 1, 2, 3, 5, 7, 10, 17, 25, 50, 75, and 100. Isolation of the same foam region across the scans was performed visually using ImageJ software for comparison and Automated Image Registration for image alignment (Rasband, 1997-2008; Woods, 2002). MRIcro software was used for fine tuning the area selection and the

generation of the 3D images (Rorden, 1999-2005). Bulk foam properties were determined using the ScanCo analysis software.

5.4 Results

The effect of packaging temperature relative to T_g on the shape recovery response is illustrated in Figure 5.1. Figure 5.1(a) shows the constrained stress recovery response at packaging temperatures above and below T_g (0.9, 1.0, 1.1, and 1.2 T_g, with T_g in °C) for a foam with a relative density of approximately 14%. Figure 5.1(b) has the free strain recovery response for the same material and the same packaging conditions.

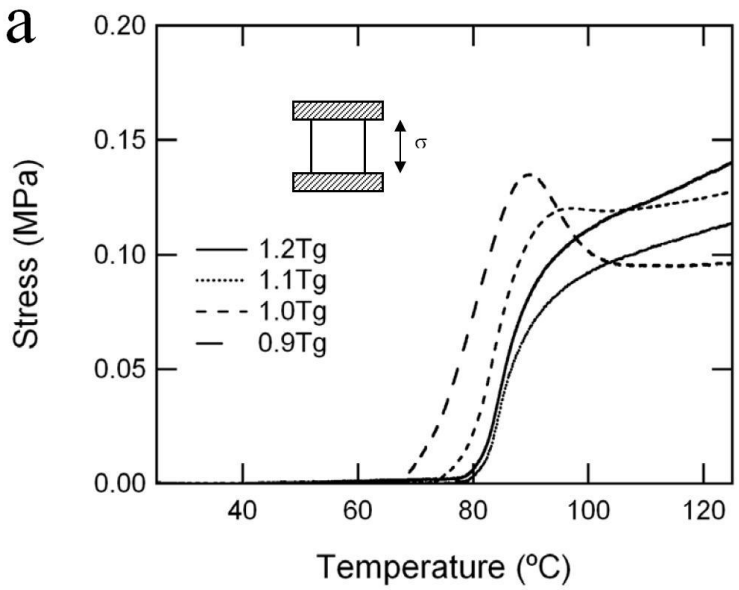

Figure 5.1: Shape recovery properties of 14% RD as the packaging temperature is varied. Free strain recovery (a) tracks the unconstrained recovery of the material as a function of temperature, while constrained stress recovery (b) tracks the constrained stress of the material as a function of temperature.

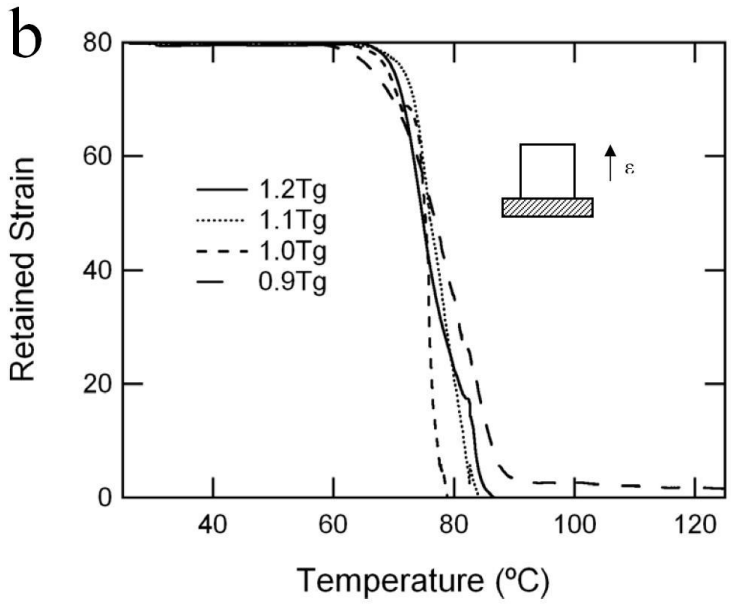

Figure 5.1 continued

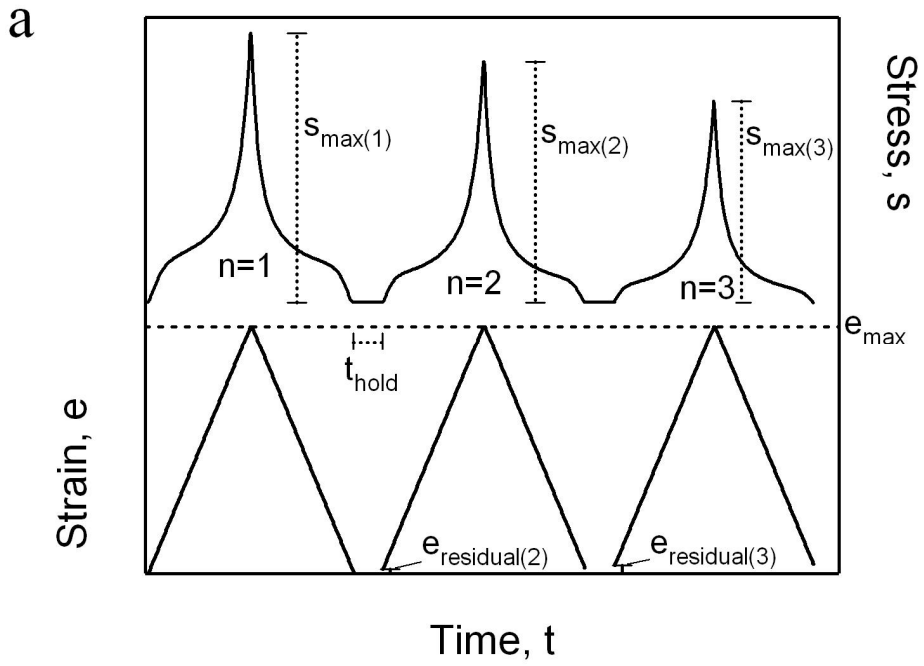

Figure 5.2: Schematic of the cyclic compression test.
In this test the sample is compressed to the same maximum strain (e_{max}) each cycle while the residual strain and drop in maximum stress is measured. A hold period can be inserted between each cycle while the sample is unloaded. Representative cyclic compression results are shown (b) for 20% RD to 80% strain; first and every 10th cycle shown.

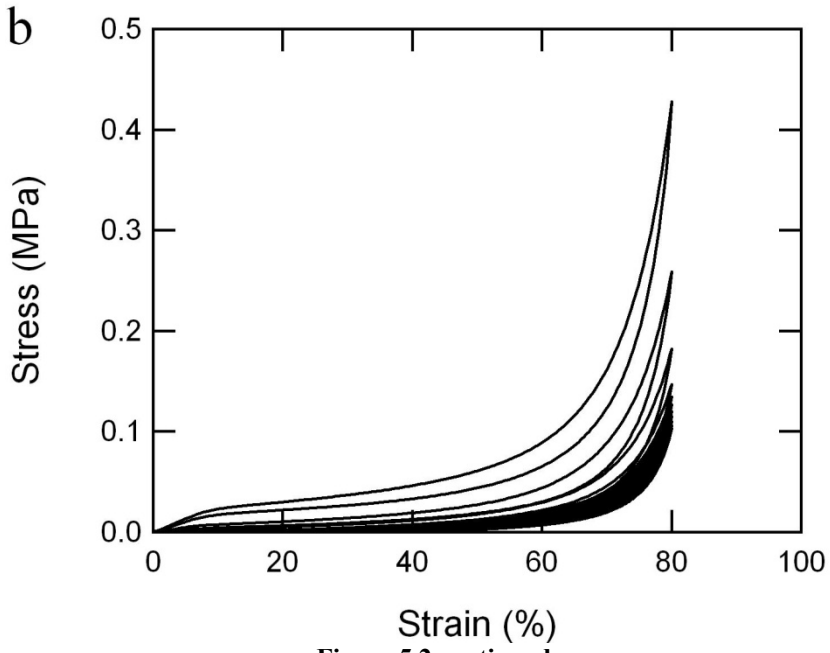

Figure 5.2 continued

A schematic defining the cyclic compression test: test profile, normalized maximum stress, and residual strain is shown in Figure 5.2. Essentially, compressive strain is applied to a maximum level, e_{max}, then the sample is unloaded by moving the crosshead until the preload force is reached; for non-zero hold times the crosshead is further raised to completely unload the sample. The sample is held in this unloaded state for a hold time, t_{hold}, and then reloaded to the same e_{max} level, taking note of the residual strain on the sample after the cycle, including the hold time. This process is further illustrated by the cyclic compression results shown in Figure 5.2(b); the first and every 10^{th} cycle shown for clarity, Figures 5.3-5.5 contain the effect of the maximum strain on the cylic response of the SMP foam. Figure 5.3 tracks the cyclic response for 20% RD foam for maximum compressive strains of 40, 60, 80, and 85%. Figure 5.3(a) presents the increase in residual strain with compressive cycles and 5.3b) tracks the decrease in normalized

maximum stress with cycles. Figure 5.4 tracks the cyclic response for 30% RD foam for maximum compressive strains of 40, 50, and 60%. Figure 5.4(a) shows the increase of residual strain with compressive cycles and Figure 5.4(b) plots the decrease in normalized maximum stress with cycles. Figure 5.5 tracks the cyclic response for 40% RD foam for maximum compressive strains of 40, 50, and 60%. Figure 5.5(a) shows the increase in residual strain with compressive cycles and 5.5b) the decrease in normalized maximum stress with cycles.

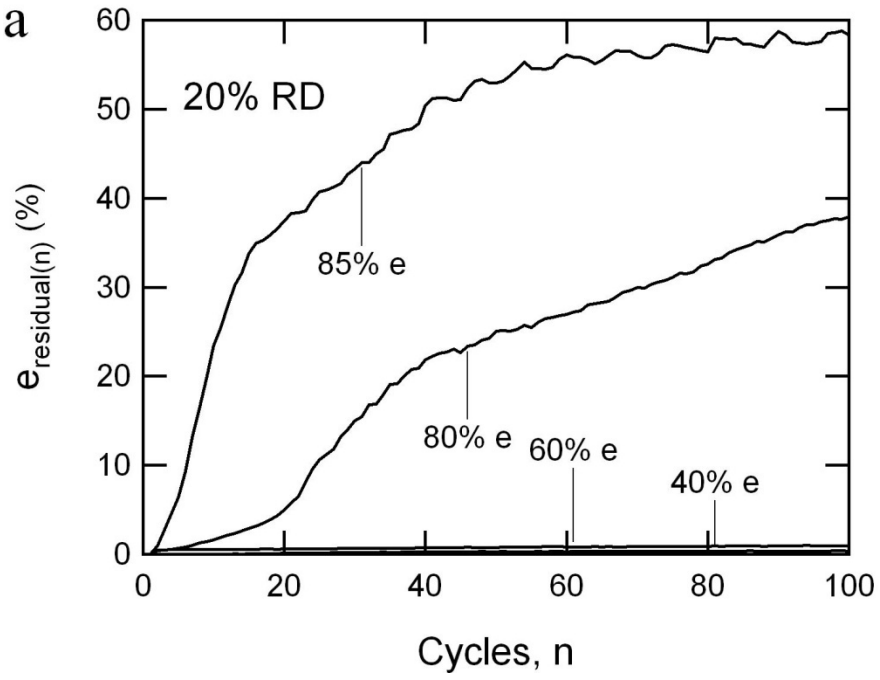

Figure 5.3: Cyclic behavior of 20% RD foam for 100 cycles at varied maximum strains. Maximum engineering strains were 40, 60, 80, and 85% with no hold between cycles. Both the residual strain (a) and the maximum stress normalized to the first cycle (b) are tracked

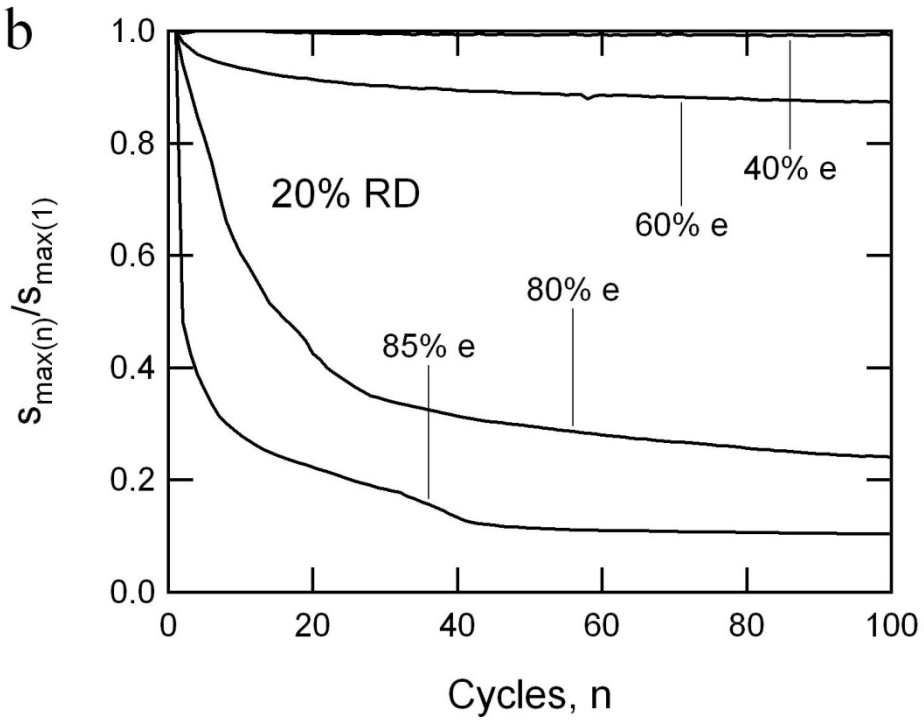

Figure 5.3 continued

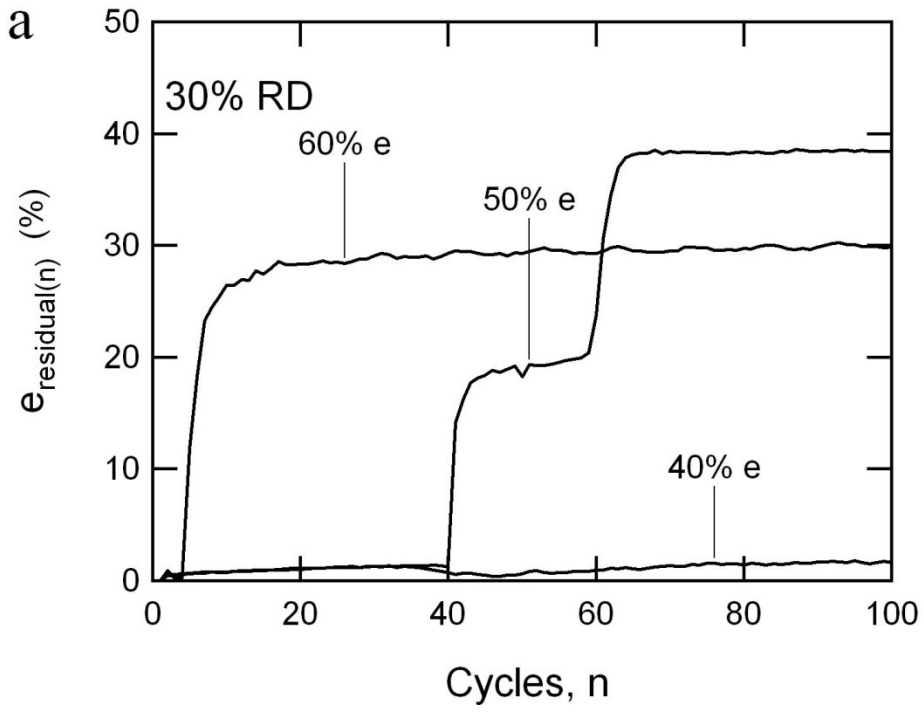

Figure 5.4: Cyclic behavior of 30% RD foam for 100 cycles at varied maximum strains. Maximum engineering strains were 40, 50, and 60% with no hold between cycles. Both the residual strain (a) and the maximum stress normalized to the first cycle (b) are tracked

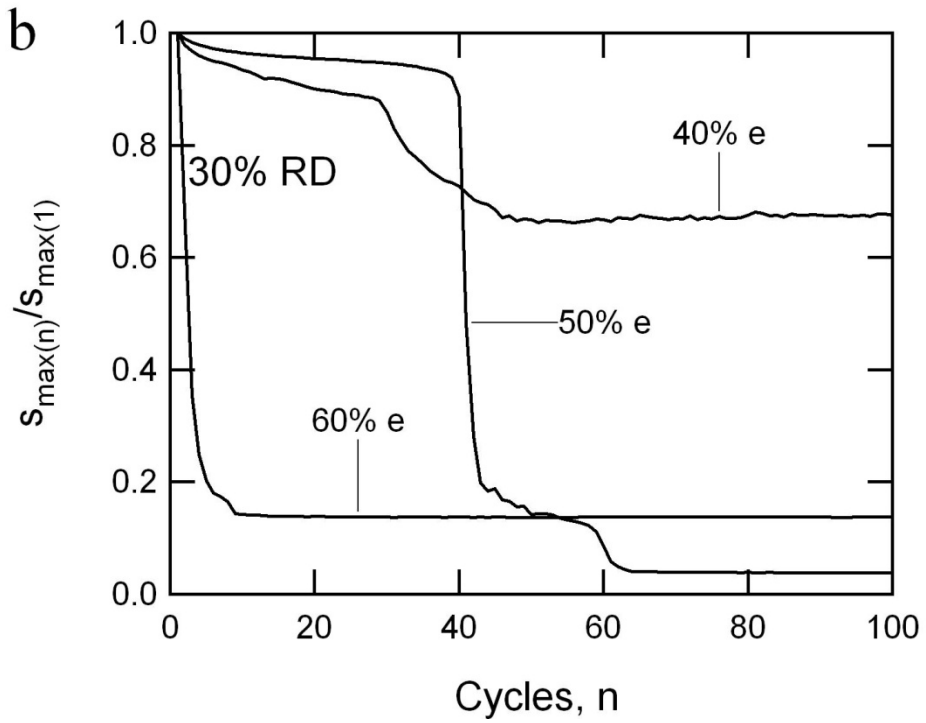

Figure 5.4 continued

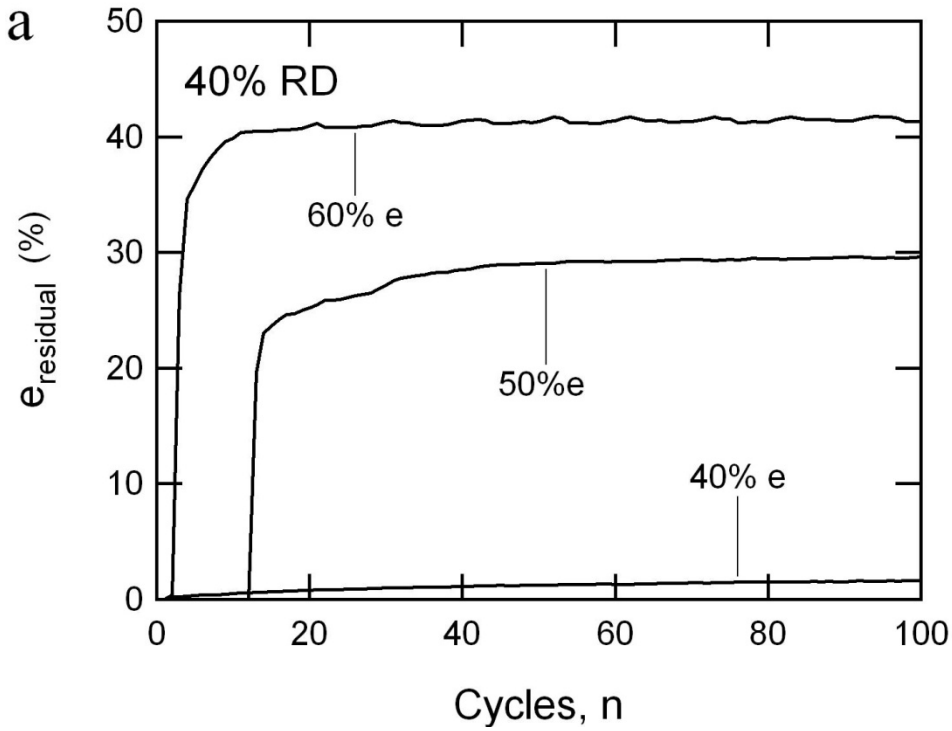

Figure 5.5: Cyclic behavior of 40% RD foam for 100 cycles at varied maximum strains. Maximum engineering strains were 40, 50, and 60% with no hold between cycles. Both the residual strain (a) and the maximum stress normalized to the first cycle (b) are tracked

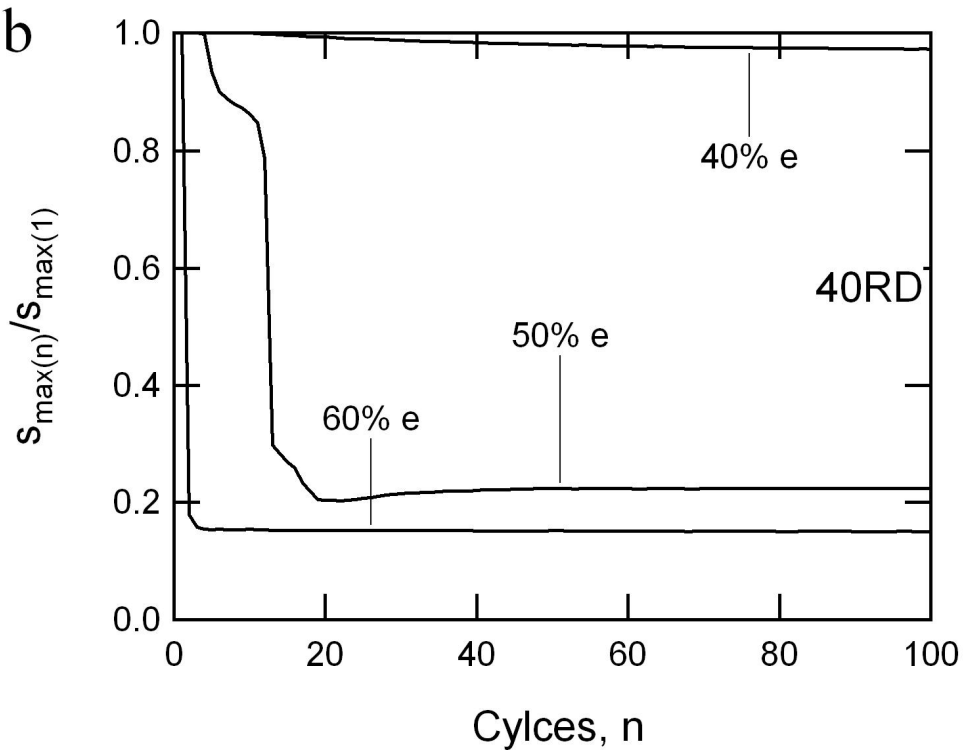

Figure 5.5 continued

Figures 5.6-5.8 show the effect of hold time between compressive cycles on the cyclic response of the SMP foam. Figure 5.6 tracks the cyclic response for 20% RD foam for relaxation times of 0 s, 40 s, and 300 s at an engineering strain of 80%. Figure 5.6(a) plots the increase in residual strain with compressive cycles. Figure 5.6(b) shows the decrease in normalized maximum stress with cycles. Figure 5.7 tracks the cyclic response for 30% RD foam for relaxation times of 0 s, 40 s, and 300 s at an engineering strain of 50%. Figure 5.7(a) plots the increase in residual strain with compressive cycles, and Figure 5.7(b) shows the decrease in normalized maximum stress with cycles. Figure 5.8 tracks the cyclic response for 40% RD foam for relaxation times of 0 s, 40 s, and 300 s at an engineering strain of 50%. Figure 5.8(a) plots the increase in residual strain with

compressive cycles, and Figure 5.8(b) plots the decrease in normalized maximum stress with cycles. Figures 5.6-5.8 present representative curves for each of the relaxation time conditions. The cycles to failure as a function of relative density and hold time are shown in Table 5.1. If the sample did not fail within the 100 test cycles, the cycles to failure was listed as 100 cycles (i.e., "runout") for comparison purposes. The check for statistical significance between hold times, ANOVA, for the 20% RD sample had a p-value of 0.142, for the 30% RD sample the p-value was 0.0715, and for the 40% RD sample the p-value was 0.734. The lower the p-value the more distinct the results are for set of tests.

Table 5.1: Cycles to Failure as a function of Hold Time.

Relative Density	T_{hold}= 0 s	T_{hold}= 40 s	T_{hold}= 300 s
20%	11	21	15
	26	33	22
	12	36	25
30%	41	100	37
	71	100	100
	24	100	51
40%	13	17	13
	14	9	11
	11	6	7

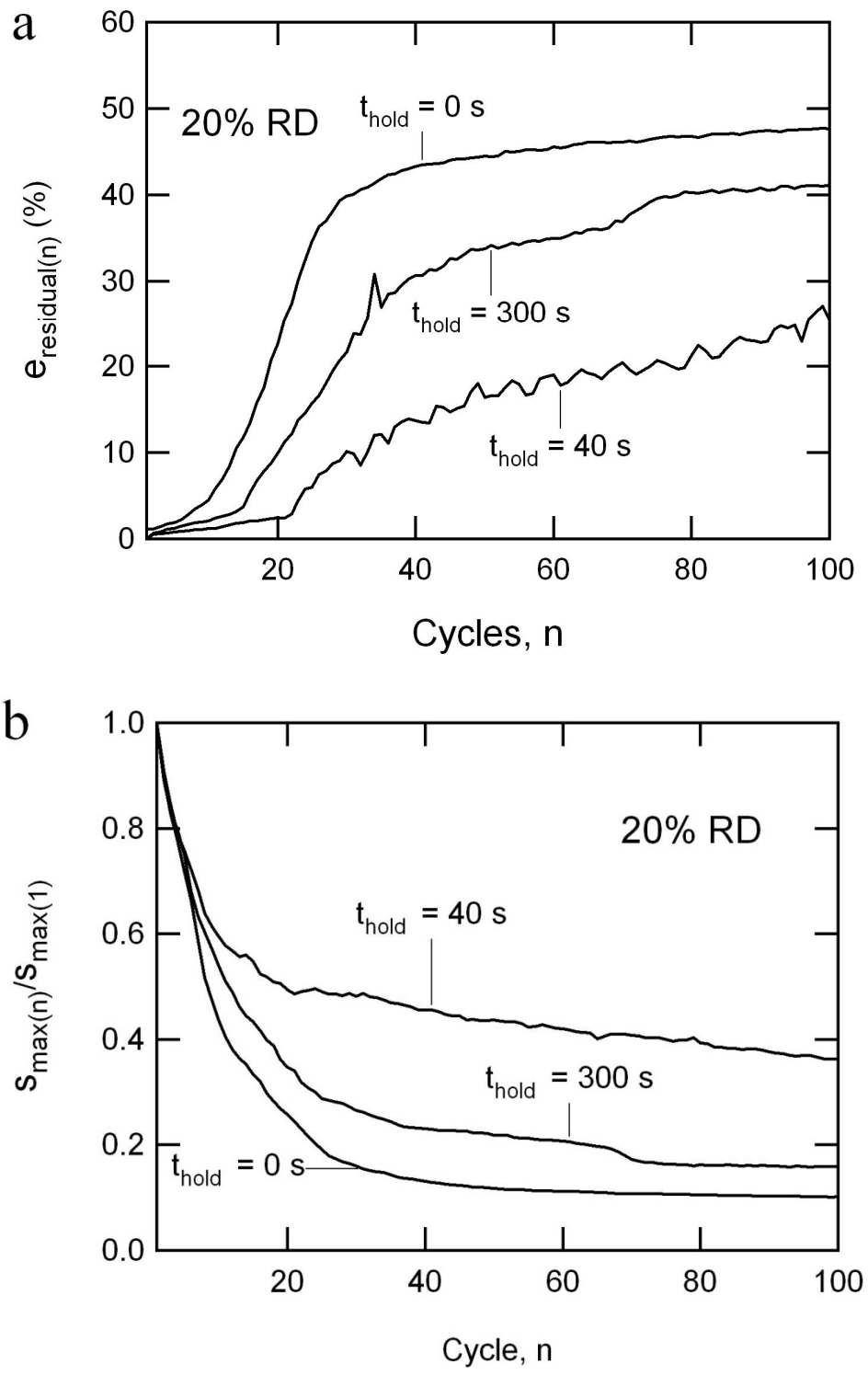

Figure 5.6: Cyclic behavior of 20% RD foam for 100 cycles with varying hold times. Hold times were 0, 40, and 300 s and the maximum engineering strain was 80%. Both the residual strain (a) and the maximum stress normalized to the first cycle (b) are tracked.

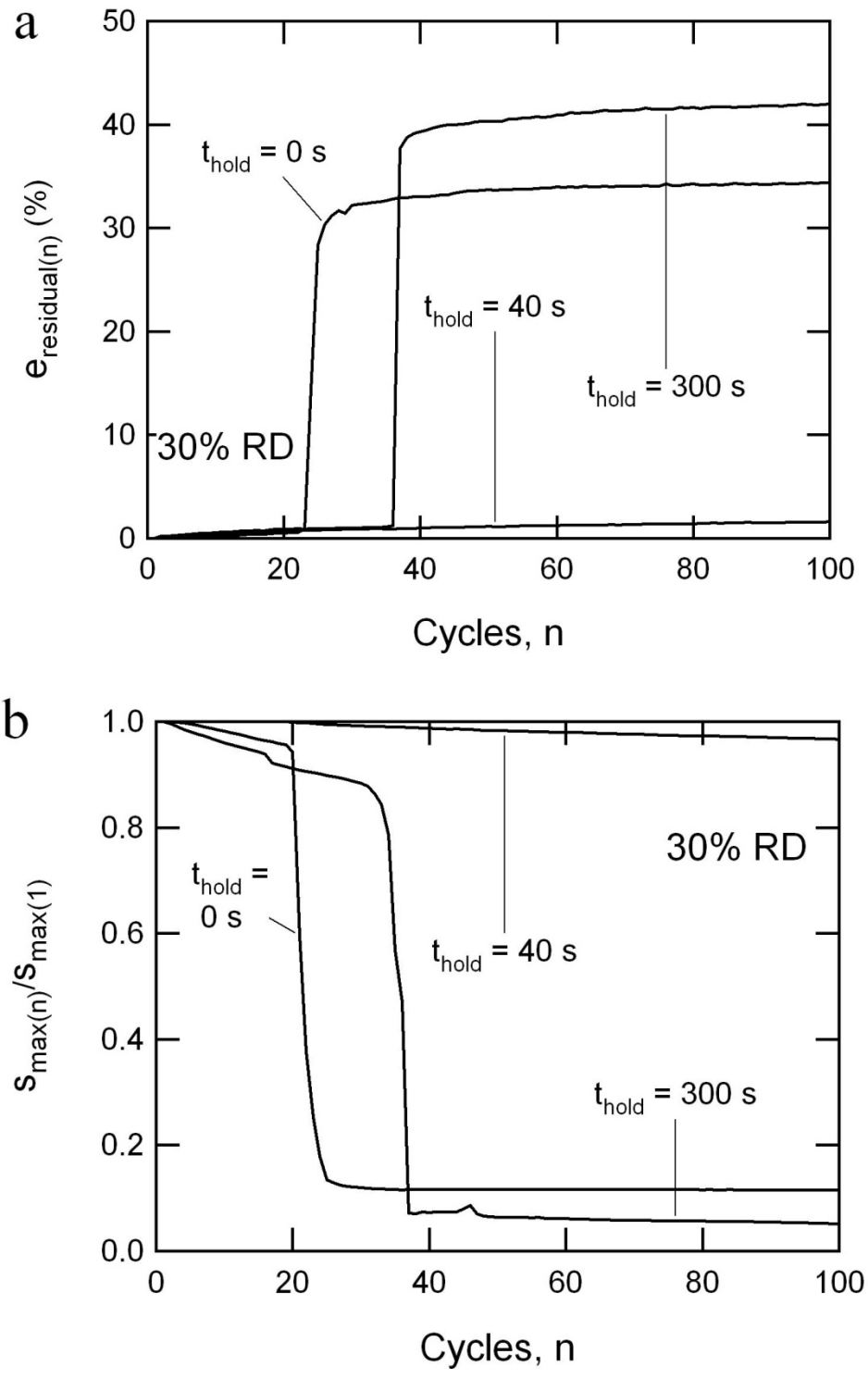

Figure 5.7: Cyclic behavior of 30% RD foam for 100 cycles with varying hold times. Hold times were 0, 40, and 300 s and the maximum engineering strain was 50%. Both the residual strain (a) and the maximum stress normalized to the first cycle (b) are tracked.

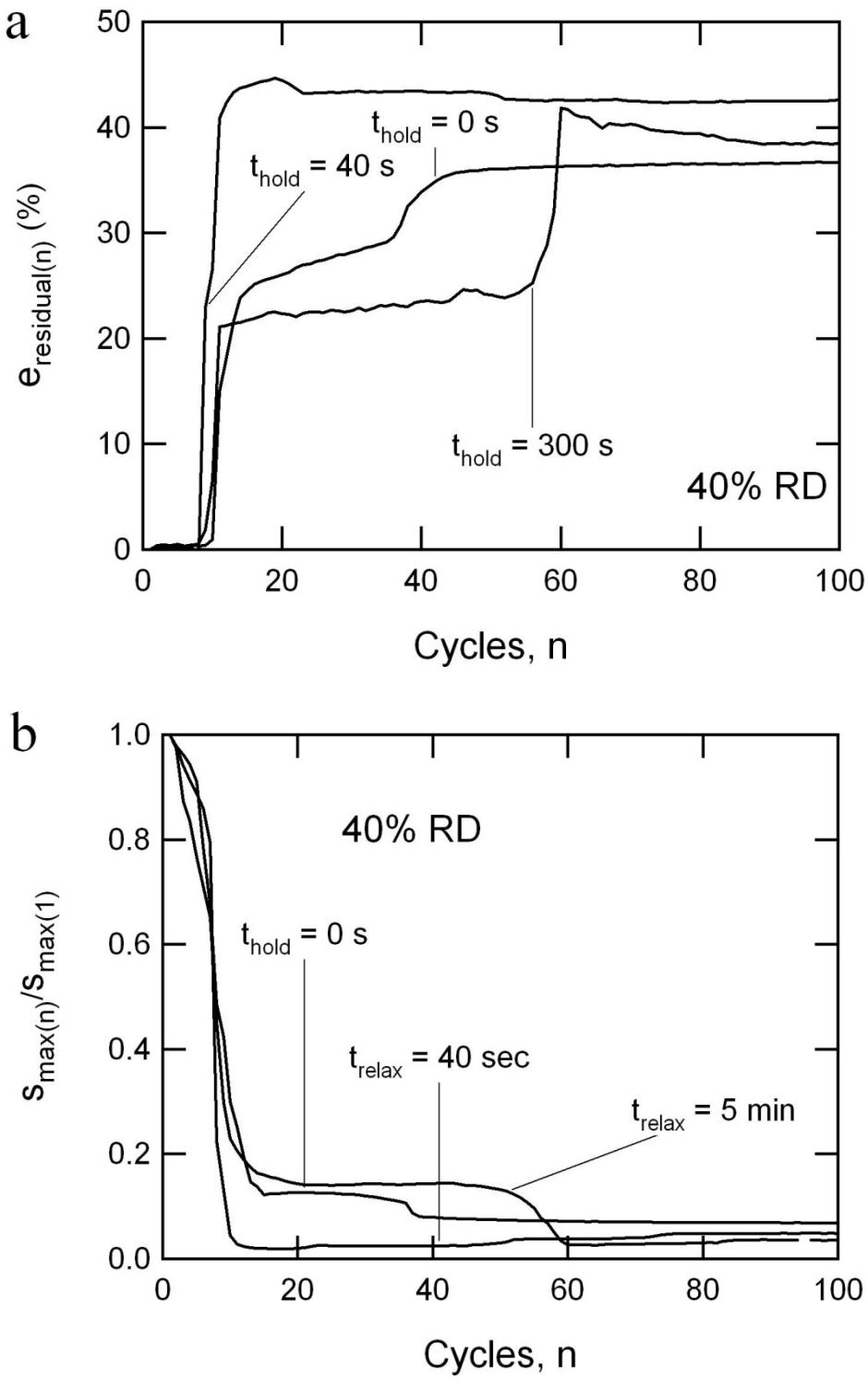

Figure 5.8: Cyclic behavior of 40% RD foam for 100 cycles with varying hold times. Hold times were 0, 40, and 300 s and the maximum engineering strain was 50%. Both the residual strain (a) and the maximum stress normalized to the first cycle (b) are tracked.

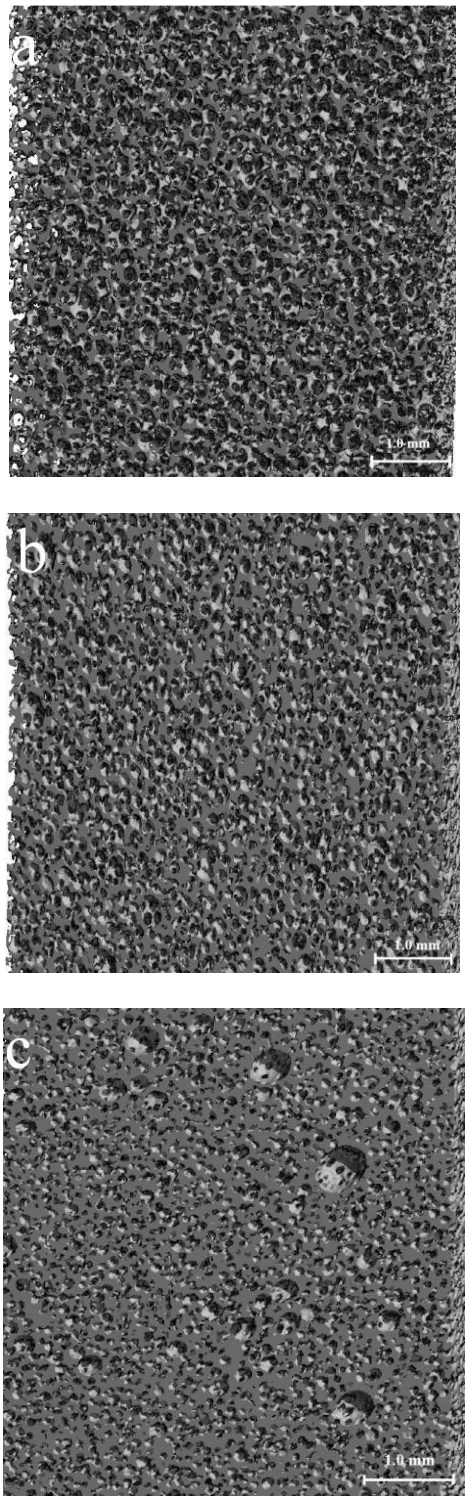

Figure 5.9: Representative micro-CT of DP5.1 foam.
The foams were a) 20% RD foam, (b) 30% RD foam, and (c) 40% RD foam.

Representative images of the foam structure for the three relative densities are shown in Figure 5.9. Structural data for the foams can be found in Chapter 3. The effect of cyclic compression on the microstructure as measured through micro-CT scans of the foam is illustrated in Figure 5.10. Samples of 17% relative density were cyclically compressed to maximum compressive engineering strains of 40, 60, and 80%. Figure 5.10(a) plots the effect of compressive cycles on the average strut thickness while, Figure 5.10(b) plots the effect of compressive cycles on the average cell spacing (pore size). The distribution of pore size for the as received material and after 100 compressive loading cycles are shown in Figures 5.10(c) 40% strain, 10(d) 60% strain, and 10(e) 80% strain. Figures 5.11(a) and 5.11(b) track the evolving geometry of two struts that undergo damage evolution through the 100 compressive cycles.

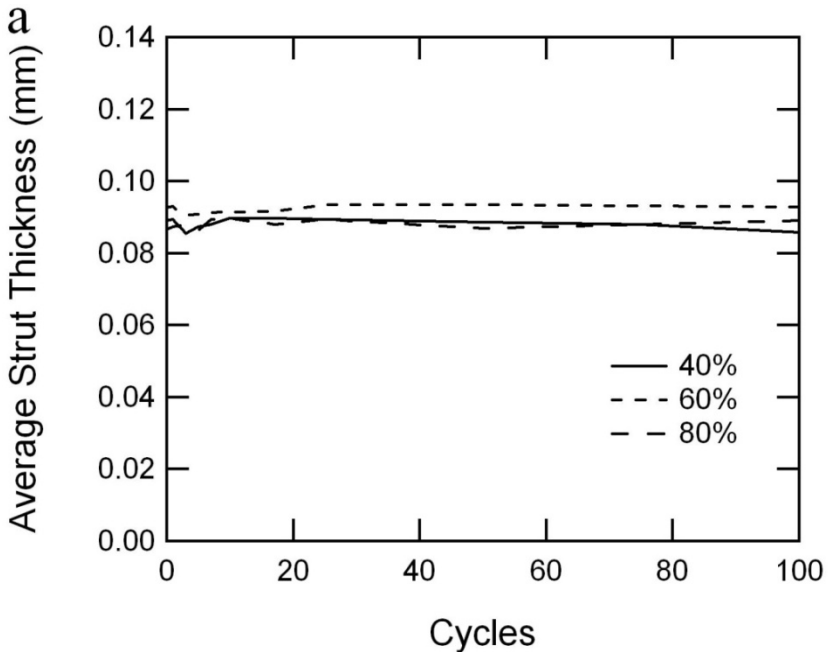

Figure 5.10: Quantitative structural response to cyclic deformation of 17% RD foam over 100 cycles. Maximum engineering strains were 40, 60, and 80%. The parameters tracked are average strut thickness (a), average cell spacing (b), cell spacing distribution for 40% strain (c), cell spacing distribution for 60% strain (d), and cell spacing distribution for 80% strain (e),

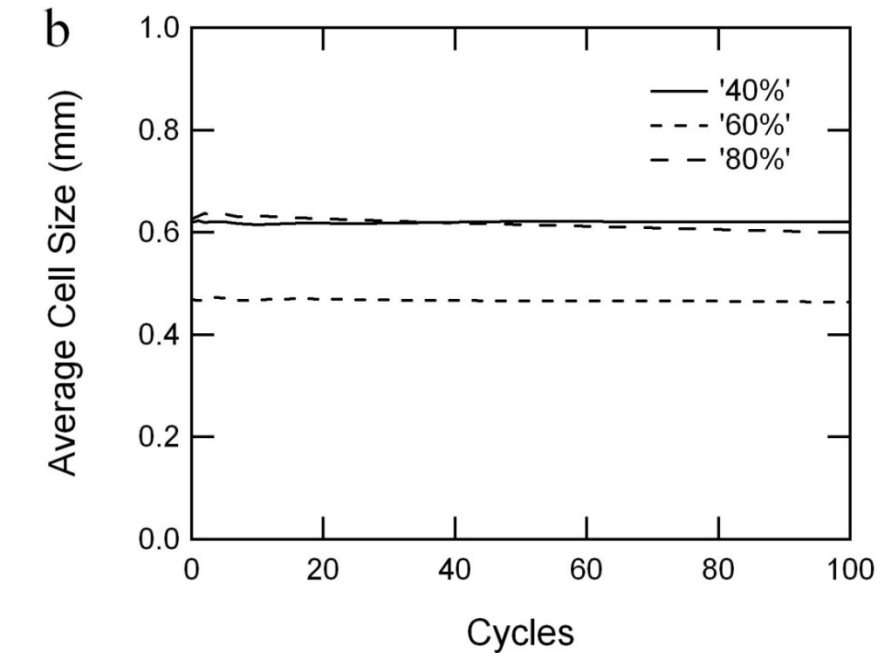

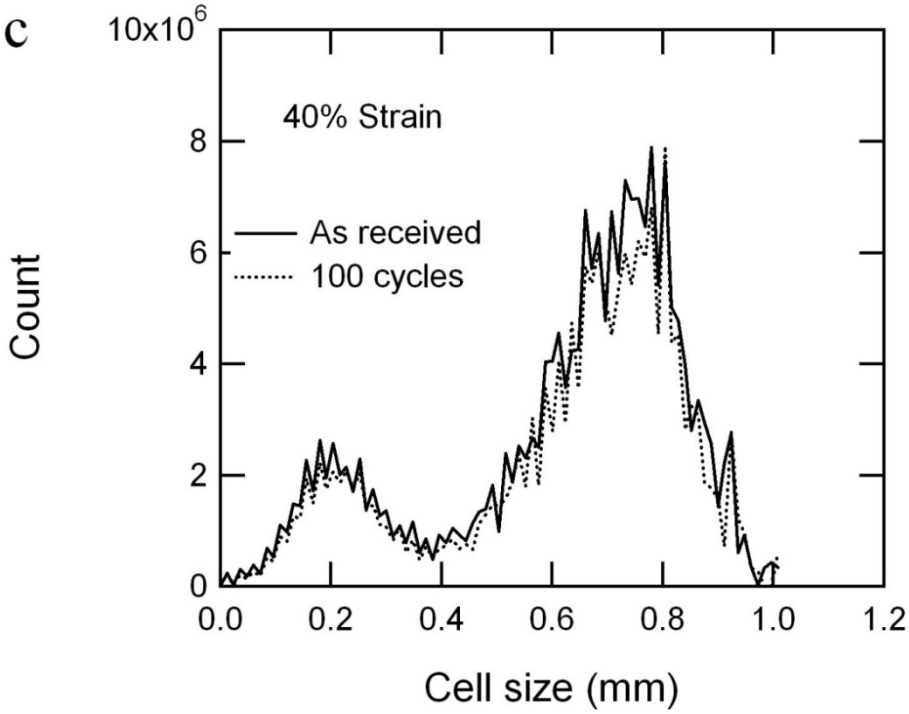

Figure 5.10 continued

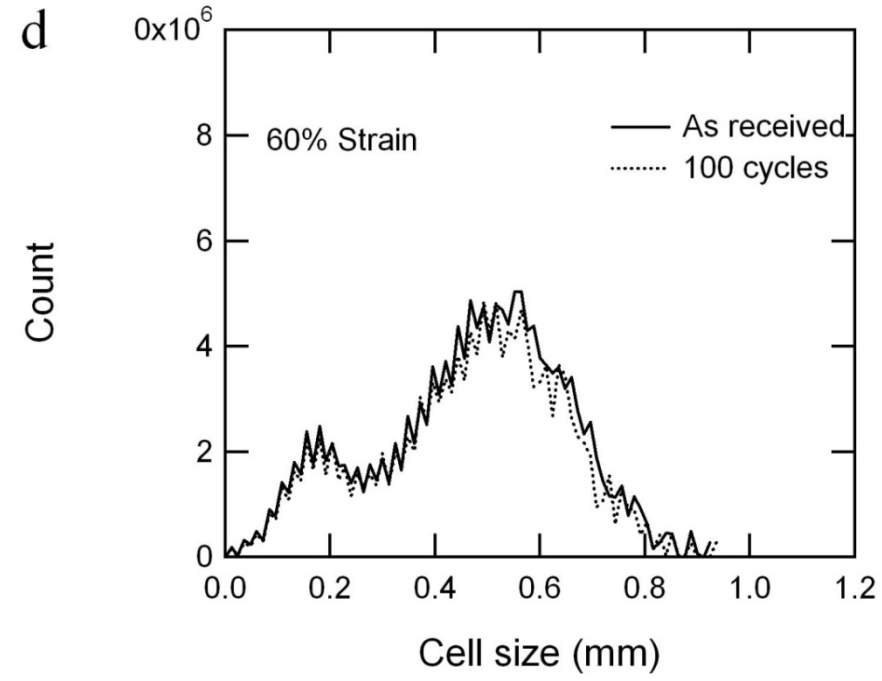

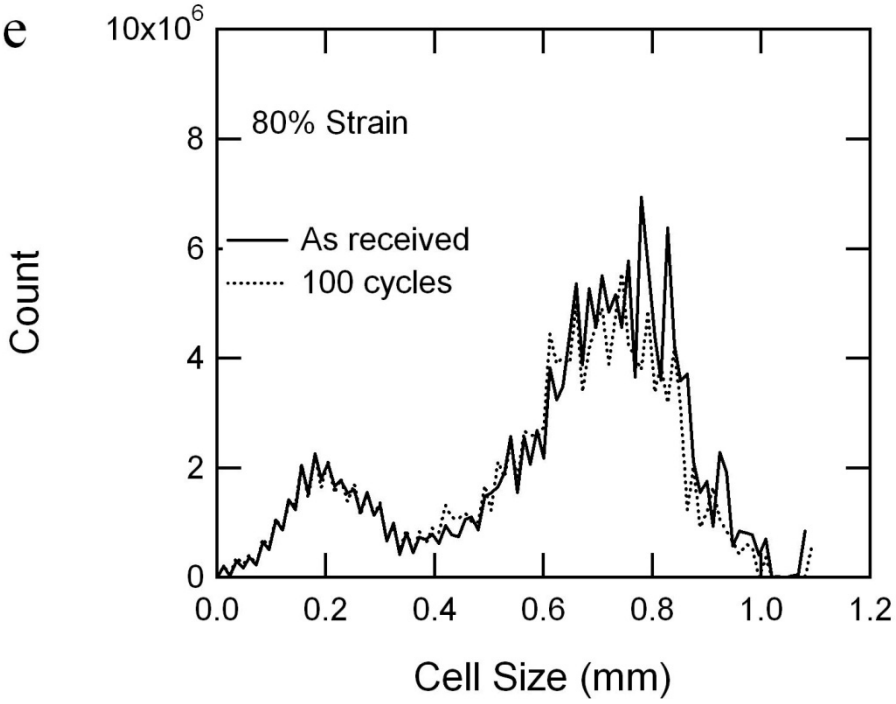

Figure 5.10 continued

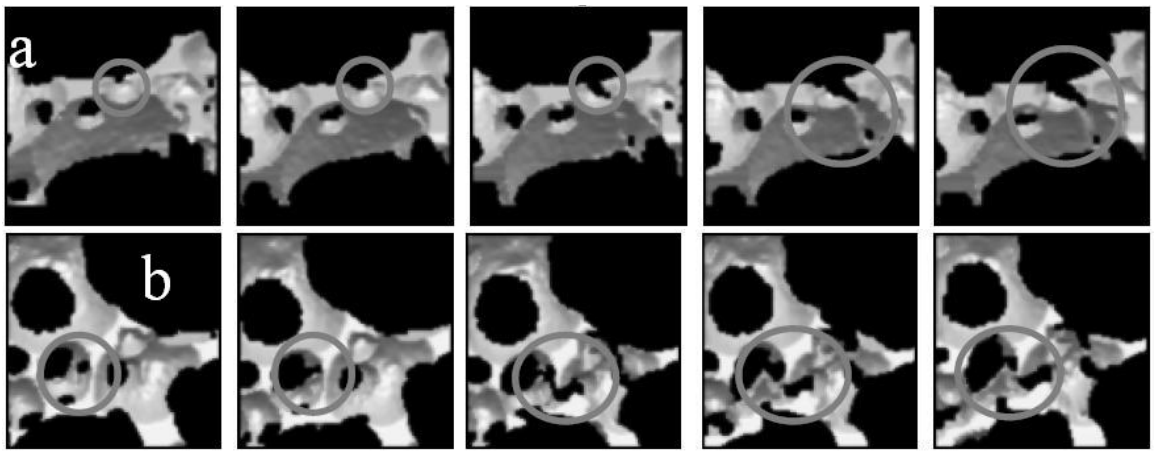

Figure 5.11: Examples of microfracturing of struts pre-macroscopic failure.
Both (a) and (b) track a strut over 100 cycles; as received the left most imagine and 100 cycles right most.

5.5 Discussion

Understanding the cyclic response, both mechanical and mesostructural, of epoxy SMP foams is critical for designing next generation materials and for use in engineering applications. This work has continued the study of cyclic behavior started by the authors in a previous work (M. A. Di Prima, et al., 2007). The prior work, Chapter 2, investigated the effect of deformation temperature on the cyclic response, and it was found that the there was a correlation between the strain-to-failure as a function of temperature and the cyclic damage accumulation. Specifically, as the deformation temperature approached that corresponding to the peak of the strain-to-failure behavior, there was significantly less cyclic damage. The strain to failure versus temperature for DP5.1 base polymer and 20% RD foam both peaked at 55°C, Chapter 3; to minimize this temperature effect the deformation temperature of $1.3T_g$ (T_g in °C) was selected. This allows the performance envelope of maximum compressive strain and relaxation times to be determined.

While not the primary focus of this work, the results of Figure 5.1 further emphasizes the importance of the packaging temperature on the behavior of SMP foam. The negligible effect on the free strain recovery allows the packaging temperature to be selected based on other criteria. Figure 5.1(a) illustrates the effect of packaging the material in the viscoelastic regime and the ability to tune both recovery force and onset temperature.

The cyclic results from prior work (M. A. Di Prima, et al., 2007) showed that cyclic deformation leads to degradation of mechanical properties under temperature and strain conditions that is not observed in monotonic deformation. This result was more extreme than the slight degradation observed in the literature (Tobushi, et al., 2004). This could be the result of the polymer chain not being able to fully recover to the equilibrium state before the next cycle starts (i.e. viscous lag from the unloading process). Thus a hold time was introduced between cycles in which the sample is totally unconstrained and is free to return to its equilibrium state. Based on the stress relaxation curve at 110°C, Figure 5.12, the three times were chosen to represent no relaxation (0 s), when the material relaxes to half way between initial stress and the stress plateau (40 s), and when the stress plateaus (300 s).

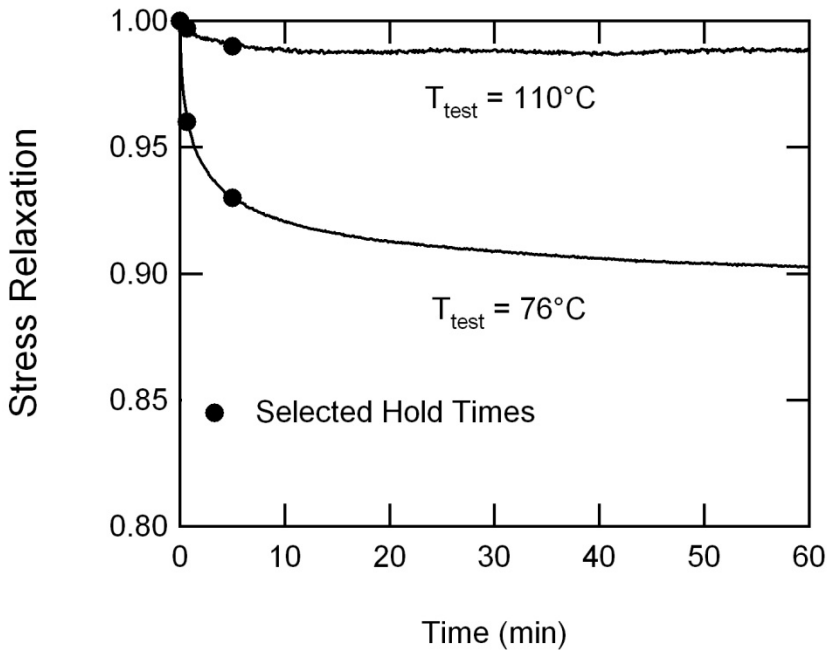

Figure 5.12: Stress relaxation of base polymer at 76°C and 110°C.
The base polymer was strained to 80% of failure strain for that temperature with the selected hold times shown for clarity.

For the 20% RD foam (Figure 5.3) there is a threshold in residual strain accumulation between maximum compressive strains of 60 and 80%. The change in the slope at 20 cycles for the 80% maximum compressive strain indicates the onset of macroscopic failure. The drop in maximum normalized stress has a threshold maximum compressive strain between 40 and 60% and it is harder to determine where macroscopic failure begins. Furthermore, the drop in maximum normalized stress leads the increase in residual strain for all compressive strains except 40%. The response of the 30% RD foam, shown in Figure 5.4, showed a similar threshold in between 40 and 50% compressive strain across both residual strain and normalized maximum stress. The drop in normalized stress, apparent in Figure 5.4(b), would indicate some sort of macroscopic failure and visual post-test inspection revealed a single fracture at the base of the sample. This was the only time such a fracture was observed and it is most likely due to a

structural defect that localized deformation. While the accumulation of residual strain slightly lags the drop in maximum normalized stress, the onset of macroscopic failure is much faster than in the 20% RD foam. The 40% RD material also showed the same damage threshold between 40 and 50% strain, observed for the 30% RD foam. However, the cycles to failure for the 40% RD foam were lower than that for the 30% RD foam. Still, the drop in maximum normalized stress corresponds to the enhanced accumulation of residual strain and macroscopic failure occurs just as quickly as in the 30% RD foam.

Figures 5.3-5.5 illustrate that relative density has an effect on both the cyclic failure envelope and the failure mechanism. FEA in an earlier work showed that for the 20% RD foams the bulk of the compressive strain is accommodated in the vertical struts, while in the 30 and 40% RD foams, the bulk of the compressive strain is accommodated in the joints, Chapter 4. This is a possible explanation for the gradual failure in the 20% RD foams and the sudden failure in the 30 and 40% RD foams. The shift of the compressive strain threshold is most likely a combination of the shift in pore volume in the foam as well as the aforementioned change in structural response.

Having set the performance boundaries in terms of temperature and applied strain, the effect of hold time on cyclic behavior can be isolated. Figures 5.6 and 5.7, indicate significant improvement with a hold time of 40 s (and associated stress relaxation) relative to the case with no hold period. However, a 300 s hold time showed reduced improvement relative to the case with no hold period. This is significant as 40 s appears to be the optimum hold time to reduce damage during cyclic deformation. This trend was

confirmed by both measures of damage; accumulation of residual strain in Figure 5.6(a) and drop of normalized maximum stress, shown in Figure 5.6b). The same optimum hold time of 40 s is again observed with the 30% RD foam, Figure 5.7. This optimum time must be the result of two competing mechanisms; one promoting damage recovery and one adding to the damage. None of the three samples with a hold time of 40 s failed in 100 compressive cycles, while two of the three samples with a hold time of 300 s failed in 100 compressive cycles and all three samples with no hold time failed in the 100 compressive cycles. The same trend is observed in the drop of the maximum normalized stress, which again slightly leads the accumulation of residual strain. The results for the 40% RD foam showed that neither accumulation of residual strain shown in Figure 5.8(a) nor drop in maximum normalized stress in Figure 5.8(b) changed with increasing hold time. This indicating that for 40% RD foam the maximum engineering strain of 50% exceeds a strain threshold where the observed hold times influence damage accumulation.

ANOVA of the cycle to failure results tests the hypothesis that the means come from a statistically similar set of data. The p-value reflects the degree of statistical similitude; a p-value of 1 indicates that there is no variation (i.e no effect of hold time) within the results, while a p-value of less than 0.05 indicates that the hold time has a significant effect on the cycles to failure. For the 20% RD foam the p-value of 0.142 indicates that the hold time has some effect on the results there is still significant overlap in the cycles to failure as a function of hold time. This is probably due to the inherent complexity of cyclic failure combined with the mesostructure of the foam. For the 30% RD foam the p-value of 0.0715 indicates that the hold is having a greater effect on cycles to failure but

there is still overlap in the data. For the 40% RD foam the p-value of 0.734 indicates that there is no effect of hold time on the cycles to failure.

The global response for 17% RD foam with a hold time of 40 s was captured at three different compressive strains (40, 60, and 80%). None of the samples experienced macroscopic failure, so only the pre-fracture behavior was captured. The average strut thickness, shown in Figure 5.10(a), and average cell size, in Figure 5.10(b), were independent of the number of cycles in the pre-failure region. This lack of evolution of the cell size is further confirmed when the as-received cell size distribution is compared to the cell size distribution after 100 compressive cycles. There is no noticeable shift in the distributions for either 40%, (Figure 5.10(c)), 60%, (Figure 5.10(d)), or 80%, (Figure 5.10(e)), compressive strains. This does not explain the difference in behavior between the responses in Figures 5.3(a) and 5.3(b) for the 60% compressed sample, so two local regions in 80% compressed material were tracked across the 12 micro-CT scans. These local regions show formation of localized micro-damage forming without disruption of the surrounding structure. This is consistent with the lack of global damage from the quantitative analysis and can explain why the maximum normalized stress drop precedes the accumulation of residual strain. These microfractures would reduce the force necessary to compress the samples without adding to the residual strain until the microfractures propagate and macro-failure occurs.

5.6 Conclusions

1. The packing temperature has negligible effect on the free strain recovery of the

material but has a significant effect on the constrained stress recovery.

2. The maximum strain is a driving factor in the cyclic behavior of epoxy SMP foams across relative densities and there is definitely a strain threshold for damage.
3. The residual strain damage indicator lags behind the normalized maximum stress damage indicator.
4. A hold time of intermediate length, 40 s, can substantially increase the cycle life span of the material within a certain strain and RD range.
5. There is no significant effect on the global structure or response by virtue of cyclic compression below the strain damage threshold.
6. Microdamage accumulates on the struts under conditions that don't lead to global failure or damage after 100 cycles.

CHAPTER 6: CONCLUSIONS

6.1 Introduction

This work has set out to address the lack of understanding of the core behaviors of SMP foams. These behaviors spanned performance envelopes, temperature and strain effects, structure-property relationships, and local structural responses. Chapter 1 provided the requisite background information on the various concepts and behaviors addressed in this work. Chapter 2 presented an introduction to the thermomechanical behavior of epoxy SMP foam and with a focus on the temperature dependent behaviors. Chapter 3 introduced different relative densities of foam (structure parameter) and tracked the effect through compression, cooling, and shape recovery. The compressive behavior was found to follow a constitutive relation proposed by Gibson and Ashby (Gibson and Ashby, 1997) once the compressibility modifier term was made to be a function of temperature. Chapter 4 continued the investigation of the effect of structure by focusing on local strain responses determined through FE simulations. The sample and batch variability was determined to insure that simulation and experimental results were representative of all materials with the same relative density. Chapter 5 addressed the cyclic response of SMP foams as a function of structure and maximum strain. Hold times were introduced to allow for viscous relaxation between compressive cycles and micro-CT scans were used to track the evolution of local micro-damage. Across these chapters, the core thermomechanical and structural behavior of SMP foams were addressed.

6.2 Fundamental Advances

In addressing the core thermomechanical and structural behavior, a series of fundamental advances were made with the understanding of SMP foams. The first advances were in determining the temperature dependent behaviors. The temperature dependent tensile strain to failure behavior seen in SMPs was confirmed to be present in the foams, Chapters 2 and 3. This behavior is also partly responsible for the temperature dependency in monotonic strain recovery (where at higher temperatures strain recovery decreases) and the dependency on cyclic damage accumulation (where more damage accumulates at higher temperatures). The compressibility, strain at which the foam can be considered fully dense, also had a temperature dependency as seen in Chapter 2 and utilized in Chapter 3. The packaging temperature also had a significant effect on the recovery behavior; the constrained stress recovery had the largest effect, while free strain recovery showed less of a temperature dependency in the investigated foams.

The next advancement was determining how the maximum strain affected material response, and even how much of an interplay there was between maximum strain and temperature. Through the block compression testing in Chapter 2, there is a threshold of maximum strain (and temperature) where the material ceases being able to recover. This same threshold carries over into the cyclic response; Chapters 2 and 5 both show increasing damage accumulation with increasing maximum strain. Chapter 5 shows that the maximum strain threshold for microdamage is lower than the strain threshold governing accumulation of residual strain. The local strain distribution from FE

simulations, Chapter 4, shows that the maximum local strain is a function of the applied compressive strain; tying the local damage back to the maximum applied strain.

The most fundamental advancement made in this work was the inclusion of structure-property relationship. No other work to date on SMP foams has included this analysis. The structure of the foam was varied by changing the relative density; with the resultant structural changes observed through micro-CT scanning. Relative density did not significantly impact the T_g (with the exception of the first foam, which was a processing issue) or free strain recovery behavior. While the tensile strain to failure analysis only compared a single foam to the base polymer; strain to failure results were divergent at low temperatures, while the failure strains for both foam and polymer peaked at the same temperature and strain and were similar for higher temperatures. Confirming predictions from Gibson and Ashby (Gibson and Ashby, 1997) stiffness of the foams followed the expected trends as a function of relative density. The cyclic compression response was also dependent on relative density; the 20% RD material showed gradual damage accumulation and could with stand larger maximum strains. The 30% and 40% RD material showed very sharp damage responses after an induction period where there was little damage accumulation and could not with stand the same strains as the 20% RD material. Local deformation also varied with relative density; the 20% RD material primarily deformed along struts aligned with applied strain while the 30% and 40% RD materials primarily deformed at cell joints.

The last advances were modeling related; the first was making the compressibility modifier from the Gibson and Ashby model for elastic open cell foams to be dependent on temperature. This allowed for a significant improvement in matching experimental data over a range of temperatures. The final advancement was the analysis of the cumulative strain distribution from the FEM simulation and fitting to a probability distribution.

6.3 Practical Applications

This work can be applied either to the performance/environmental conditions of existing SMP foam or it can be used to more intelligently design foams for specific applications. The understanding of temperature and strain limitations of these specific foams, based on CTD DP5.1 polymer, can be used in determining if this material is capable of performing under the required conditions (i.e those seen by a morphing wing or embolic sponge). In application where there is some environmental control, the optimum temperature can be selected to minimize cyclic damage as well as maximize strain to failure. If possible, allowing short pauses between the cyclic compressions will extend the life of the material if the maximum strain is near the boundary of the foam. Furthermore, new foams (either different relative density or base polymer) can be designed with a better understanding of the end properties and behavior.

Confirming the relationship between the modulus of the base polymer and the foam across a range of temperatures as a function of relative density allows either the relative density or the base polymer to be picked to hit a target stiffness at a specific temperature.

The improved constitutive model allows a specific stress/strain response to be selected by again picking the relative density and base polymer. Also knowing that the relative density effects the mechanical degradation under cyclic conditions can further dictate the foam design. In general, with a better understanding which properties and how they are affected by the relative density allows for a better designed SMP foam for specific applications.

6.4 Future Directions

While this work has addressed and developed a better understanding of the core thermomechanical and structural behavior of SMP foams, there is still more that can be done. This work observed some of the complex viscoelastic behavior during the packaging process, but more can be done to character base material response and how relative density effects viscoelastic behavior (relaxation, creep). Specifically, modeling how the packaging temperature drives the difference in constrained stress behavior would be valuable. Appendix C touches on the ratio of mechanical energy needed to package the material and how much mechanical energy can be recovered. The results showed that entropy change was a greater factor than the packaging mechanical energy, a factor that would be further illuminated by a better understanding of the viscoelastic behavior of the polymer and foam. This could also lead to a better understanding of how a hold time of 40 s minimizes the cyclic degradation of mechanical properties which could not be fully explained in Chapter 5.

As finite modeling and the resultant strain analysis has proved to be an invaluable tool in understanding local deformation behavior of SMP foam, there is room for optimization

and improvements in the simulation. Due to computational and coding constraints, the simulations only ran to strains that were in the initial plateau region, but it would be more useful to be able to run the simulation into the densification regime. Furthermore, while the meshes used in the simulations were considered RVEs it would be useful to run larger meshes. The constitutive material model used for FEM neglected viscoelastic behavior, which would be a more dominant behavior at lower temperatures and improve overall simulation accuracy.

Micro-CT scanning has proved to be an invaluable tool in characterizing foam structure, capturing local deformation, and observing localized micro-damage. As such, this technique could be used to further tie structural qualities directly to differences in foam processing. This would allow for better foam design, and could ultimately remove the general relative density term and replace it with a more structurally relevant term. This sort of characterization combined with a strenuous thermo-mechanical test regimen would further enhance the structure-property relationship.

The last direction of interest stemming from this work is determining the mysterious shift in T_g of the foams found in Appendix A. This shift, if time dependent, would have a significant effect on the materials performance and impede the ability to intelligently design new foams. If the shift was due to an unknown environmental effect; it needs to be indentified and the mechanism investigated to insure the behavior can be account for in material models and by material designers.

6.5 Conclusion

This work set out to further the understanding of the thermomechanical and microstructural behavior of epoxy SMP foams. In achieving this goal, the temperature, strain, and structural effects on a variety of behaviors were determined. Constitutive models were validated and adjusted to fit this class of materials and the complex cyclic behavior was investigated. Lastly, the fundamental advances of the work, practical applications, and future directions for SMP foam research were discussed. With this complete, applications like morphing wings and embolic sponges will be able to take advantage of the unique blend of properties found in SMP foams.

APPENDIX A: Determing T_g

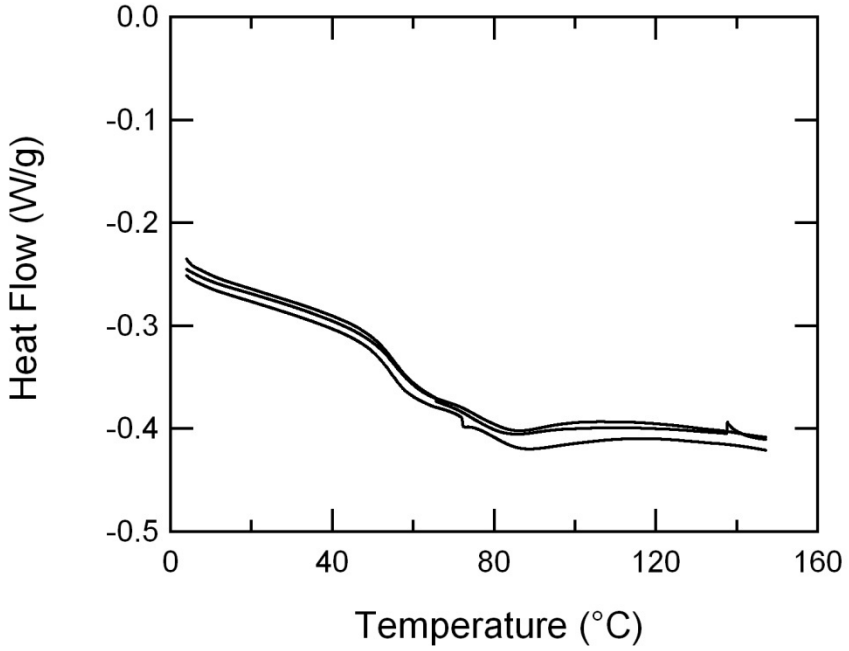

Figure A.1: DSC of TEMBO 3XE foam.

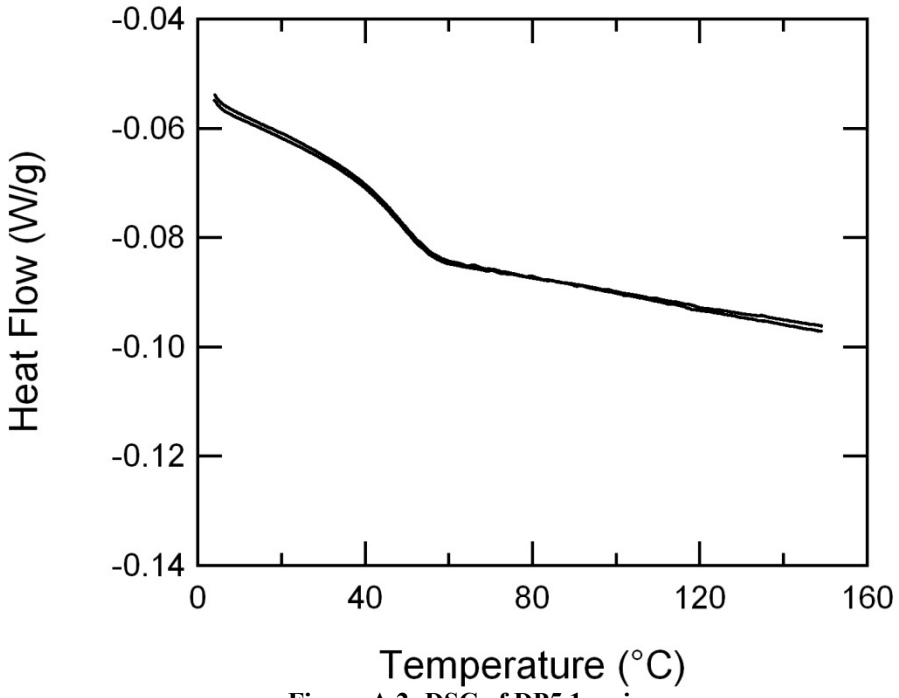

Figure A.2: DSC of DP5.1 resin.

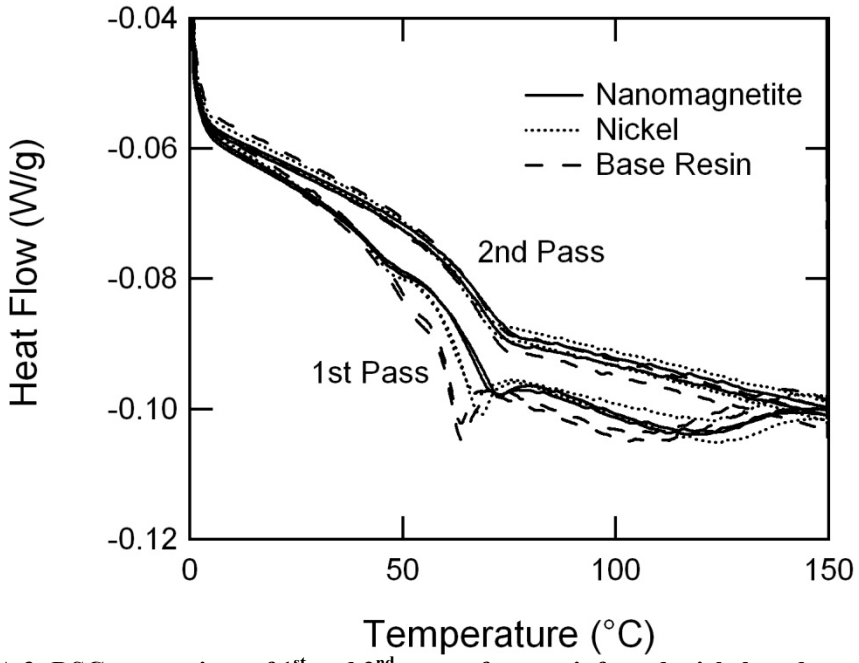

Figure A.3: DSC comparison of 1st and 2nd passes for unreinforced, nickel, and nanomagnetite reinforced DP5.1.

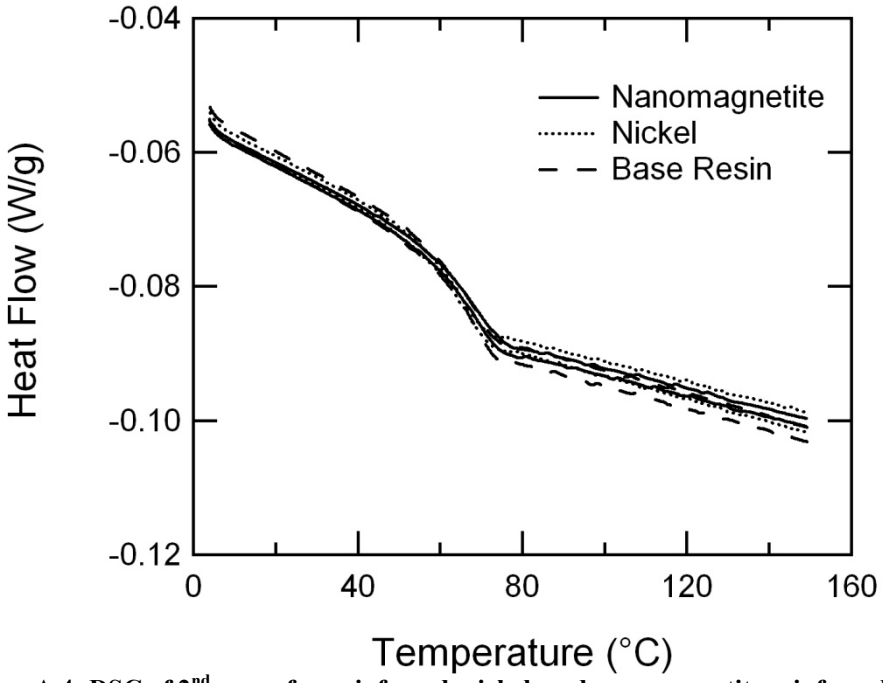

Figure A.4: DSC of 2nd pass of unreinforced, nickel, and nanomagnetite reinforced DP5.1.

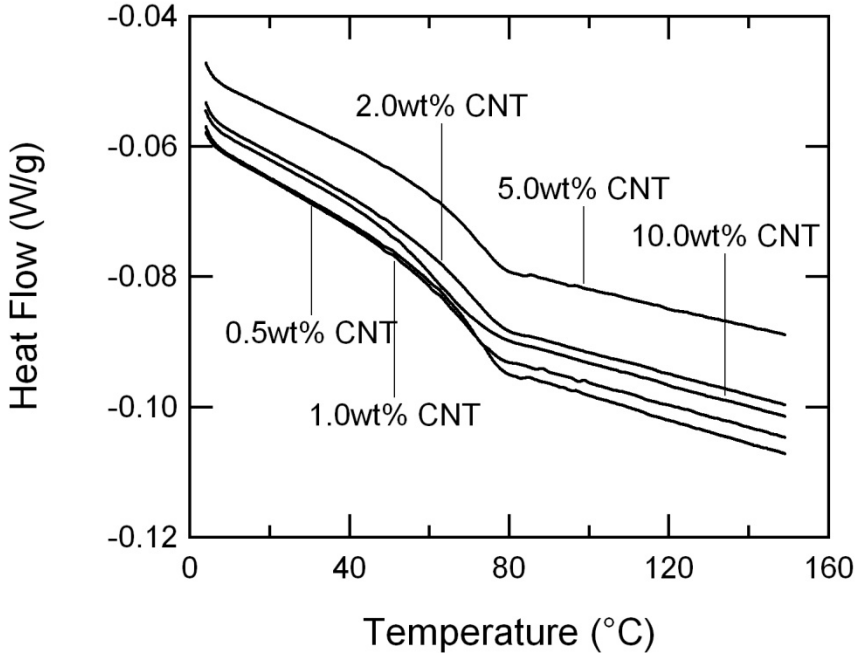

Figure A.5: DSC of DP5.1 reinforced with 0.5, 1.0, 2.0, 5.0, and 10.0 wt% multi-walled carbon nanotubes (CNT).

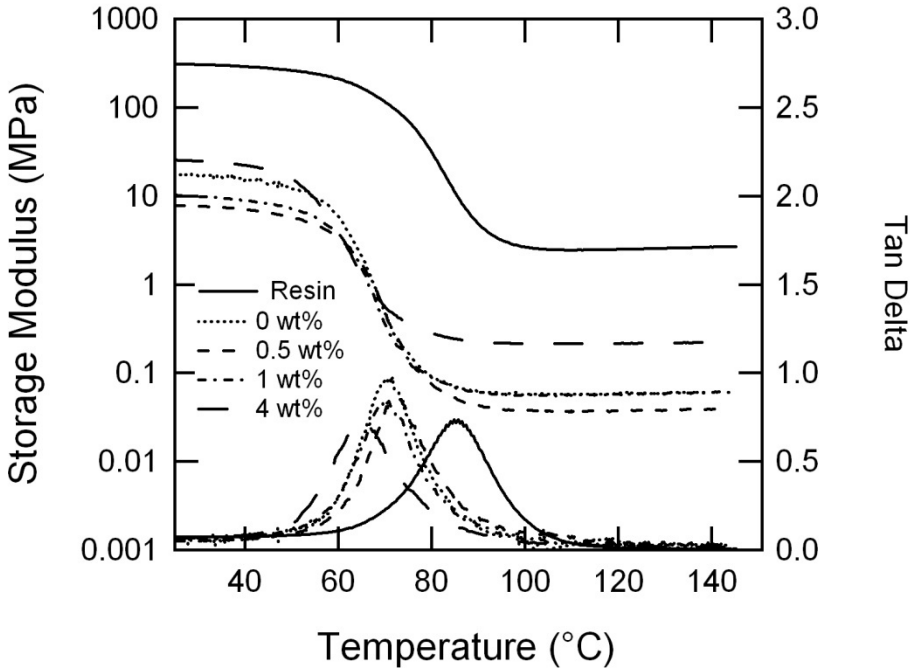

Figure A.6: Effect of Nanomagnetite reinforcement in DP5.1 foams on T_g and modulus.

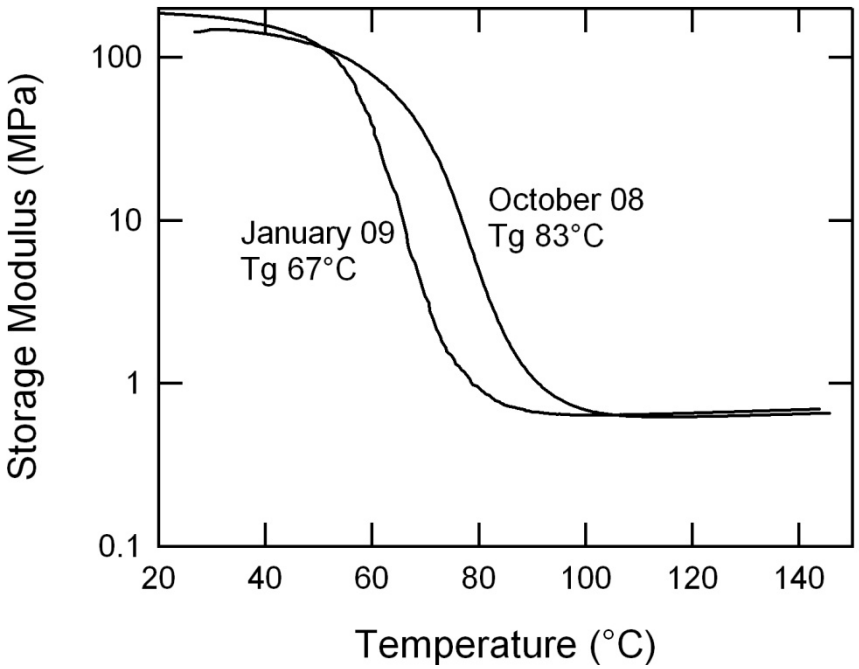

Figure A.7: Effect of time on the T_g of DP5.1 foam.
A 30% RD foam was used to illustrate this effect, which was uniform across samples.

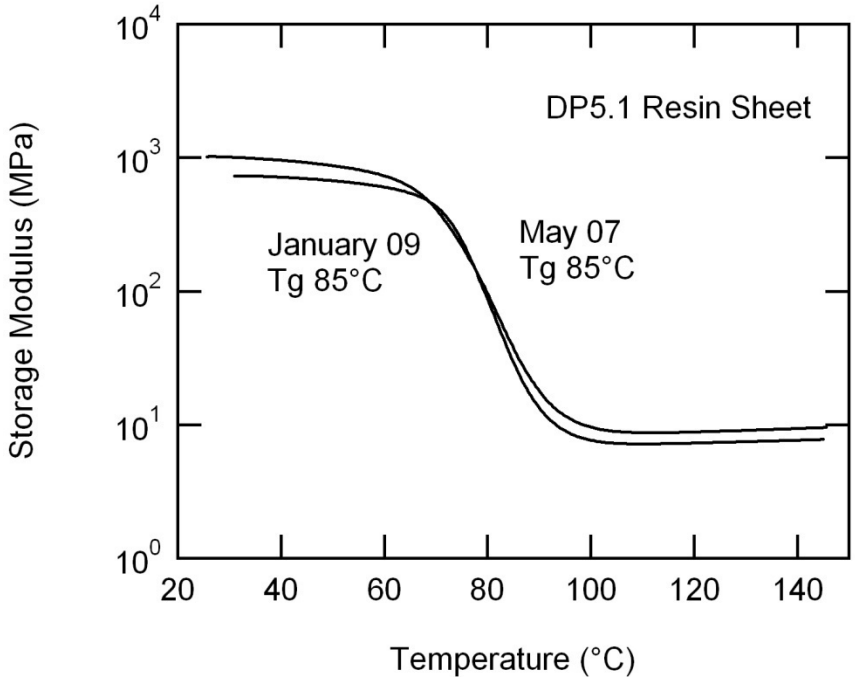

Figure A.8: Effect of time on the T_g of DP5.1 resin.
Unlike the foam, no time induced change of Tg was observed. This indicates that this effect is not inherent to the base polymer.

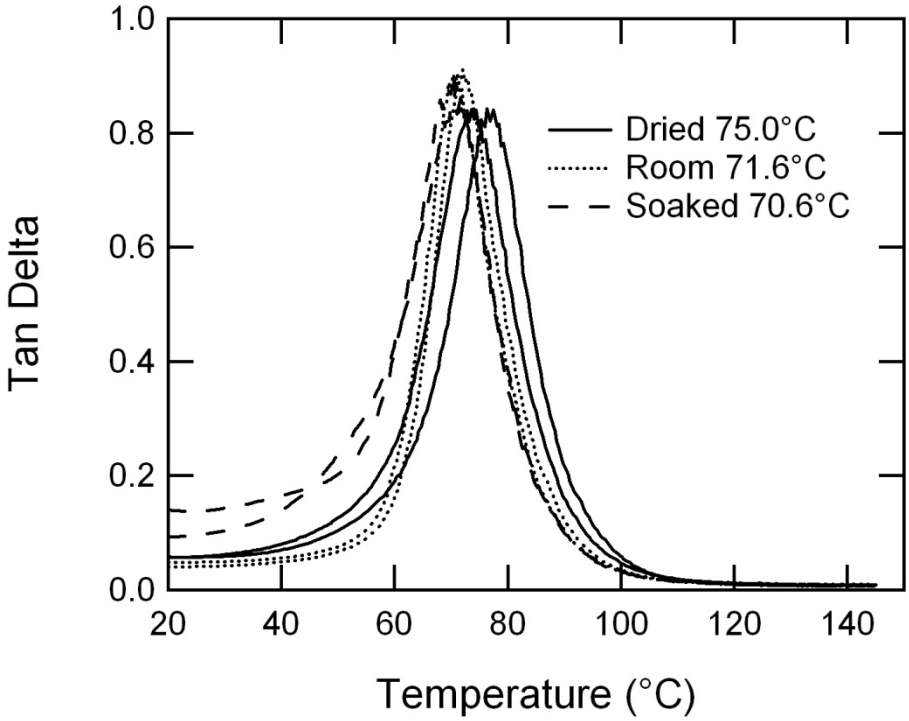

Figure A.9: Effect of humidity on the T_g of DP5.1 foam.

A 30% RD foam sample was used to illustrate the effect of humidity on the Tg in an attempt to explain the difference between A.7 and A.8. The two dried samples were dried in a vacuum oven at 100°C for 5 hours, soaked samples were soaked in water at room temperature for 36 hours and the pat dried before tests, and room samples were left out in the lab prior to testing.

APPENDIX B: Reinforced Foam

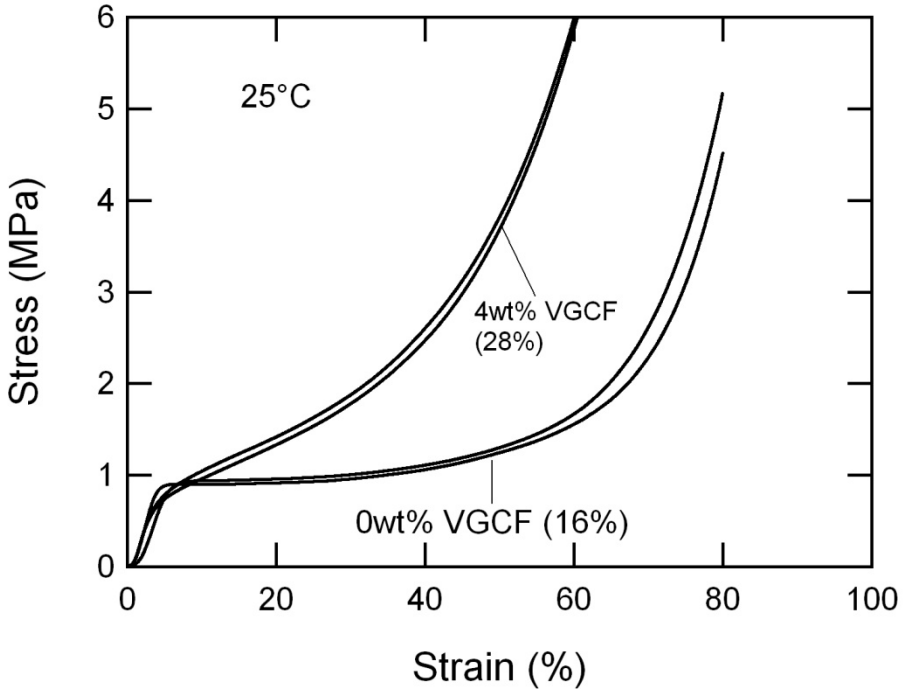

Figure B.1: Comparison of 4wt% and 0wt% VGCF reinforced foam at 25°C.

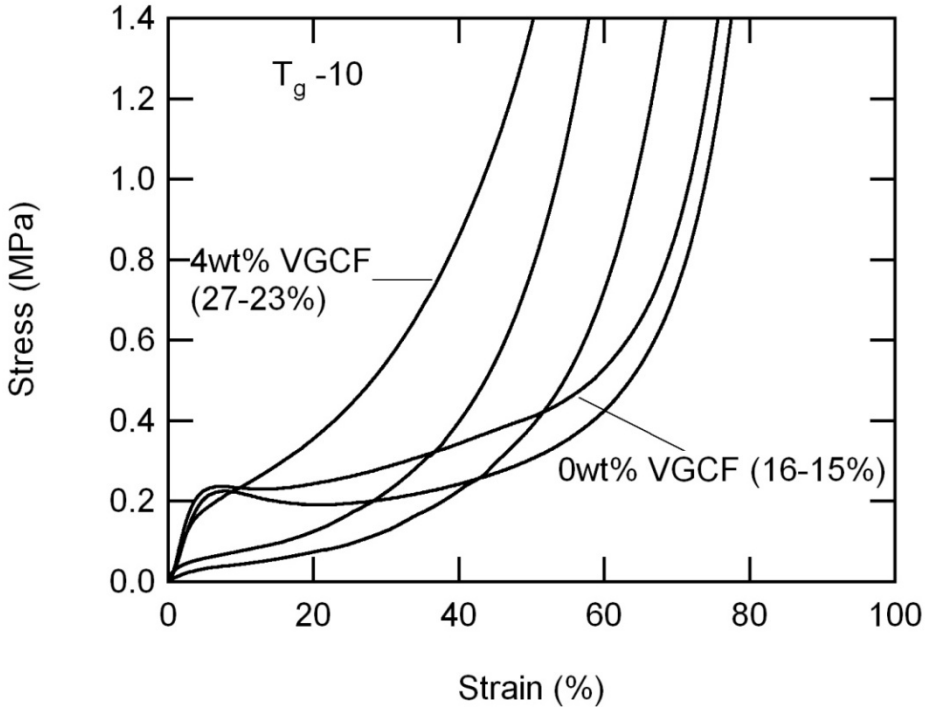

Figure B.2: Comparison of 4wt% and 0wt% VGCF reinforced foam at T_g - 10°C.

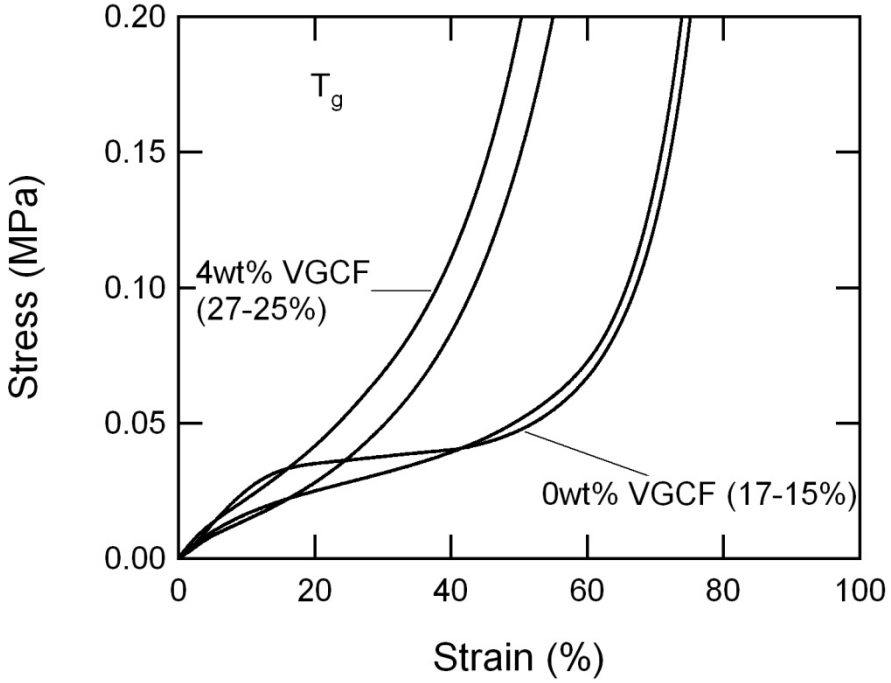

Figure B.3: Comparison of 4wt% and 0wt% VGCF reinforced foam at T_g.

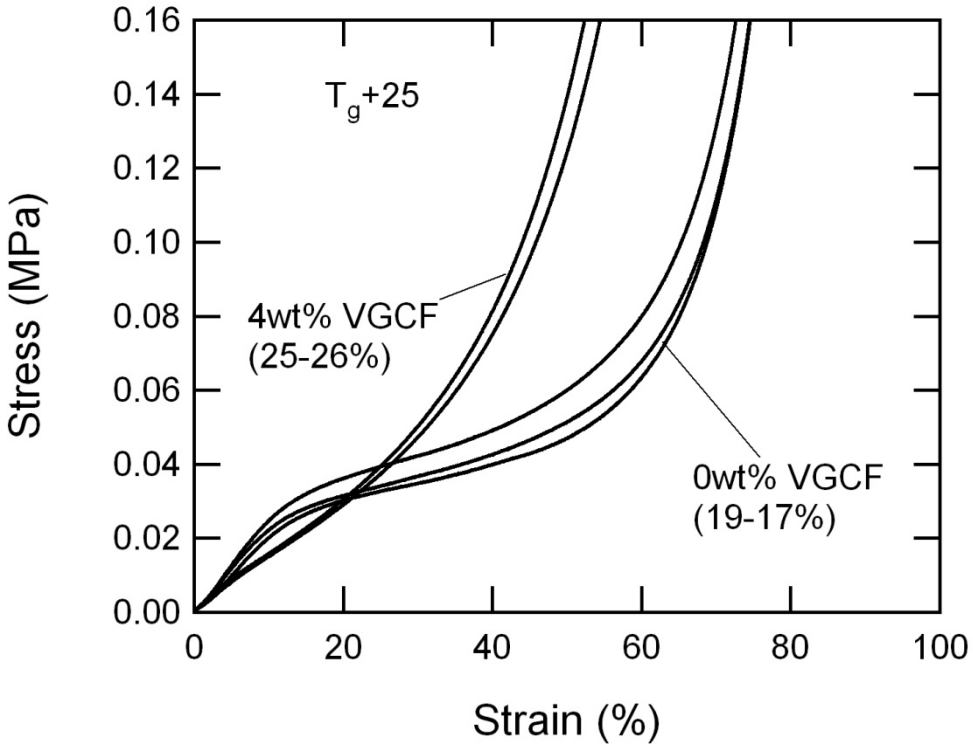

Figure B.4: Comparison of 4wt% and 0wt% VGCF reinforced foam at T_g + 25°C.

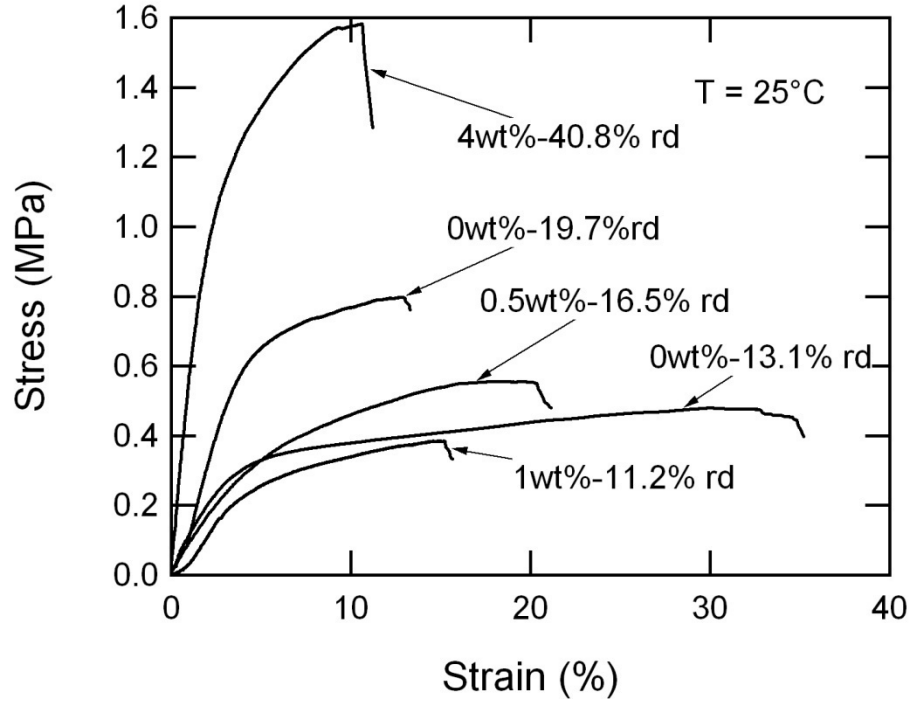

Figure B.5: Comparison of tensile response at 25°C for VGCF reinforced DP5.1 foam.

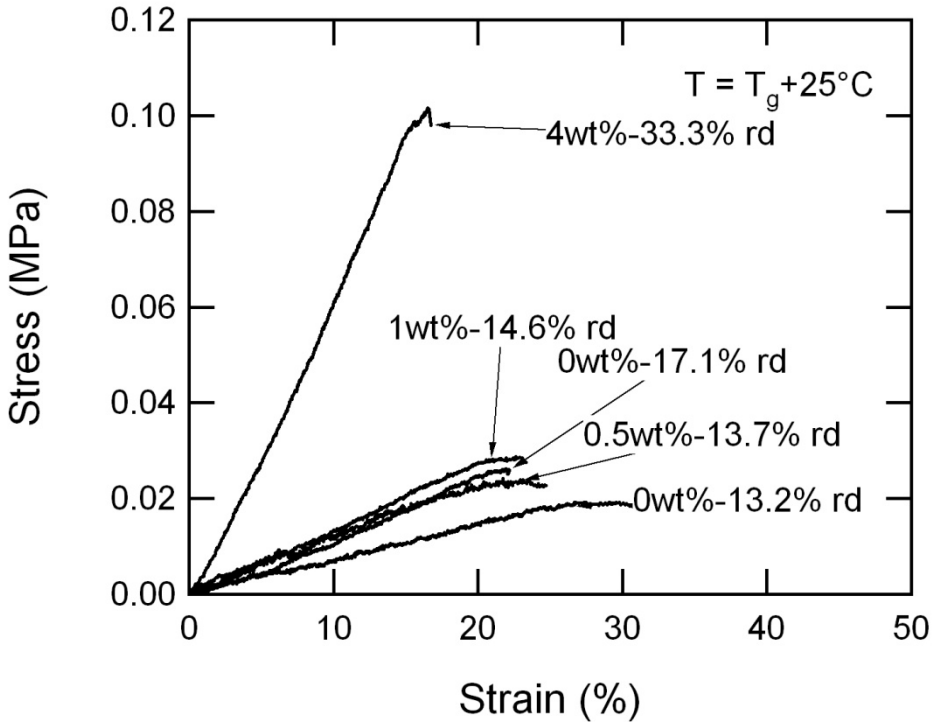

Figure B.6: Comparison of tensile response at T_g + 25°C for VGCF reinforced DP5.1 foam.

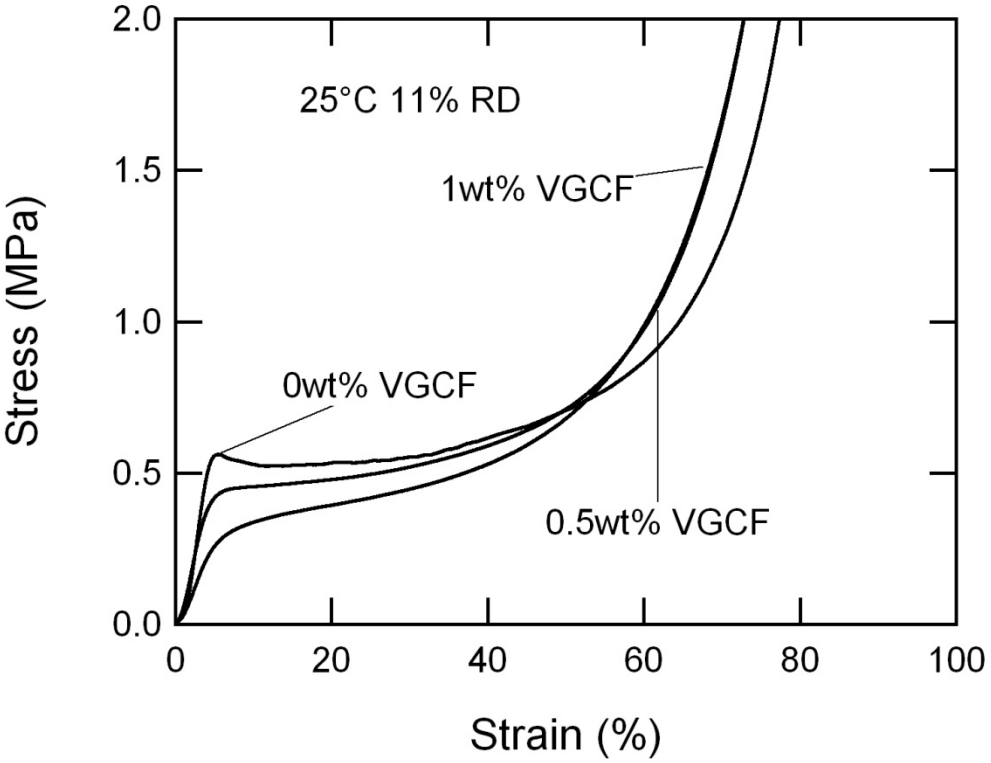

Figure B.7: Comparison of 11% RD VGCF reinforced DP5.1 foam DP5.1 at 25°C.

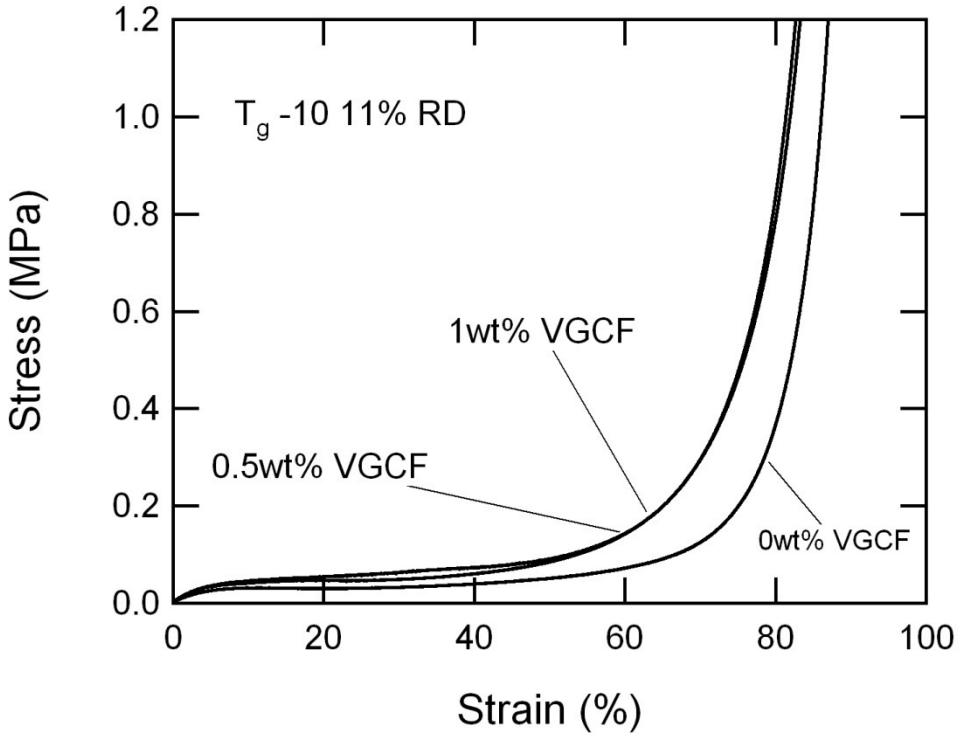

Figure B.8 Comparison of 11% RD VGCF reinforced DP5.1 foam DP5.1 at T_g - 10°C.

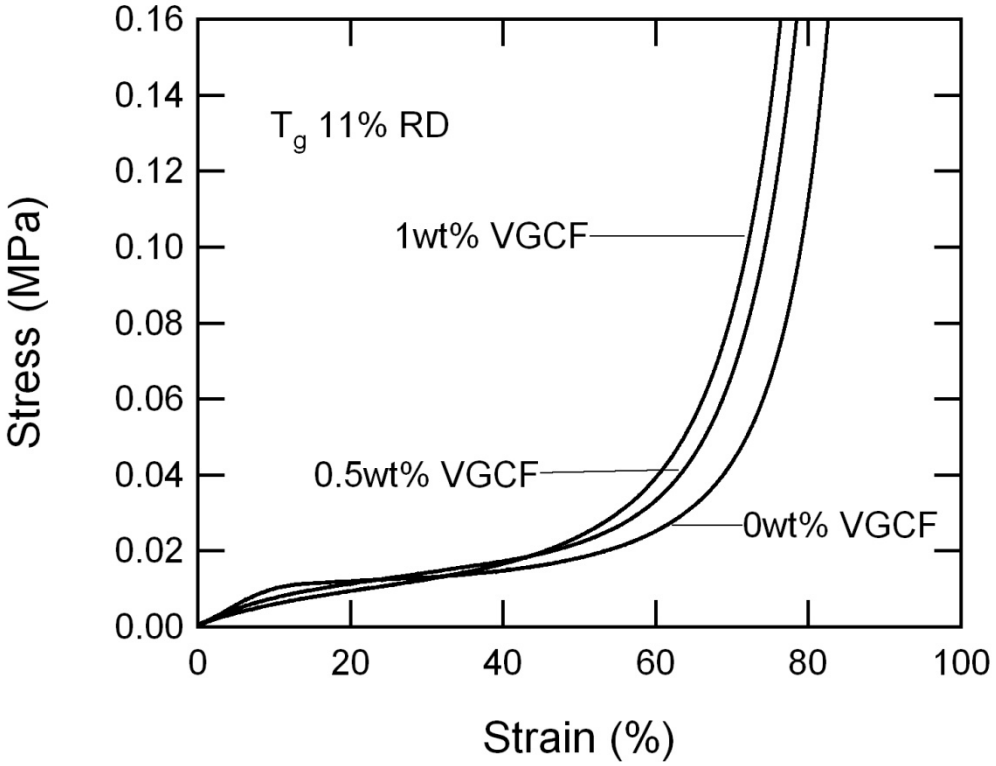

Figure B.9: Comparison of 11% RD VGCF reinforced DP5.1 foam DP5.1 at T_g.

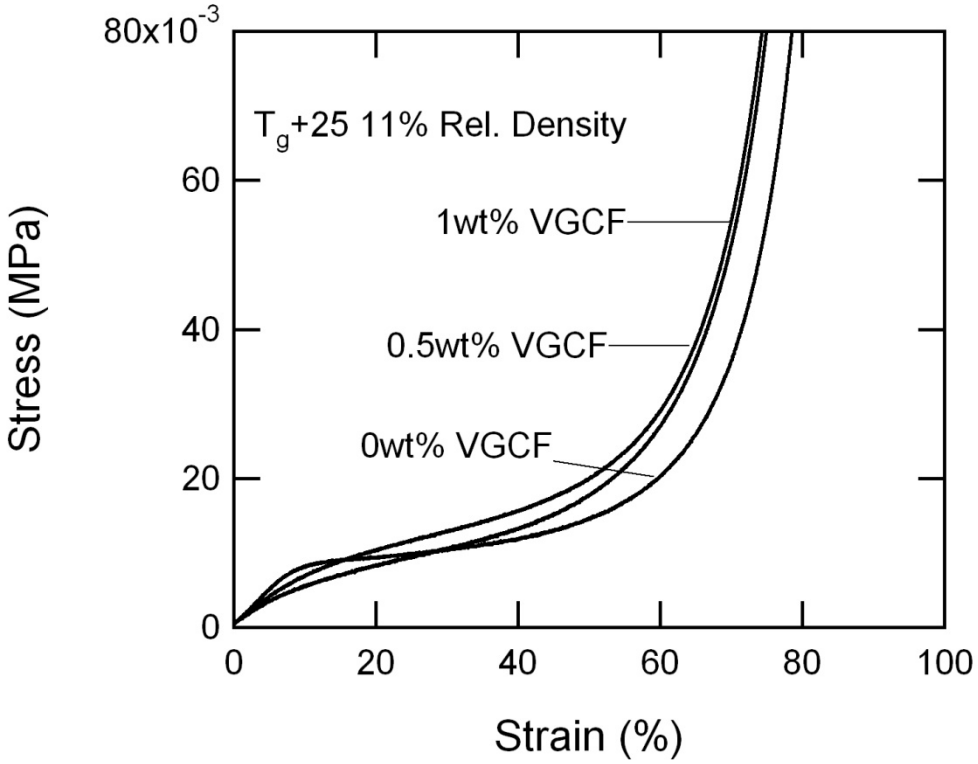

Figure B.10: Comparison of 11% RD VGCF reinforced DP5.1 foam DP5.1 at T_g + 25°C.

APPENDIX C: Mechanical Efficiency

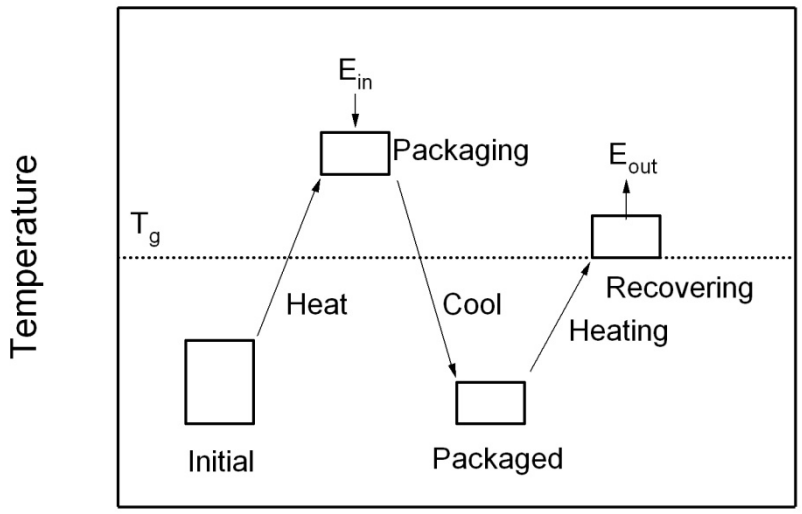

Figure C.1: Schematic of Mechanical efficiency.

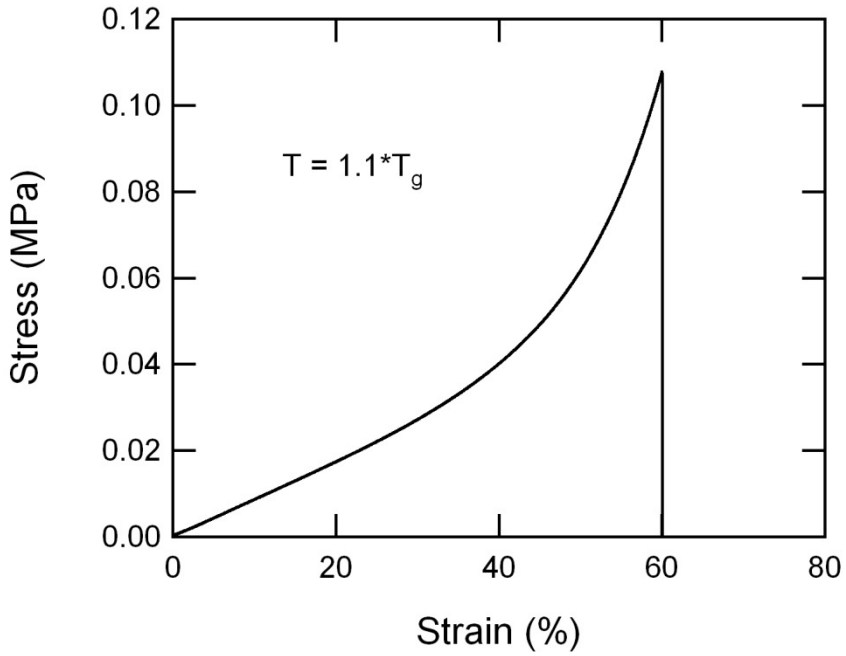

Figure C.2: Packaging response for DP5.1 20% RD foam at 1.1*T_g.

The mechanical energy in is calculated be taking the integral of the curve, performed using the trapezoidal rule.

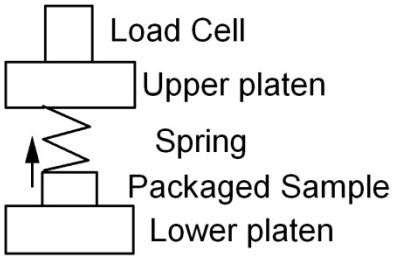

Figure C.3: Schematic of observing output of mechanical energy.
This setup is superior to the constrained stress recovery set up as work can be directly calculated. Once the spring is characterized, the force on the load cell correlates to a displacement of the spring. This displacement along with the force read on the load cell gives the mechanical energy the packaged sample is exerting.

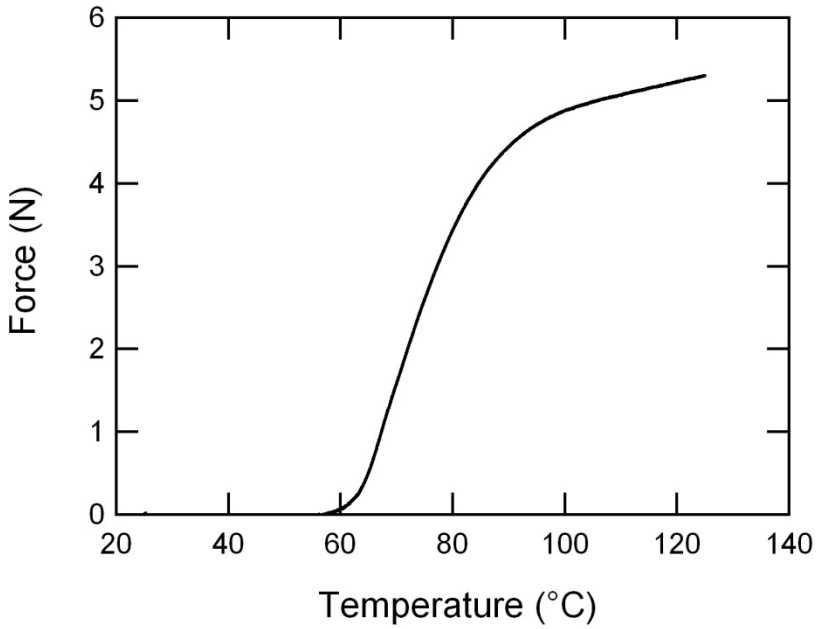

Figure C.4: Energy recovered response for DP5.1 20% RD foam.
This plot leads to knowing the mechanical energy the packaged sample is releasing at each temperature as the spring constant of the spring is known. For improved accuracy the effect of thermal expansion is removed for the calucations (this curve is recalculated so the force plateaus).

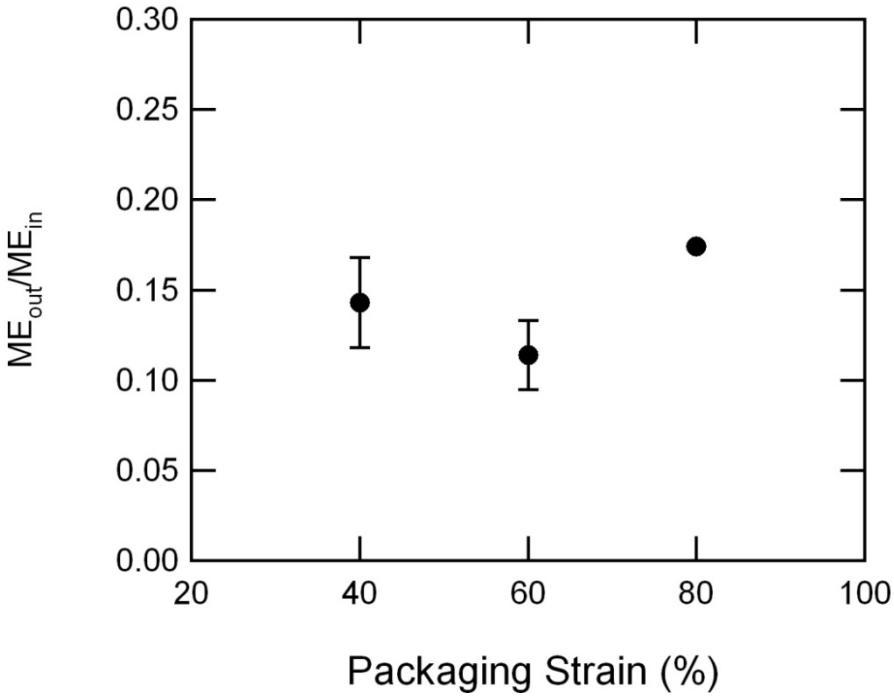

Figure C.5: Mechanical energy efficiency as a function of packaging strain.
The samples were 20% RD and packaged at T_g. Two samples were run under each condition, the second run for the 80% strain sample was excluded as an extreme outlier. Even with this small sample size, the packaging strain doesn't seem to exert a significant effect on the mechanical efficiency.

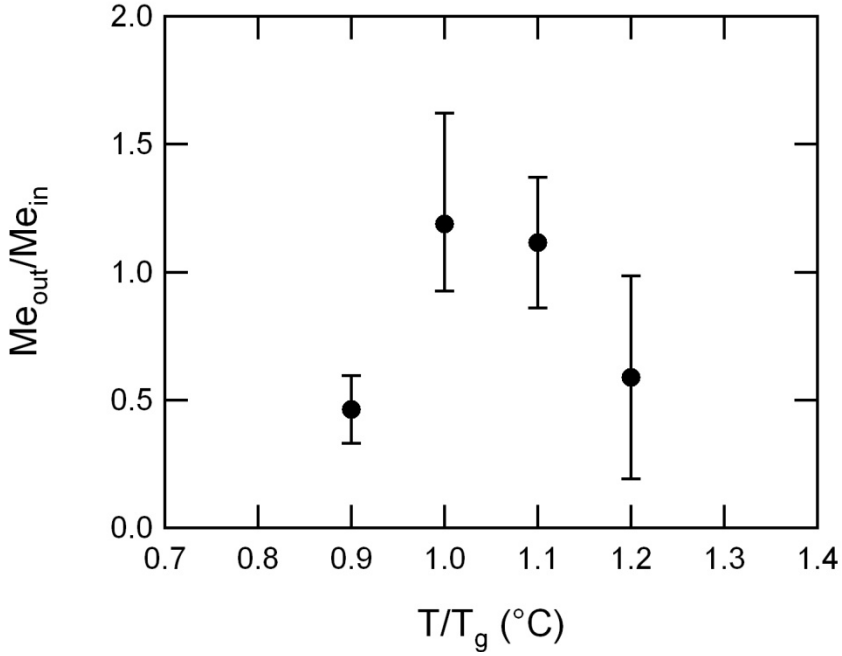

Figure C.6: Mechanical energy efficiency as a function of packaging temperature.
The samples were 20%RD and packaged to an engineering strain of 60%. Three samples were run under each condition. From ANOVA, a p-value of 0.23 indicates that packaging temperature does not significantly alter the mechanical energy efficiency. Since the packaging strain is the same, the entropy is the driving force for mechanical efficiency.

APPENDIX D: Micro-CT Scans

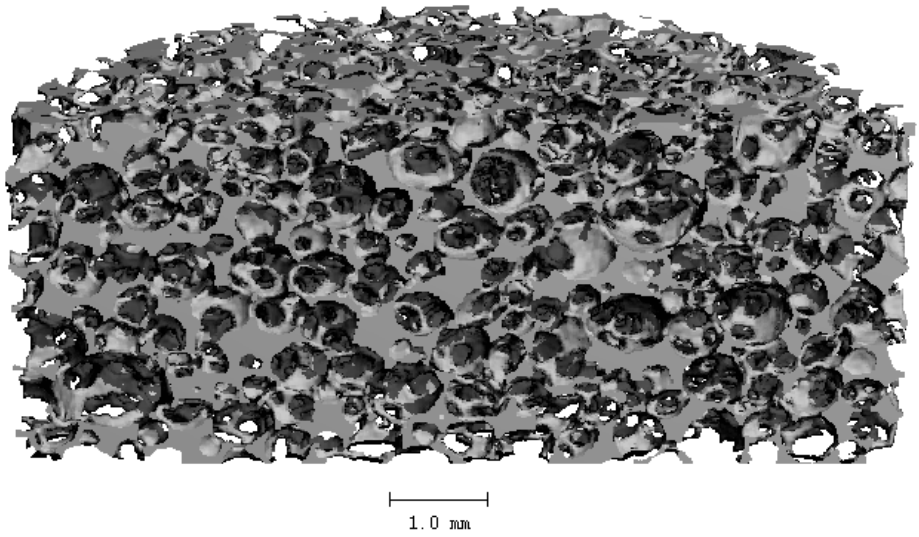

Figure D.1: As received TEMBO 3XE.

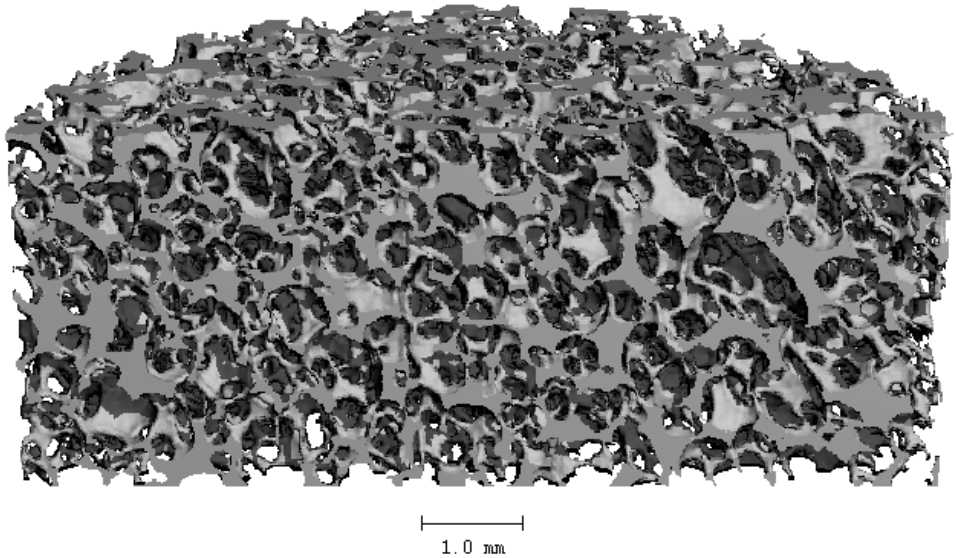

Figure D.2: 15% compressed TEMBO 3XE at 25°C

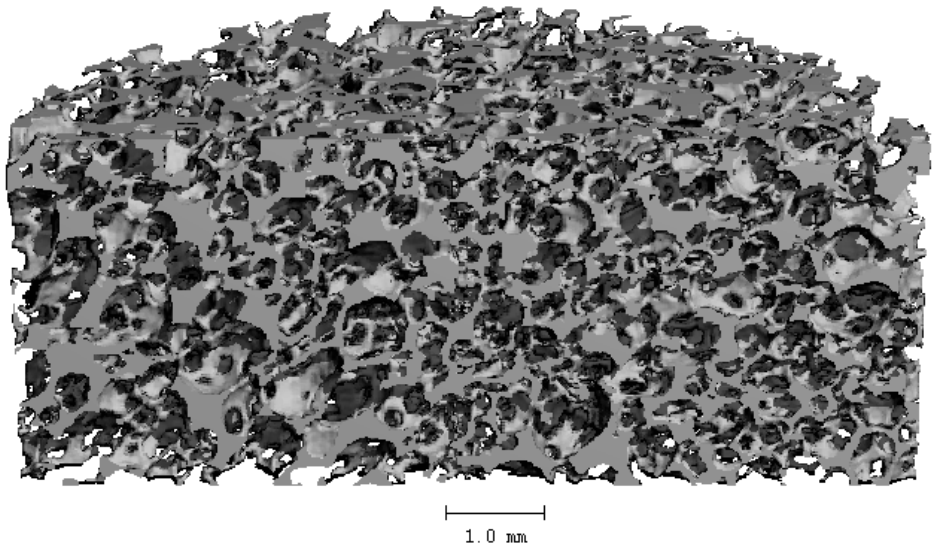

Figure D.3: 30% compressed TEMBO 3XE at 25°C

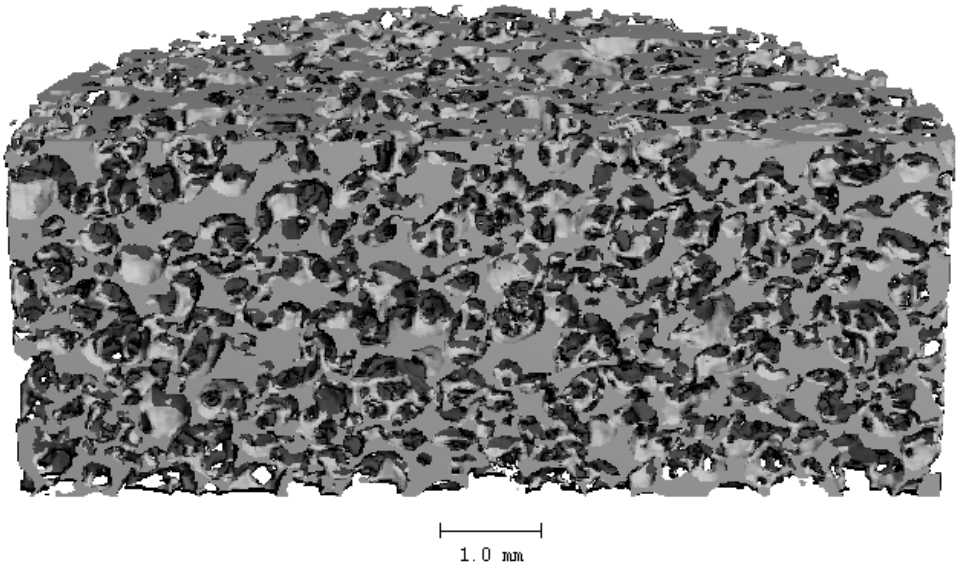

Figure D.4: 45% compressed TEMBO 3XE at 25°C

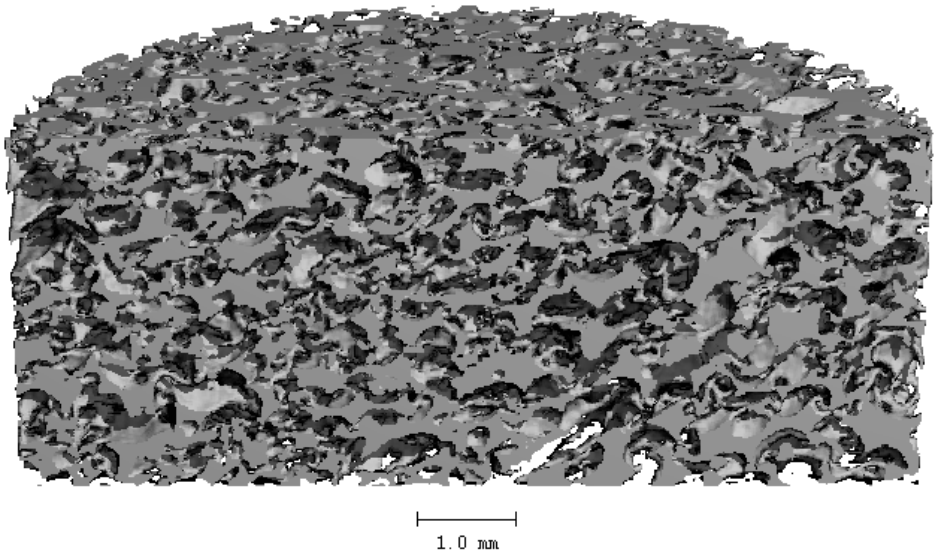

Figure D.5: 60% compressed TEMBO 3XE at 25°C

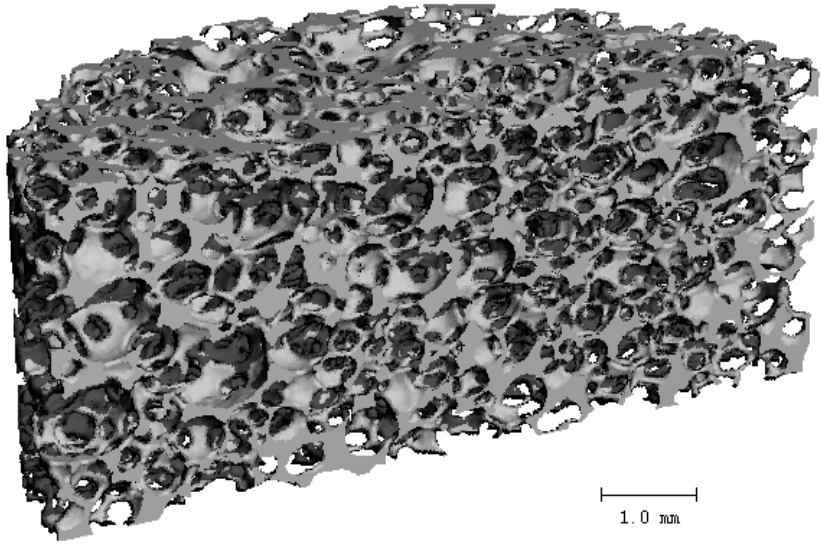

Figure D.6: 15% compressed TEMBO 3XE at 125°C

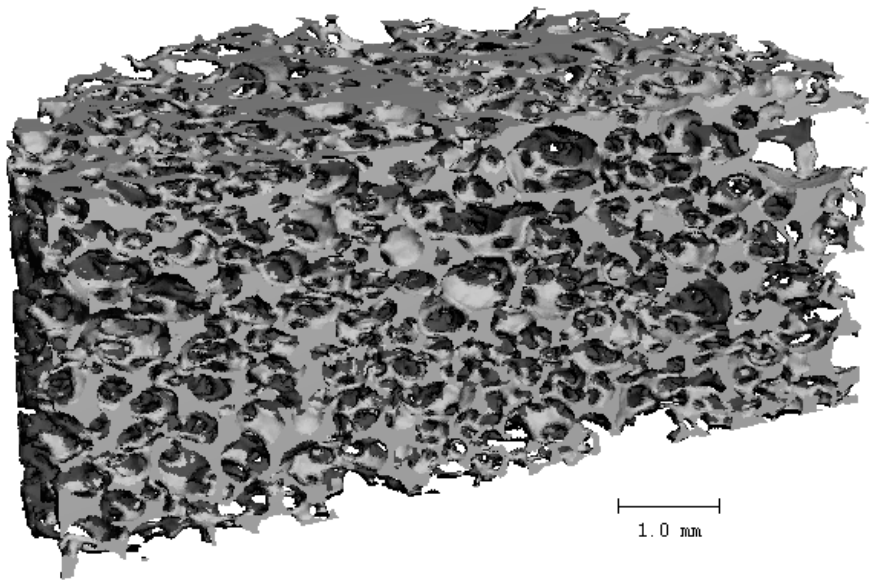

Figure D.7: 30% compressed TEMBO 3XE at 125°C

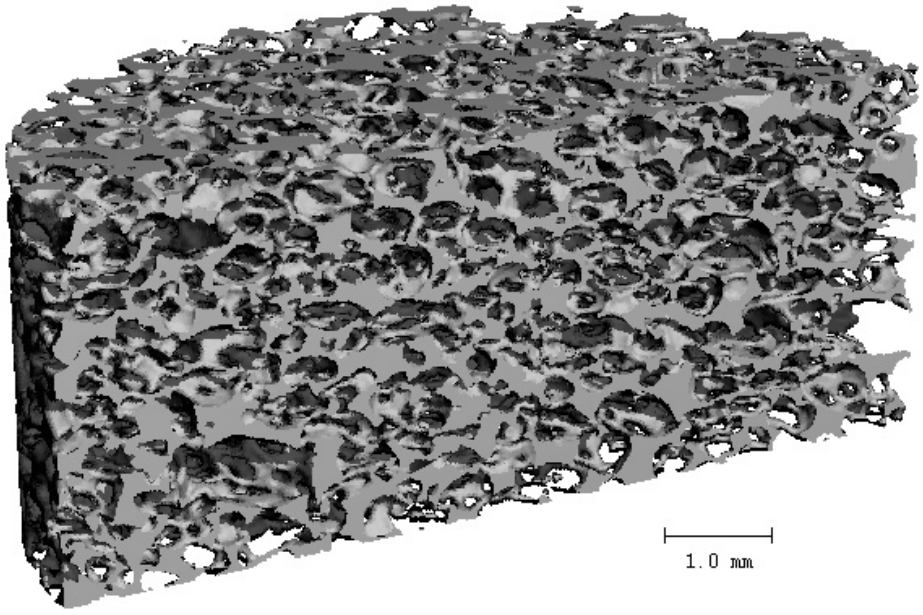

Figure D.8: 45% compressed TEMBO 3XE at 125°C

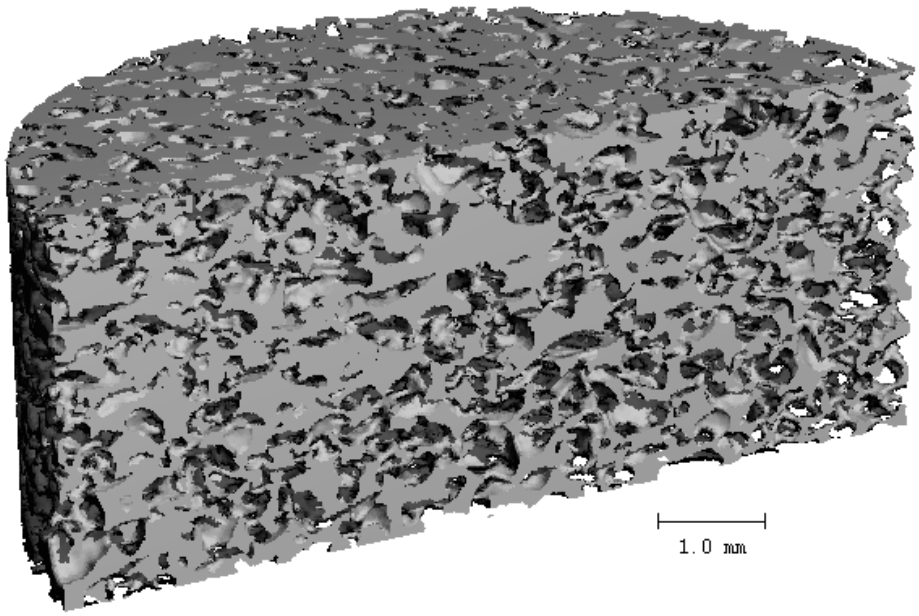

Figure D.9: 45% compressed TEMBO 3XE at 125°C

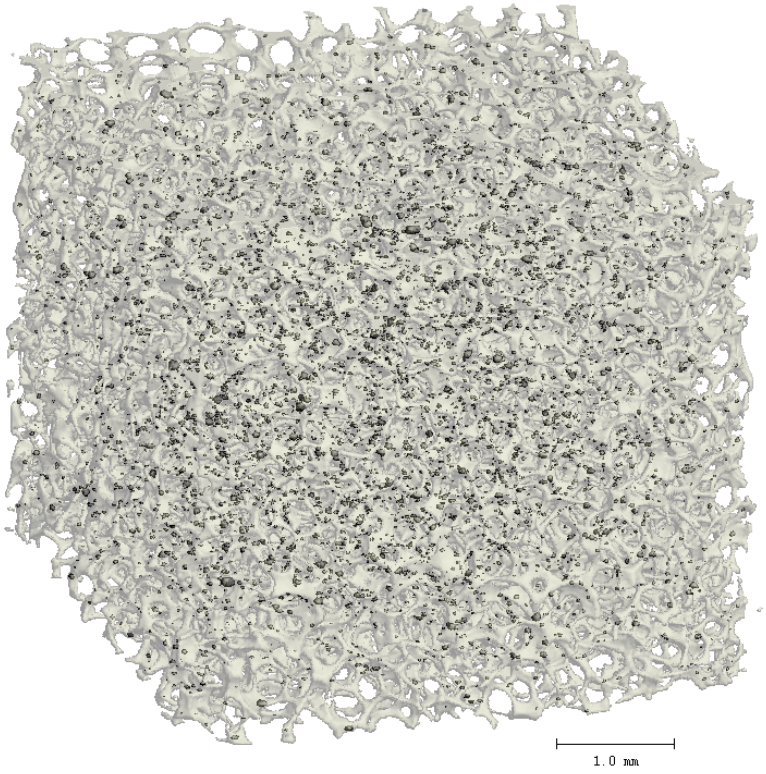

Figure D.10: DP5.1foam reinforced with 5wt% MagSilica

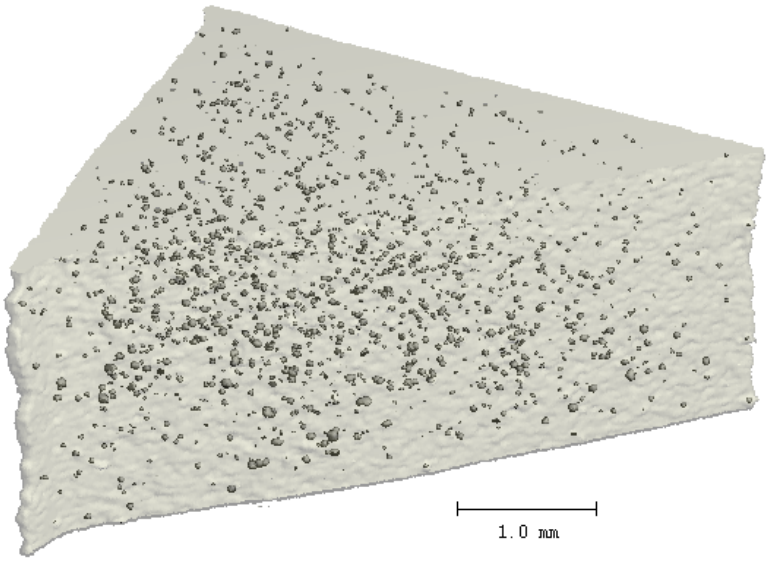

Figure D.11: DP5.1 reinforced with 1wt% nanomagnetite.

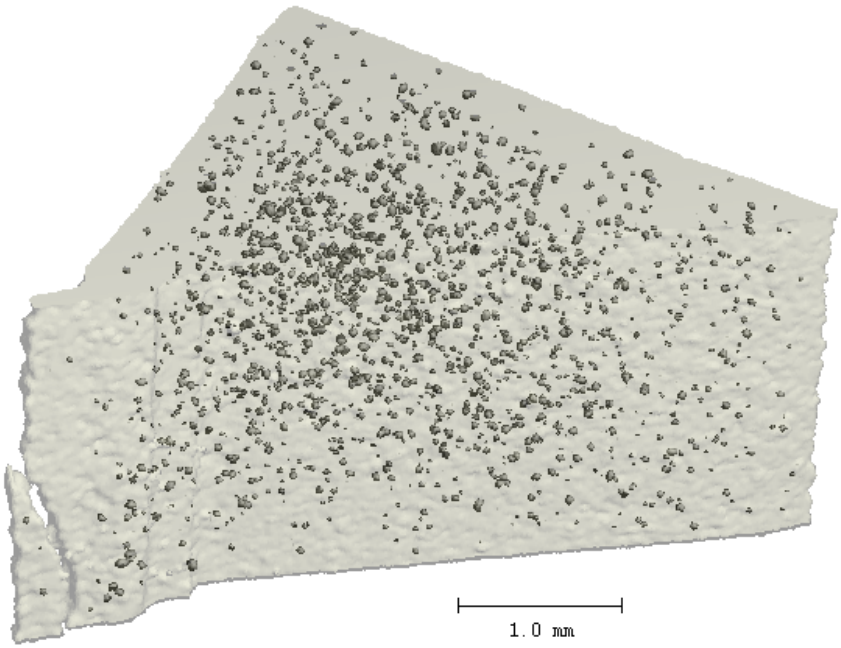

Figure D.12: DP5.1 reinforced with 2.5wt% nanomagnetite.

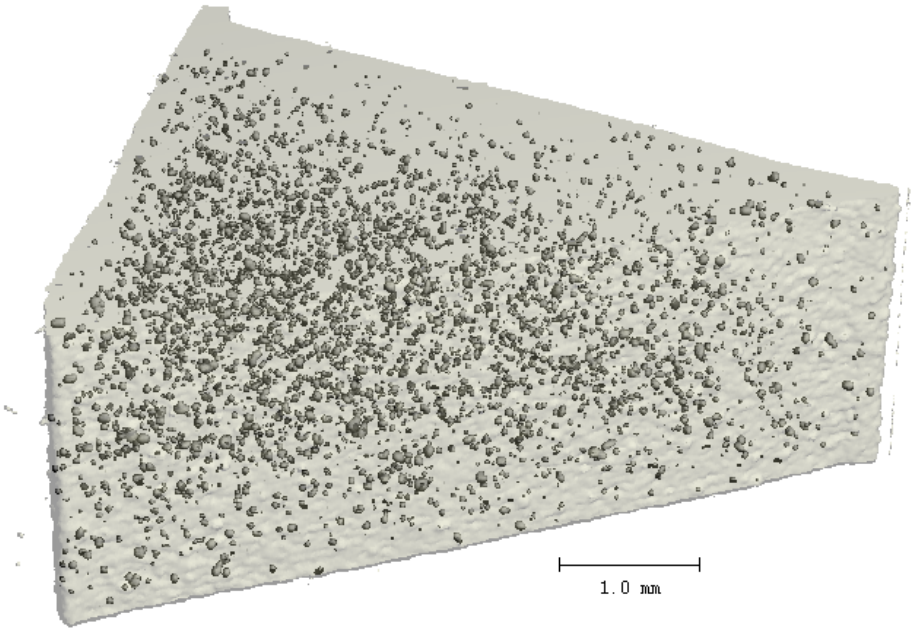

Figure D.13: DP5.1 reinforced with 5wt% nanomagnetite.

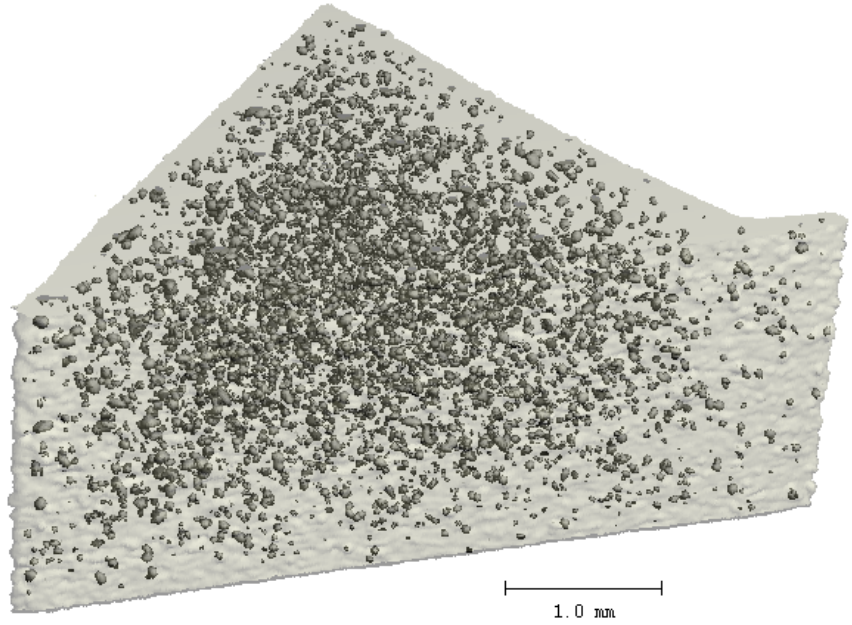

Figure D.14: DP5.1 reinforced with 10wt% nanomagnetite.

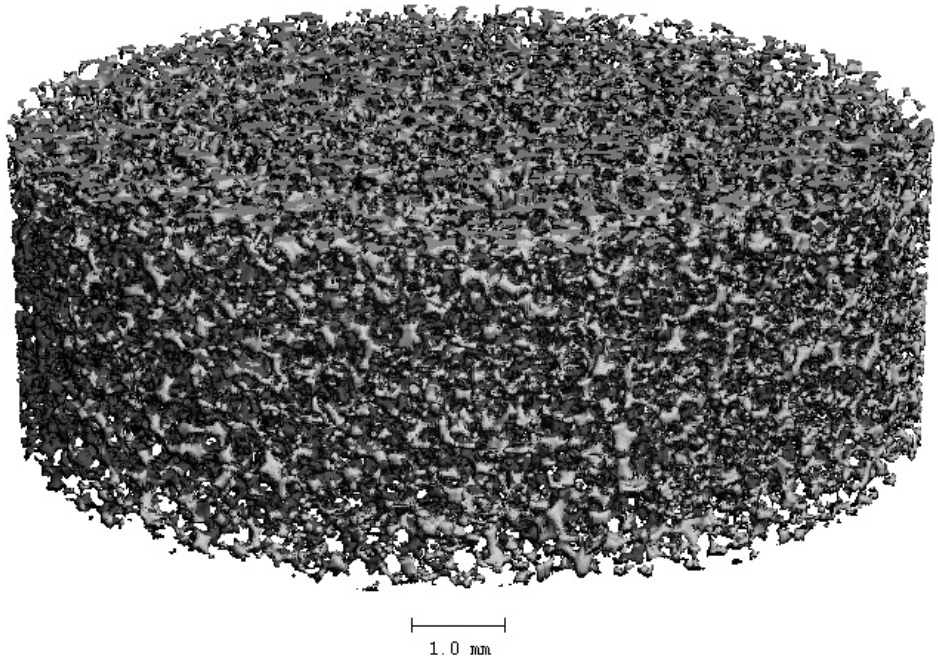

Figure D.15: DP5.1 foam, ~8% RD

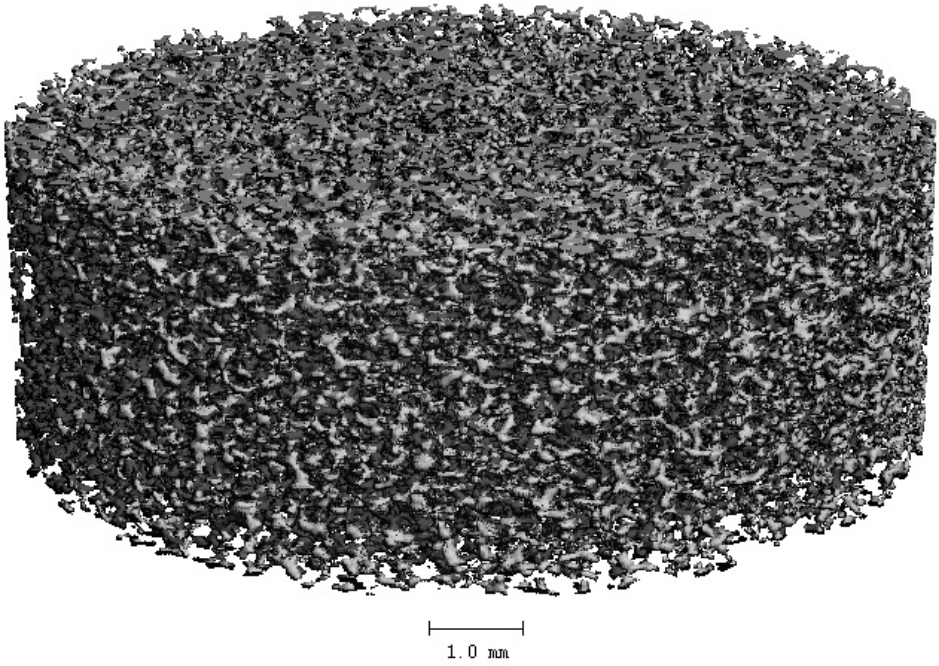

Figure D.16: DP5.1 foam reinforced 0.5wt% VGCF, ~9% RD

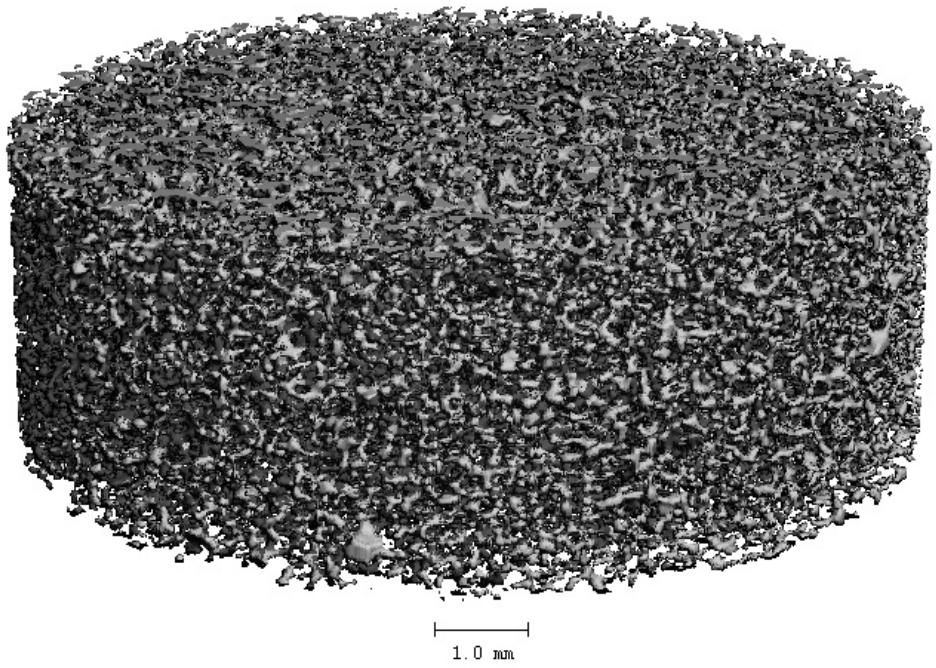

Figure D.17: DP5.1 foam reinforced 1w% VGCF, ~8% RD

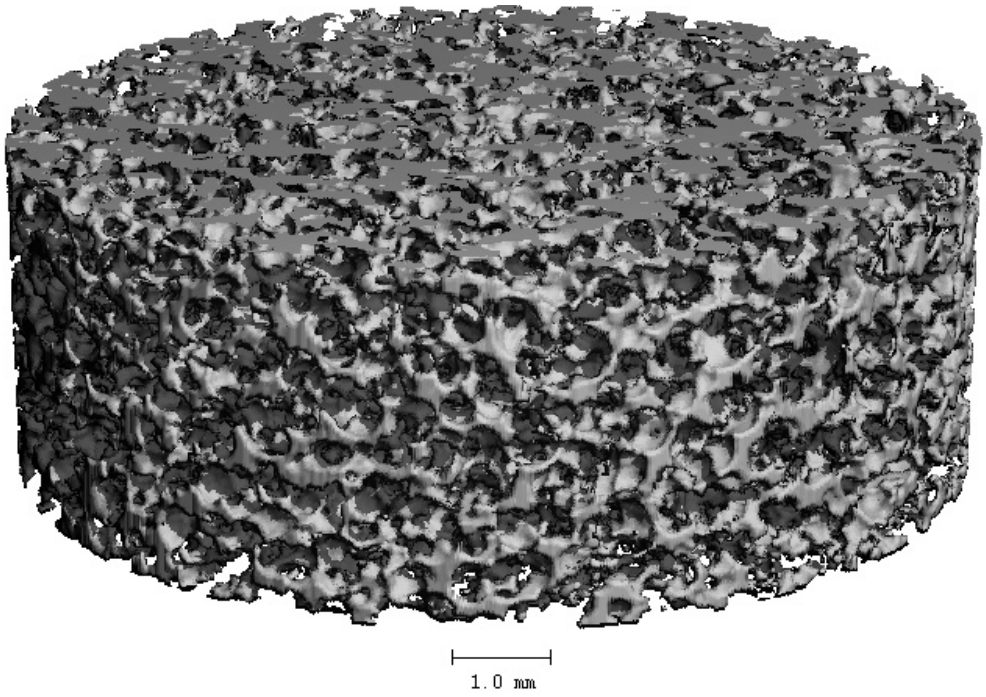

Figure D.18: DP5.1 foam reinforced 4w% VGCF, ~24% RD

REFERENCES

(1984-2009) MATLAB. The MathWorks, Inc.

(2005) ASTM D6226 "Standard Test Method for Open Cell Content of Rigid Cellular Plastics". ASTM International.

(2005) ASTM E1269 "Standard Test Method for Determining Specific Heat Capacity by Differential Scanning Calorimetery". ASTM International.

(2005) Igor Pro 5.04A. WaveMetrics, Lake Oswego, OR.

(2007) Hyperelastic behavior of rubberlike materials. In, *ABAQUS Analysis User's Manual*. Dassault Systems.

A. Brydon, S.B., E. Miller, G. Seidler (2005) Simulation of the densification of real open-celled foams microstructure, *Journal of the Mechanics and Physics of Solids*, **53**, 2638-2660.

Abrahamson, E.R., Lake, M.S., Munshi, N.A. and Gall, K. (2003) Shape memory mechanics of an elastic memory composite resin, *Journal of Intelligent Material Systems and Structures*, **14**, 623-632.

Adrien, J., Maire, E., Gimenez, N. and Sauvant-Moynot, V. (2007) Experimental study of the compression behaviour of syntactic foams by in situ X-ray tomography, *Acta Materialia*, **55**, 1667-1679.

Andrews, E.W., Gioux, G., Onck, P. and Gibson, L.J. (2001) Size effects in ductile cellular solids. Part II: experimental results, *International Journal of Mechanical Sciences*, **43**, 701-713.

Annette, M.S. (2006) Electromagnetic Activation of Shape Memory Polymer Networks Containing Magnetic Nanoparticles, *Macromolecular Rapid Communications*, **27**, 1168-1172.

Barot, G., Rao, I.J. and Rajagopal, K.R. (2008) A thermodynamic framework for the modeling of crystallizable shape memory polymers, *International Journal of Engineering Science*, **46**, 325-351.

Beyerlein, I.J. and Tomé, C.N. (2007) Modeling transients in the mechanical response of copper due to strain path changes, *International Journal of Plasticity*, **23**, 640-664.

Bezazi, A. and Scarpa, F. (2009) Tensile fatigue of conventional and negative Poisson's ratio open cell PU foams, *International Journal of Fatigue*, **31**, 488-494.

Boivin, M.-E.Y., Massieux, B., Breure, A.M., van den Ende, F.P., Greve, G.D., Rutgers, M. and Admiraal, W. (2005) Effects of copper and temperature on aquatic bacterial communities, *Aquatic Toxicology*, **71**, 345-356.

Buckley, P.R.M., G.H.; Wilson, T.S.; Small, W.; Benett, W.J.; Bearinger, J.P.; McElfresh, M.W.; Maitland, D.J. (2006) Inductively Heated Shape Memory Polymer for the Magnetic Actuation of Medical Devices, *Biomedical Engineering, IEEE Transactions on*, **53**, 2075 - 2083.

C. Jo, H.N. (2007) Constitutive modeling of HDPE polymer/clay nanocomposite foam, *Polymer*, **48**, 3349-3360.

C. M. Yakacki, S.W., C. Luders, K. Gall (2008) Deformation Limits in Shape-Memory Polymers, *Advanced Engineering Materials*, **10**, 112-119.

Chen, Y.-C. and Lagoudas, D.C. A constitutive theory for shape memory polymers. Part I: Large deformations, *Journal of the Mechanics and Physics of Solids*, **In Press, Corrected Proof**, 351.

Chen, Y.-C. and Lagoudas, D.C. A constitutive theory for shape memory polymers. Part II: A linearized model for small deformations, *Journal of the Mechanics and Physics of Solids*, **In Press, Corrected Proof**, 351.

Christopher M. Yakacki, R.S., David Safranski, Alicia M. Ortega, Katie Sassaman, Ken Gall (2008) Strong, Tailored, Biocompatible Shape-Memory Polymer Networks, *Advanced Functional Materials*, **18**, 2428-2435.

Chryssanthopoulos, M.K. and Righiniotis, T.D. (2006) Fatigue reliability of welded steel structures, *Journal of Constructional Steel Research*, **62**, 1199-1209.

Cooper, D.W. and Spielman, L.A. (1976) Data inversion using nonlinear programming with physical constraints: Aerosol size distribution measurement by impactors, *Atmospheric Environment (1967)*, **10**, 723-729.

Coorssen, J.R., Blank, P.S., Albertorio, F., Bezrukov, L., Kolosova, I., Chen, X., Backlund, P.S., Jr. and Zimmerberg, J. (2003) Regulated secretion: SNARE density, vesicle fusion and calcium dependence. 2087-2097.

Danielsson, M., Parks, D.M. and Boyce, M.C. (2004) Constitutive modeling of porous hyperelastic materials, *Mechanics of Materials*, **36**, 347-358.

Demiray, S., Becker, W. and Hohe, J. (2006) Analysis of two- and three-dimensional hyperelastic model foams under complex loading conditions, *Mechanics of Materials*, **38**, 985-1000.

Demiray, S., Becker, W. and Hohe, J. (2007) Numerical determination of initial and subsequent yield surfaces of open-celled model foams, *International Journal of Solids and Structures*, **44**, 2093-2108.

Du Bois, P.A., Kolling, S., Koesters, M. and Frank, T. (2006) Material behaviour of polymers under impact loading, *International Journal of Impact Engineering*, **32**, 725-740.

Ehlers, W. and Markert, B. (2003) A macroscopic finite strain model for cellular polymers, *International Journal of Plasticity*, **19**, 961-976.

G. Baer, T.S.W., D. L. Matthews, D. J. Maitland (2007) Shape-memory behavior of thermally stimulated polyurethane for medical applications, *Journal of Applied Polymer Science*, **103**, 3882-3892.

Gall, K., Dunn, M.L., Liu, Y.P., Finch, D., Lake, M. and Munshi, N.A. (2002) Shape memory polymer nanocomposites, *Acta Materialia*, **50**, 5115-5126.

Gall, K., Mikulas, M., Munshi, N.A., Beavers, F. and Tupper, M. (2000) Carbon fiber reinforced shape memory polymer composites, *Journal of Intelligent Material Systems and Structures*, **11**, 877-886.

Gall, K., Yakacki, C., Willis, S., Luders, C. and Tyber, J. (2007) Deformation limits in shape memory polymer foams, **In Review**.

Gibson, L.J. and Ashby, M.F. (1997) *Cellular solids: Structure and properties*. Cambridge University Press, Cambridge.

Gong, L. and Kyriakides, S. (2005) Compressive response of open cell foams - Part II: Initiation and evolution of crushing, *International Journal of Solids and Structures*, **42**, 1381-1399.

Gong, L., Kyriakides, S. and Jang, W.Y. (2005) Compressive response of open-cell foams. Part I: Morphology and elastic properties, *International Journal of Solids and Structures*, **42**, 1355-1379.

Guldberg, R.E., Hollister, S.J. and Charras, G.T. (1998) The Accuracy of Digital Image-Based Finite Element Models, *Journal of Biomechanicial Engineering*, **120**, 289-295.

Hayashi, S., Kondo, S., Kapadia, P. and Ushioda, E. (1995) Room-Temperature-Functional Shape-Memory Polymers, *Plastics Engineering*, **51**, 29-31.

Hayashi, S., Tasaka, Y., Hayashi, N. and Akita, Y. (2004) Development of Smart Polymer Materials and its Various Applications, *Mitsubishi Heavy Industries, Ltd. Technical Review*, **41**, 1-3.

Hildebrand, T., Laib, A., Muller, R., Dequeker, J. and Ruegsegger, P. (1999) Direct Three-Dimensional Morphometric Analysis of Human Cancellous Bone: Microstructural Data from Spine, Femur, Iliac Crest, and Calcaneus. 1167-1174.

Hohe, J. and Becker, W. (2003) Effective mechanical behavior of hyperelastic honeycombs and two-dimensional model foams at finite strain, *International Journal of Mechanical Sciences*, **45**, 891-913.

James Ren, X. and Silberschmidt, V.V. (2008) Numerical modelling of low-density cellular materials, *Computational Materials Science*, **43**, 65-74.

Jeong, H.M., Lee, S.Y. and Kim, B.K. (2000) Shape memory polyurethane containing amorphous reversible phase, *Journal of Materials Science*, **35**, 1579-1583.

Ken Gall, C.M.Y., Yiping Liu, Robin Shanda,s Nick Willett, Kristi S. Anseth (2005) Thermomechanics of the shape memory effect in polymers for biomedical applications, *Journal of Biomedical Materials Research A*, **73A**, 339-348.

Keyak, J.H. and Falkinstein, Y. (2003) Comparison of in situ and in vitro CT scan-based finite element model predictions of proximal femoral fracture load, *Medical Engineering & Physics*, **25**, 781-787.

Lendlein, A., Jiang, H., Junger, O. and Langer, R. (2005) Light-induced shape-memory polymers, *Nature*, **434**, 879-882.

Lendlein, A. and Kelch, S. (2002) Shape-Memory Polymers, *Angewandte Chemie International Edition*, **41**, 2034-2057.

Lim, T.J., Smith, B. and McDowell, D.L. (2002) Behavior of a random hollow sphere metal foam, *Acta Materialia*, **50**, 2867-2879.

Lin, A.S.P., Barrows, T.H., Cartmell, S.H. and Guldberg, R.E. (2003) Microarchitectural and mechanical characterization of oriented porous polymer scaffolds, *Biomaterials*, **24**, 481-489.

Liu, Y., Gall, K., Dunn, M.L. and McCluskey, P. (2004) Thermomechanics of shape memory polymer nanocomposites, *Mechanics of Materials*, **36**, 929-940.

Liu, Y.P., Gall, K., Dunn, M.L., Greenberg, A.R. and Diani, J. (2006) Thermomechanics of shape memory polymers: Uniaxial experiments and constitutive modeling, *International Journal of Plasticity*, **22**, 279-313.

Liu, Y.P., Gall, K., Dunn, M.L. and McCluskey, P. (2004) Thermomechanics of shape memory polymer nanocomposites, *Mechanics of Materials*, **36**, 929-940.

Lopatnikov, S.L., Gama, B.A. and Gillespie, J.W. (2007) Modeling the progressive collapse behavior of metal foams, *International Journal of Impact Engineering*, **34**, 587-595.

M. A. Di Prima, Lesniewski, M., Gall, K., McDowell, D.L., Sanderson, T. and Campbell, D. (2007) Thermo-mechanical behavior of epoxy shape memory polymer foams, *Smart Mater. Struct.*, 2330.

Maitland, D.J., Small, W., Iv, Ortega, J.M., Buckley, P.R., Rodriguez, J., Hartman, J. and Wilson, T.S. (2007) Prototype laser-activated shape memory polymer foam device for embolic treatment of aneurysms, *Journal of Biomedical Optics*, **12**, 030504-030503.

Metcalfe, A., Desfaits, A.-C., Salazkin, I., Yahia, L.H., Sokolowski, W.M. and Raymond, J. (2003) Cold hibernated elastic memory foams for endovascular interventions, *Biomaterials*, **24**, 491-497.

Montminy, M.D., Tannenbaum, A.R. and Macosko, C.W. (2004) The 3D structure of real polymer foams, *Journal of Colloid and Interface Science*, **280**, 202-211.

Nagaraja, S., Couse, T.L. and Guldberg, R.E. (2005) Trabecular bone microdamage and microstructural stresses under uniaxial compression, *Journal of Biomechanics*, **38**, 707-716.

Odgaard, A. and Gundersen, H.J.G. (1993) Quantification of connectivity in cancellous bone, with special emphasis on 3-D reconstructions, *Bone*, **14**, 173-182.

Ohki, T., Ni, Q.Q., Ohsako, N. and Iwamoto, M. (2004) Mechanical and shape memory behavior of composites with shape memory polymer, *Composites Part a-Applied Science and Manufacturing*, **35**, 1065-1073.

Onck, P.R. (2001) Application of a continuum constitutive model to metallic foam DEN-specimens in compression, *International Journal of Mechanical Sciences*, **43**, 2947-2959.

Onck, P.R., Andrews, E.W. and Gibson, L.J. (2001) Size effects in ductile cellular solids. Part I: modeling, *International Journal of Mechanical Sciences*, **43**, 681-699.

P. Hard af Segerstad, R.L., S. Toll (2007) A constitutive equation for open-cell cellular solids, including viscoplastic, damage and deformation induced anisotropy, *International Journal of Plasticity*, **In Press**.

Qi, H.J., Nguyen, T.D., Castro, F., Yakacki, C.M. and Shandas, R. (2008) Finite deformation thermo-mechanical behavior of thermally induced shape memory polymers, *Journal of the Mechanics and Physics of Solids*, **56**, 1730-1751.

Quispe, A., Medina, S.F., Gómez, M. and Chaves, J.I. (2007) Influence of austenite grain size on recrystallisation-precipitation interaction in a V-microalloyed steel, *Materials Science and Engineering: A*, **447**, 11-18.

Rasband, W.S. (1997-2008) ImageJ. U.S. National Institute of Health, Bethesda, Maryland.

Roberts, A.P. and Garboczi, E.J. (2001) Elastic moduli of model random three-dimensional closed-cell cellular solids, *Acta Materialia*, **49**, 189-197.

Roberts, A.P. and Garboczi, E.J. (2002) Elastic properties of model random three-dimensional open-cell solids, *Journal of the Mechanics and Physics of Solids*, **50**, 33-55.

Rorden, C. (1999-2005) MRIcro.

Rubinstein, M. and Colby, R. (2003) *Polymer Physics*. Oxford University Press, Oxford.

Ryan, T.M. and Milner, G.R. (2006) Osteological applications of high-resolution computed tomography: a prehistoric arrow injury, *Journal of Archaeological Science*, **33**, 871-879.

Safranski, D.L. and Gall, K. Effect of Chemical Structure and Crosslinking Density on the Thermo-Mechanical Properties and Toughness of (Meth)acrylate Shape-Memory Polymer Networks, *Polymer*, **In Press, Accepted Manuscript**.

Sanderson, T. and Gall, K. (2007) Shape Memory Polymer Characterization for Advanced Air Vehicle Technologies, *Raytheon Technology Today*, 10.

Scarpa, F., Ciffo, L.G. and Yates, J.R. (2004) Dynamic properties of high structural integrity auxetic open cell foam, *Smart Materials & Structures*, **13**, 49-56.

Schraad, M.W. (2007) The influence of dispersity in geometric structure on the stability of cellular solids, *Mechanics of Materials*, **39**, 183-198.

Schraad, M.W. and Harlow, F.H. (2006) A stochastic constitutive model for disordered cellular materials: Finite-strain uni-axial compression, *International Journal of Solids and Structures*, **43**, 3542-3568.

Silva, M.J. and Gibson, L.J. (1997) The effects of non-periodic microstructure and defects on the compressive strength of two-dimensional cellular solids, *International Journal of Mechanical Sciences*, **39**, 549-563.

Simulia (2007) ABAQUS/Standard 6.7-1. Warwick, Rhode Island.

Sivakumar, S., Subbanna, M., Sahay, S.S., Ramakrishnan, V., Kapur, P.C., Pradip and Malghan, S.G. (2001) Population balance model for solid state sintering II. Grain growth, *Ceramics International*, **27**, 63-71.

Small, W., Buckley, P.R., Wilson, T.S., Benett, W.J., Hartman, J., Saloner, D. and Maitland, D.J. (2007) Shape Memory Polymer Stent With Expandable Foam: A New Concept for Endovascular Embolization of Fusiform Aneurysms, *Biomedical Engineering, IEEE Transactions on*, **54**, 1157-1160.

Smith, T. (1963) Ultimate tensile properties of elastomers. I. Characterization by a time and temperature independent failure envelope, *Journal of Polymer Science Part A*, **1**, 3597-3536.

Sokolowski W M, C.A., Hayashi S, Yamada T (1999) Cold hibernated elastic memory (CHEM) self-deployable structures. *Smart Structures and Materials 1999: Electroactive Polymer Actuators and Devices*. SPIE.

Tey, S.J., Huang, W.M. and Sokolowski, W.M. (2001) Influence of long-term storage in cold hibernation on strain recovery and recovery stress of polyurethane shape memory polymer foam, *Smart Materials & Structures*, **10**, 321-325.

Tobushi, H., Hara, H., Yamada, E. and Hayashi, S. (1996) Thermomechanical properties in a thin film of shape memory polymer of polyurethane series, *Smart Materials & Structures*, **5**, 483-491.

Tobushi, H., Matsui, R., Hayashi, S. and Shimada, D. (2004) The influence of shape-holding conditions on shape recovery of polyurethane-shape memory polymer foams, *Smart Materials & Structures*, **13**, 881-887.

Tobushi, H., Okumura, K., Endo, M. and Hayashi, S. (2001) Thermomechanical properties of polyurethane shape-memory polymer foam. In, *Shape Memory Materials and Its Applications*. 577-580.

Tobushi, H., Okumura, K., Hayashi, S. and Ito, N. (2001) Thermomechanical constitutive model of shape memory polymer, *Mechanics of Materials*, **33**, 545-554.

Tuan, H.S. and Hutmacher, D.W. (2005) Application of micro CT and computation modeling in bone tissue engineering, *Computer-Aided Design*, **37**, 1151-1161.

Vialle, G., Prima, M.A.D., Hocking, E., Gall, K., Garmestani, H., Sanderson, T., Arzberger, S. and Campbell, D. (Submitted) Remote Activation of Nanomagnetite Reinforced Shape Memory Polymer Foam, *Advanced Functional Materials*.

Wang, Y., Gioia, G. and Cuitino, A.M. (2000) The deformation habits of compressed open-cell solid foams, *Journal of Engineering Materials and Technology-Transactions of the Asme*, **122**, 376-378.

Woods, R.P. (2002) AIR 5.0.

Y. Liu, K.G., M. Dunn, A. Greenberg, J. Diani (2006) Thermomechanics of shape memory polymers: Uniaxial experiments and constitutive modeling, *International Journal of Plasticity*, **22**, 279-313.

Yakacki, C.M., Shandas, R., Lanning, C., Rech, B., Eckstein, A. and Gall, K. (2007) Unconstrained recovery characterization of shape-memory polymer networks for cardiovascular applications, *Biomaterials*, **28**, 2255-2263.

Yang, B., Huang, W.M., Li, C., Li, L. and Chor, J.H. (2005) Qualitative separation of the effects of carbon nano-powder and moisture on the glass transition temperature of polyurethane shape memory polymer, *Scripta Materialia*, **53**, 105-107.

Youssef, S., Maire, E. and Gaertner, R. (2005) Finite element modelling of the actual structure of cellular materials determined by X-ray tomography, *Acta Materialia*, **53**, 719-730.

Zenkert, D. and Burman, M. (2008) Tension, compression and shear fatigue of a closed cell polymer foam, *Composites Science and Technology*, **In Press, Corrected Proof**.

Zhou, J. and Soboyejo, W.O. (2005) Mechanics modeling of the compressive stiffness and strength of open-celled aluminum foams (vol 19, pg 863, 2004), *Materials and Manufacturing Processes*, **20**, 129-129.